UNIVERSITY OF CALIFORNIA

Los Angeles

Empirical Modeling of 3D Plasma Pressure and Magnetic Field Structures in the Earth's Plasma Sheet

A dissertation submitted in partial satisfaction of

the requirements for the degree Doctor of Philosophy

in Atmospheric and Oceanic Sciences

by

Chao Yue

2015

ABSTRACT OF THE DISSERTATION

Empirical modeling of 3D plasma pressure and magnetic field structures in the Earth's plasma sheet

by

Chao Yue

Doctor of Philosophy in Atmospheric and Oceanic Sciences

University of California, Los Angeles, 2015

Professor Lawrence R. Lyons, Chair

Ions and electrons in the nightside magnetosphere, driven by the dawn-to-dusk convection electric field, flow earthward and are energized. As a result, plasma pressure is enhanced and magnetic field configuration becomes more stretched, forming the necessary conditions for the development of substorms. Determining the physical processes leading to the changes of the plasma and magnetic field configurations, as well as the processes resulting from the configuration variations, is thus crucial to understanding substorms. Accurate evaluation of these processes, including formation of field-aligned currents (FACs), isotropization by current sheet scattering, and some localized instabilities that may responsible for substorm onset, relies on knowing the realistic 3 dimensional (3D) magnetic field configurations, which cannot be provided by current available empirical models with sufficient accuracy or as a function of growth phase development. Therefore, we have developed a 3D force-balanced empirical substorm growth phase magnetic field model, which allows us to investigate the evolution of these configurations during the substorm growth phase and evaluate the physical processes

governing the configuration changes. Here, we first statistically analyzed the growth phase pressures using Geotail and THEMIS data, and identified three primary factors causing the growth phase pressure change: solar wind dynamic pressure (P_{SW}), energy loading, and sunspot number. We then constructed a 2D equatorial empirical pressure model and an error model in the near Earth plasma sheet ($r \leq 20$ R_E) using the Support Vector Regression Machine (SVRM) with the three factors as input. The model predicts the plasma sheet pressure accurately with median errors of 5%, and the predicted pressure gradients agree reasonably well with observed gradients obtained from two-probe measurements. The model shows that pressure increases linearly as P_{SW} increases, while the pressure responses to energy loading and sunspot number are nonlinear. From these model pressure distributions, we were able to establish a realistic 3D growth phase magnetic field configurations that satisfy the physical constraint of force balance with the plasma pressures using a 3D magnetic field model [*Zaharia*, 2008]. The force-balanced magnetic field configuration shows that Bz decreases in the near Earth region and increases in the tail due to an increasing perpendicular current peaking at the earthward edge of the plasma sheet. The current peak moves towards the Earth as energy loading increases, indicating earthward penetrating of the plasma sheet. Meanwhile, positive dBz/dz is found to develop late in the growth phase, but a Bz minimum at the equator does not form, unlike the prediction by *Saito et al.* [2010]. The perpendicular current peaks off the equator plane and its peak moves towards the equatorial plane as the growth phase evolves, indicating the thinning of current sheet. In addition, there are typical Region-1 FACs around 12 to 20 R_E at the beginning of substorm growth phase and they gradually evolve to Region-2 FACs in the late growth phase with their earthward boundary moving to smaller r. The model magnetic fields agree quantitatively well with observed fields. The magnetic field is substantially more stretched under higher P_{SW} while the dependence on sunspot number is non-linear and less substantial. The excellent agreements between the model results and observations give us confidence that the realistic model can be used at the first time to understand the pressure and magnetic field changes observed during a substorm event by providing accurate evaluations of the effects of energy loading and P_{SW}, as well as the temporal and spatial effects along a spacecraft trajectory. By applying our modeling to a substorm event, we found that the equatorward moving of proton aurora during the growth phase is mainly due to continuous stretching of magnetic field lines, and the ballooning instability is more favorable at late growth phase around midnight tail where there is a localized plasma beta peak. Furthermore, the equatorial mapping of the breakup auroral arc is X ~ –14 R_E near midnight, coinciding with the location of the maximum growth rate for ballooning instability.

The dissertation of Chao Yue is approved.

Vassilis Angelopoulos

Richard M. Thorne

Chih-Ping Wang

Lawrence R. Lyons, Committee Chair

University of California, Los Angeles

2015

Dedicated to my parents and great family for their love and support

Table of Contents

Acknowledgements

I would like to express my deepest gratitude to my thesis advisor, Prof. Larry Lyons and my research supervisor, Dr. Chih-Ping Wang, for their guidance and inspiration on my research works. I have benefited a lot from their profound knowledge.

I want to also thank my coauthors, collaborators who contribute a lot for my Ph.D. research: Prof. Vassilis Angelopoulos and Dr. Toshi Nishimura at UCLA; Prof. Eric Donovan and Dr. Jun Liang at University of Calgary, Canada; Dr. Mike Henderson at Los Alamos National Lab; Dr. Tony Lui at Johns Hopkins University Applied Physics Laboratory; Dr. Kyle Murphy at NASA Goddard Space Flight Center and Dr. Yongli Wang at University of Maryland. Especially, I'd like to thank Dr. Sorin Zaharia at University of California, Berkeley, who generate my Ph.D. research project at the first place. Without him, I won't be able to conduct this fantastic research project.

In addition, I want to thank Prof. Richard Thorne who taught me a lot about space physics and for his support as my Ph.D. committee member and my postdoctoral advisor.

Meanwhile, I'm also grateful for the excellent atmosphere provided by my colleagues at UCLA. They made my life easier and happier everyday.

I would also like to thank my parents, my elder sister, and elder brother. They were always supporting me and encouraging me with their best wishes.

Finally, I would like to thank my husband, Dr. Jianzhu Ma. He was always there cheering me up and stood by me through the good times and bad.

Chao Yue

Los Angeles, California

June 25, 2015

Chapter 2 is a combined version of "Wang, C.-P., **C. Yue**, S. Zaharia, X. Xing, L. Lyons, V. Angelopoulos, T. Nagai, and T. Lui (2013), Empirical modeling of plasma sheet pressure and three-dimensional force-balanced magnetospheric magnetic field structure: 1. Observation, *J. Geophys. Res. Space Physics*, 118, doi:10.1002/jgra.50585." and "**Yue, C.,** C.-P. Wang, L. Lyons, Y. Wang, T. Hsu, V. Angelopoulos, M. Henderson, A.T.Y. Lui, Tsugunobu Nagai, A 2D empirical plasma sheet pressure model for substorm growth phase using the Support Vector Regression Machine, *J. Geophys. Res. Space Physics, 120, doi:10.1002/2014JA020787.* " as well as part of "**Yue, C.,** C.-P. Wang, S. G. Zaharia, X. Xing, and L. Lyons (2013), Empirical modeling of plasma sheet pressure and three-dimensional force-balanced magnetospheric magnetic field structure: 2. Modeling, *J. Geophys. Res. Space Physics*, 118, doi:10.1002/2013JA018943."

Chapter 3 is a part version of "**Yue, C.,** C.-P. Wang, S. G. Zaharia, X. Xing, and L. Lyons (2013), Empirical modeling of plasma sheet pressure and three-dimensional force-balanced magnetospheric magnetic field structure: 2. Modeling, *J. Geophys. Res. Space Physics*, 118, doi:10.1002/2013JA018943."

Chapter 4 is a version of "**Yue, C.,** C.-P. Wang, L. Lyons, J. Liang, E. F. Donovan, S. G. Zaharia, and M. Henderson (2014), Current sheet scattering and ion isotropic boundary under 3-D empirical force-balanced magnetic field, *J. Geophys. Res. Space Physics*, 119, doi:10.1002/2014JA020172."

Chapter 5 is a version of "**Yue, C.,** C.-P. Wang, Y. Nishimura, K. R. Murphy, X. Xing, L. Lyons, M. Henderson, V. Angelopoulos, A. T. Y. Lui, and T. Nagai (2015), Empirical modeling of 3D Force-balanced Plasma and Magnetic Field Structures during Substorm Growth Phase, J. Geophys. Res. Space Physics, 120, doi:10.1002/2015JA021226."

This research was funded by NASA Grant NNX11AJ12G, and NNX08A135G, NSF Grant ATM-1003595, and IGPPS Program at Los Alamos National Laboratory. All THEMIS data are from THEMIS official website (http://themis.ssl.berkeley.edu/data_files.shtml). All Geotail data are from the Institute of Space and Astronautical Science/Japan Aerospace Exploration Agency (ISAS/JAXA) through the Data Archives and Transmission System (DARTS) of ISAS (http://www.darts.isas.jaxa.jp/).

Vita

June, 2008	Bachelor of Engineering, School of Electronic Information Wuhan University, Hubei, China **Best Undergraduate Thesis Award of Hubei province**
June, 2011	M.S., Space Sciences Institute of Space Physics and Applied Technology Peking University, Beijing, China
June, 2013	M. S., Space Sciences Department of Atmospheric and Oceanic Sciences University of California, Los Angeles, USA
2011	**UCLA Chancellor's Prize**
2013	**NSF-GEM Best Student Poster Award**
2014	**AGU Outstanding Student Paper Award**
2015	**UCLA Dissertation Year Fellowship**
2015	Teaching Assistant Department of Atmospheric and Oceanic Sciences University of California, Los Angeles, USA.
2012-2015	Graduate Student Research Assistant Department of Atmospheric and Oceanic Sciences University of California, Los Angeles, USA

PUBLICATIONS

1. **Yue, C.,** C.-P. Wang, Y. Nishimura, K. R. Murphy, X. Xing, L. Lyons, M. Henderson, V. Angelopoulos, A. T. Y. Lui, and T. Nagai (2015), Empirical modeling of 3D Force-balanced Plasma and Magnetic Field Structures during Substorm Growth Phase, *J. Geophys. Res. Space Physics*, 120, doi:10.1002/2015JA021226.

2. **Yue, C.,** C.-P. Wang, L. Lyons, Y. Wang, T. Hsu, V. Angelopoulos, M. Henderson, A.T.Y. Lui, Tsugunobu Nagai, A 2D empirical plasma sheet pressure model for substorm growth phase using the Support Vector Regression Machine, *J. Geophys. Res. Space*

Physics, 120, doi:10.1002/2014JA020787.

3. **Yue, C.,** C.-P. Wang, L. Lyons, J. Liang, E. F. Donovan, S. G. Zaharia, and M. Henderson (2014), Current sheet scattering and ion isotropic boundary under 3-D empirical force-balanced magnetic field, *J. Geophys. Res. Space Physics*, 119, doi:10.1002/2014JA020172.

4. **Yue, C.,** C.-P. Wang, S. G. Zaharia, X. Xing, and L. Lyons (2013), Empirical modeling of plasma sheet pressure and three-dimensional force-balanced magnetospheric magnetic field structure: 2. Modeling, *J. Geophys. Res. Space Physics*, 118, doi:10.1002/2013JA018943.

5. **Yue C.,** Y. Nishimura, L. R. Lyons, V. Angelopoulos, E. F. Donovan, Q. Shi, Z. Yao, and J. W. Bonnell (2013), Coordinated THEMIS spacecraft and all-sky imager observations of interplanetary shock effects on plasma sheet flow bursts, poleward boundary intensifications, and streamers, *J. Geophys. Res. Space Physics*, 118, doi:10.1002/jgra.50372.

6. **Yue C.,** and Q. Zong (2011), Solar wind parameters and geomagnetic indices for four different interplanetary shock/ICME structures, *J. Geophys. Res. Space Physics*, 116, A12201, doi:10.1029/2011JA017013.

7. **Yue C.,** Q. Zong, Y. Wang, I. I. Vogiatzis, Z. Pu, S. Fu, and Q. Shi (2011), Inner magnetosphere plasma characteristics in response to interplanetary shock impacts, *J. Geophys. Res. Space Physics*, 116, A11206, doi:10.1029/2011JA016736.

8. **Yue C.,** Q.-G. Zong, H. Zhang, Y. F.Wang, C. J. Yuan, Z. Y. Pu, S. Y. Fu, A. T. Y. Lui, B. Yang and C.R.Wang (2010), Geomagnetic activities triggered by interplanetary shocks *J. Geophys. Res. Space Physics,* 115, A00I05, doi:10.1029/2010JA015356.

CHAPTER 1 | Introduction

To help readers who are not familiar with magnetospheric physics, I present in section 1.1 a short introduction of magnetospheric configuration and dynamics. Readers who are familiar with these issues could go directly to section 1.2, in which my motivation of establishing the plasma sheet pressure distributions and the Earth's magnetic field configurations is given along with my research goals. In section 1.3, substorm related phenomena are described. In section 1.4, a brief description of major global Earth's magnetic field modeling is presented. In section 1.5, I present the objective of this thesis and the thesis organization.

1.1 General introduction

1.1.1 Structure of the Earth's magnetosphere

The Earth's magnetosphere as shown in Figure 1.1 is contained inside a surface boundary called the magnetopause with a bow shock forming in front of it due to the supersonic nature of the solar wind. The region between the bow shock and the magnetopause is called the magnetosheath, where flow is subsonic but plasma is hotter and more turbulent than in the solar wind. The Earth's magnetosphere includes the inner magnetosphere, plasma sheet and tail lobes according to their plasma and magnetic field characteristics.

(1) Inner magnetosphere: The inner magnetosphere is the closed field-line region that extends from the dayside magnetopause to about geosynchronous orbit on the nightside. This is a region populated by the inner and the outer radiation belts. A typical density of energetic ions is 1 cm^{-3}, and ion energy in the radiation belt is on the order of 100 keV. The particles lost from the inner magnetosphere (through magnetopause shadowing or collisions with neutral gas or by scattering and precipitation to the atmosphere) are compensated by injection of fresh plasma from plasma sheet during magnetic storms and substorms.

(2) Plasma sheet: The plasma sheet is a layer of hot plasma within the closed field-line region of the nightside magnetosphere, extending in the equatorial plane from ~6 R_E (Earth radii, 1 R_E = 6380 km) to about 50 R_E downtail from the Earth with a typical thickness of 6 R_E and width in the east-west direction of 40 R_E [*Borovsky et al.,* 1998]. The plasma sheet is a region of high plasma beta (β, the ratio between the plasma pressure (P_P = nkT) and magnetic pressure ($P_B = B^2/2\mu_o$), $\beta = P_P/P_B > 10$), with plasma density of 0.1-1 cm^{-3} and typical ion energy of a few keV. Unlike the inner magnetosphere, this region is rather dynamic, with its parameters (pressure, P, density, n, temperature, T) varying substantially in time.

(3) Tail lobes: The tail lobes are two regions of tenuous plasma and relatively strong magnetic field lying north and south of the plasma sheet. Field lines of the lobes are open and maintain roughly the same direction pointing towards Earth north of the equator and away from Earth south of it. Plasma density is typically 0.01 cm^{-3}, and the strong magnetic field leads to very low plasma β.

1.1.2 Magnetospheric dynamics

The magnetosphere generally changes all the time. Sometimes the change is slow and gradual, while other times it can be very explosive. Since the solar wind is the main energy and particle sources for the magnetosphere, magnetospheric activity is closely connected to the solar wind conditions.

(1) Magnetospheric convection: Magnetospheric convection is a process that can replenish magnetospheric plasma from the slowly precipitation loss into the atmosphere, through the partially "open" Earth's magnetic field lines when reconnection happens as sketched in Figure 1.2. When the interplanetary magentic field (IMF) has a southward component which is opposite to the Earth's magentic field on the dayside, reconnection between the IMF and Earth's field happens. The reconnected "open" magnetospheric field lines are then swept away over the polar caps with the solar wind. When they arrive in the magnetotail, the magnetic field lines from the opposite hemispheres again reconnect and become closed, providing magnetic flux that then returns back to the dayside. Under southward IMF, the electric field in the solar wind, $\mathbf{E}_{SW} = -\mathbf{V}_{SW} \times \mathbf{B}_{SW}$, thus, creates an electric potential difference across the whole magnetosphere and it results in dawn to dusk electric field in the magentotail, which generates the plasma earthward flow due to the $\mathbf{E} \times \mathbf{B}$ drift.

(2) Geomagnetic Storms: A geomagnetic storm occurs under a long period (several hours) of intense southward IMF driven by a solar coronal mass ejection (CME) or a high speed stream (co-rotating interaction region or CIR). A geomagnetic storm consists of a sudden commencement, the main phase, and recovery phase. During the main phase, the intensified westward ring current causes a decrease in the horizontal magnetic field at the Earth's surface. The frequency of geomagnetic storms increases and decreases with the solar cycle. CME driven storms are more common during the solar maximum and CIR driven storms are more common during the declining phase of the solar cycle.

(3) Substorms: Magnetospheric substorm is one of the most interesting and complex phenomena in space physics. It is a process of storage and sudden release of energy in the Earth's magnetosphere. Its development has generally been categorized into three phases: the growth, expansion, and recovery phases. The growth phase [*McPherron,* 1970] is a period, lasting from 20 minutes to 1 hour, that starts with the southward turning of IMF and ends at the onset of the expansion phase. Throughout the growth phase, solar wind energy is accumulating in the Earth's magnetotail; in the magnetosphere, observations of high-energy particle fluxes at geostationary orbit during the growth phase [e.g., *Baker and McPherron,* 1990] indicate strong field line stretching and the formation of a thin current sheet in the near-Earth tail [e.g., *Sergeev et al.,* 1990, 2011*; Sanny et al.,* 1994].

1.1.3 Magnetosphere-ionosphere coupling (M-I coupling)

The ionosphere and magnetosphere form a closely coupled and interacting system. The coupling of the terrestrial magnetosphere and ionosphere is fundamental to understanding the behavior of each region. Strong coupling is often associated with the closure of intense electrical currents flowing along magnetic fields lines, called field-aligned currents, which produce optical aurora emission when magnetospheric electrons are precipitated into ionosphere. There is also ion precipitation caused by pitch angle scattering, leading to proton aurora, which is generally much weaker than electron auroral but also quite interesting.

(1) Auroral dynamics: Aurora Borealis occur in the Earth's ionosphere, and result from collisions between energetic electrons (sometimes also protons, and even heavier charged particles) and atoms and molecules in the upper atmosphere (~100 km or above). The ultimate origin of the energy which powers the aurora borealis is the Sun – via the solar wind and its coupling to the Earth's magnetic field. Interactions between the solar wind (which carries its own tangled magnetic fields) and the Earth's magnetic field may cause electrons (and other particles) to be trapped and accelerated; those particles which aren't trapped in the Earth's magnetosphere could be dumped to the ionosphere due to pitch angle scattering leading to aurora.

(2) Field-aligned currents (FACs): A very important topic with regard to ionospheric particle precipitation and aurora is the field-aligned currents (FACs), which are seen flowing along the magnetic field lines. They connect to the horizontal currents in the ionosphere, forming a closed electrical circuit. Study of the FACs is extremely important to ionospheric phenomena. FACs result from the diversion of the transverse magnetospheric currents, so they are crucial to the M-I coupling. Typical FACs consist of Region-1 (R1) FACs which flow from/into ionosphere on dusk/dawn side at higher latitudes and Region-2 (R2) with the opposite directions at lower latitudes as shown in Figure 1.3.

1.2 Plasma pressure distributions and magnetic field configurations

Plasma pressure is several tenths of nPa in the plasma sheet [e.g., *Huang and Frank*, 1986; 1994] and increases to several nPa in the inner magnetosphere [e.g., *Lui and Hamilton*, 1992; *De Michelis et al.*, 1999; *Kirpichev and Antonova*; 2011]. The pressure varies significantly during geomagnetic disturbances [e.g., *Baumjohann et al*., 1991; *Kistler et al*., 1992]. Highly isotropic pressure is commonly observed in the tail plasma sheet [e.g., *Kauffmann et al*., 2002; *Wang et al*., 2011] but pressure becomes anisotropic in the inner magnetosphere with larger pressure in the perpendicular direction [e.g, *De Michelis et al.*, 1999]. Electron pressure is generally small compared with ion pressure (< ~1/6) in the tail plasma sheet [e.g., *Wang et al*., 2009], but becomes much larger toward smaller radial distance.

Large-scale distributions of the plasma sheet pressure and their dependencies on the solar wind condition and geomagnetic activity have been studied using in-situ plasma measurements in the magnetosphere [e.g., *Spence et al*., 1989; *Guild et al*., 2004; *Kaufmann et al*. 2004; *Wang et al*., 2007] or within the ionosphere [*Wing and Newell*, 1998]. The pressure depends on the conditions of the solar wind and interplanetary magnetic field (IMF) [e.g., *Wang et al.,* 2007]. Among all solar wind parameters, the solar wind dynamic pressure (P_{SW}) is found to strongly regulate the plasma sheet pressure [*Borovsky et al.,* 1998]. The pressure is reported to increase with decreasing distance to the Earth for all levels of activity [*Angelopoulos et al.,* 1993; *Angelopoulos,* 1996]. Away from the central plasma sheet, the plasma pressure decreases while the magnetic pressure increases so that the two remain in balance [*Fairfield et al.,* 1981; *Baumjohann et al*., 1990; *Wang et al*., 2013]. *Spence et al*. [1989] showed that the pressure magnitudes and their earthward gradients increase with increasing Kp. *Tsyganenko and Mukai* [2003] established a 2D empirical plasma pressure model based on Geotail data in the region of r = 10 to 50 R_E, controlled by the interplanetary magnetic field (IMF) and P_{SW}. Their results showed that there is no significant dawn-dusk pressure asymmetry, in line with the observed symmetry of the tail lobe magnetic fields. In addition, *Wang et al.* [2006] investigated how pressure profiles change with IMF B_Z history by using Geotail data and their results showed that the overall pressure magnitude is higher when IMF has been dominantly southward for a longer period. Their results also showed a very weak dawn-dusk asymmetry. Furthermore, *Wang et al*. [2009] showed that the equatorial plasma pressure increases everywhere as the cross polar cap potential or AE increases. The plasma sheet pressure is also well correlated with the P_{SW} with higher pressure under higher P_{SW} [e.g., *Borovsky et al*., 1998; *Wang et al*., 2013]. Since the plasma pressure distributions depend on various factors, it is important to understand quantitatively how the pressure changes in response to changes in these factors. **Therefore, the first goal of my thesis research is to use a large observational dataset from Geotail and THEMIS to established a 2 dimensional (2D) empirical pressure model under different levels of Kp and P_{SW}.**

Most of the time the earthward plasma flow is slow [e.g., *Angelopoulos et al*., 1994; *Wang et al*., 2009] so that magnetic field configuration changes to maintain force balance with the increased pressure. Increasing plasma pressure gradient in the radial direction causes stretching of magnetic field and enhanced perpendicular currents flowing azimuthally. On the other hand, FACs associated with the azimuthal pressure gradient flow into or out of the ionosphere, resulting in bending of magnetic field lines. Thus the coupling between magnetic field and plasma plays an essential role in particle dynamics and energization, in magnetosphere-ionosphere (M-I) coupling, and thus also in the plasma sheet processes causing substorms. Understanding and quantifying magnetic field mapping between the ground, thermosphere and ionosphere and the equatorial magnetosphere has long been an important goal of space physics research.

Past studies on large-scale plasma sheet pressure and magnetic field distributions [e.g., *Spence et al.,* 1989*; Kistler et al.,* 1993*; Hori et al.,* 2000*; Kaufmann et al.,* 2001] have shown that the structures and the associated plasma sheet dynamics change significantly under different solar wind and geomagnetic conditions. The pressure and magnetic field are closely coupled through force balance. The magnetic field configuration affects particles in their motion [e.g., *Speiser*, 1965] and pitch-angle distributions [e.g., *Sergeev et al*., 1983], as well as their energization [e.g., *Wang et al*., 2004]. In return the resulting plasma pressure changes the magnetic field. The coupling may lead to possible instabilities [*Xing and Wolf,* 2007, *Cheng and Liu*, 1998] that locally and temporarily disrupt the plasma and magnetic field equilibrium. These processes in the plasma sheet can connect with ionospheric processes through FACs. Therefore, magnetic field models have been widely used for evaluating various plasma sheet dynamics and instabilities with observations and simulations, as well as for mapping plasma sheet features to observed ionospheric phenomena [e.g., *Sergeev and Malkov*, 1988; *Wing and Newell*, 1998].

Most of the empirical magnetic field models [e.g., *Olson and Pfitzer,* 1974*; Tsyganenko,* 1995, 1996] were established by fitting the model magnetic field generated from a framework of postulated electrical currents to numerous observations at different locations and times. While empirical models provide realistic large-scale fields, they do not have built-in force balance between field and plasma pressure, as force balance imposes additional constraints [*Zaharia and Cheng,* 2003]. The empirical models have also been shown [e.g., *McCollough et al*., 2008] to perform well only in certain areas or under certain geomagnetic conditions. These drawbacks certainly lead to larger uncertainties in the results using these models. For example, errors in mapping latitudes can wrongly link an ionospheric phenomenon with an unrelated process or region in the magnetotail. Also, using separate plasma pressure and B-field models that have not been established to be in force balance can lead to spurious results when used in physical studies [e.g., *Zaharia,* 2008; *Xing and Wolf*, 2007]. This is why it is crucial to include both physical (force-balance) and extensive observational constraints in modeling the magnetic field.

Force balance is valid in the slow flow region of the magnetosphere, in which quasi-static equilibrium is believed to exist most of the time [*Wolf,* 1983] except for short periods of explosive activity [e.g., *Tsyganenko,* 1990]. In equilibrium, both magnetic field and plasma pressure evolve while maintaining (approximate) force balance with each other. *Tsyganenko* [2010] reconstructed the magnetospheric plasma pressure distributions in the midnight meridian plane from 4 empirical Tsyganenko magnetic field models through approximate (in a least square sense) force balance equation. They found that the T89 and T96 models give more realistic inferred pressure than do TU82 and T87, the inferred pressure being nearly isotropic in the tail, with a moderate pancake-type anisotropy in the inner magnetosphere, consistent with observations.

Present force balance magnetic field modeling includes methods using the MHD approach of numerical relaxation technique [*Hesse and Birn,* 1993; *Toffoletto et al.,* 2001], the Biot-Savart approach with magnetic field obtained from flexible current density distributions [*Wang et al.,* 2002], and various Euler-potential approaches [*Cheng,* 1995; *Zaharia et al.,* 2004; *Liu et al.,* 2006; *Gkioulidou et al.,* 2011]. In the Euler-potential approach, the magnetic field $\mathbf{B} = \nabla\alpha\times\nabla\beta$ is determined by two Euler potentials α and β. *Zaharia* [2008] developed a new Euler-potential method for solving a three dimensional (3D) plasma and magnetic field equilibrium. This new method allows for modeling larger plasma sheet domains and is less detrimental to numerical instability than other Euler-potential methods. Since knowing the 3D magnetic field configurations is the key to understand the physical processes in the plasma sheet, **the second goal of my thesis research is thus to adopt this magnetic field solver to establish a realistic 3D magnetic field configuration that satisfies the physical constraint of force balance with observed plasma pressure distributions under different levels of Kp and P_{SW}.**

1.3 Physical processes during substorm growth phase

Substorm is one of the most interesting and complex phenomena in space physics. It is a process of storage and sudden release of energy in the Earth's magnetosphere. Its development has generally been categorized into three phases: growth, expansion, and recovery. The growth phase [*McPherron,* 1970] is a period, lasting from 20 minutes to 1 hour, that starts with the southward turning of the interplanetary magnetic field (IMF) and ends at the onset of the expansion phase. Throughout the growth phase, solar wind energy is accumulating in the Earth's magnetotail; in the magnetosphere, observations of high-energy particle fluxes at geostationary orbit during the growth phase [e.g., *Baker and McPherron,* 1990] indicate strong field line stretching and the formation of a thin current sheet in the near-Earth tail [e.g., *Sergeev et al.,* 1990, 2011*; Sanny et al.,* 1994]. Understanding the plasma sheet pressure evolution is particularly important to substorms since there is continuous (~20 to 60 minutes) and enhanced solar wind energy input during the substorm growth phase [*McPherron,* 1970], and the resulting pressure increases [e.g., *Baker and McPherron*, 1990] and stretched magnetic field configurations in the near-Earth plasma sheet [e.g., *Sergeev et al*., 1990, 2011; *Sanny* et al., 1994] are believed to be crucial to the onset of the expansion phase. For example, they may become favorable to ballooning instability [e.g., *Miura et al.,* 1989; *Liu,* 1997; *Pu, et al*., 1997].

There have been only a few studies focusing on the pressure changes during substorms. *Miyashita et al*. [2000; 2001; 2003; 2009; 2010] studied the equatorial pressure and magnetic field variations around the substorm onset based on Geotail observations and found that pressure increases earthward of 12 R_E 2 min before the onset while it decreases tailward of the initial dipolarization region. Similar results were found by *Xing et al.* [2010]. In addition, *Xing et al.* [2011] used simultaneous measurements from two THEMIS probes to obtain azimuthal pressure gradients and showed that a westward azimuthal pressure gradient is enhanced before onset at r ~11 R_E. Furthermore, *Wing et al.* [2007] investigated the DMSP observations of ion pressures at the low-altitude ends of the plasma sheet and found that the pressure peaks at the inner edge of the plasma sheet during the substorm growth phase. Also, *Machida et al.* [2009] investigated the temporal development of the near-Earth magnetotail during substorms by conducting multi-dimensional superposed-epoch analysis of Geotail data. They showed that the total pressure starts to decrease around $X = -16$ R_E about 4 min before the substorm onset, and the decrease then propagates both earthward and tailward along the lobes, consistent with the results from *Miyashita et al*. [2009].

These previous studies have provided some general understanding about how pressure changes during the growth phase. However, how the pressure and its spatial variations are correlated with the intensity of a substorm and how they are affected by factors of the solar wind condition and geomagnetic activity, which are different for each substorm, remain to be determined. Therefore, **the third goal of my thesis research is to use a large observational dataset from Geotail and THEMIS and a Support Vector Regression Machine (SVRM) technique to construct empirical pressure model that allows us to quantitatively determine the changes in large-scale equatorial plasma sheet pressure distributions during the growth phase in response to different driving factors.**

Furthermore, where substorm onset starts in the plasma sheet has remained one of the outstanding substorm questions, and is critical for differentiating substorm onset models, such as the near-Earth neutral line model [*Baker et al*., 1996, *Shiokawa et al*., 1997], the current disruption model [*Lui*, 1996], and the more recent proposal of a connection between flow bursts and a near-Earth onset instability [*Nishimura et al.,* 2010]. Previous studies have used observations together with magnetic field model to try to determine the onset location. For example, *Kubyshkina et al.* [2011] analyzed an isolated substorm on 29 March 2009 with THEMIS satellites and ground-based All sky Imagers combined with an adjusted time-varying magnetic field model, and they found the equatorial mapping of substorm breakup to be at a radial distance of ~22 R_E, which is about 10 R_E tailward of the mapped location using the Tsyganenko 96 model. *Sergeev et al.* [2012] used a dynamically adapted magnetospheric model combining with isotropic boundaries observed by low-latitude satellites and found that the most equatorward locations of pre-breakup arcs mapped to 8-10 R_E in the plasma sheet. *Chu et al.* [2015] used a dynamic magnetospheric model with real-time substorm currents from their inversion model [*Chu et al.*, 2014] and found that the flows at 9-10 R_E mapped to pre-breakup arcs. The differences and uncertainties in these mappings may reflect the lack of a realistic magnetic field model designed for the substorm growth phase. A solution to this issue would be to determine onset location in the plasma sheet through mapping of initial auroral brightening via a realistic magnetic field model for the substorm growth phase.

For current disruption model, ballooning/interchange instability [*Cheng and Qian*, 1994, *Cheng and Liu*, 1998] has been suggested as a plausible mechanism for initiation of substorm onset in the high-β plasma sheet [*Hurricane*, 1997; *Pu et al*., 1997; *Lee and Wolf*, 1992; *Cheng and Lui*, 1998]. Thus, identifying the initiation of the ballooning instability in the plasma sheet may help the further understanding of the onset processes. Explicit ballooning instability criteria in the MHD regime has been used to investigate the stability of the growth phase plasma sheet [e.g, *Xing et al.,* 2013]. Since ballooning instability is determined by the plasma and magnetic field spatial variations, accurate evaluation of the ballooning instability requires a realistic 3D force-balanced plasma pressure and magnetic field configurations.

Therefore, accurate evaluation of these substorm processes relies on knowing the realistic 3D magnetic field configurations. However, such evaluations cannot be provided with sufficient accuracy or as a function of growth phase development by currently available empirical magnetic field models, which have been shown [e.g., *McCollough et al*., 2008] to perform well only in certain areas or under certain geomagnetic conditions. Therefore, **the fourth goal of my thesis research is to establish the very first empirical model that is capable of reliably describing the evolution of 3D force-balanced plasma pressure and magnetic field**

configurations during the substorm growth phase and to apply the model to substorm events to examine underlying physical processes during the growth phase.

1.4 Earth's magnetic field modeling

Magnetic field model is a very important tool in magenetospheric physics. The interaction between the high-altitude magnetosphere and the low-altitude ionosphere-thermosphere system results from coupling of the particle dynamics and electric current between these two regions through the magnetic field lines that connect them. Therefore, understanding and quantifying magnetic field mapping between the ground/thermosphere/ionosphere and the equatorial magnetosphere has long been an important goal of space physics research. Here, I briefly review three different approaches of establishing 3D global magentospheric magnetic field modeling in the space physic community.

1.4.1 Equilibrium models

The goal of magnetospheric equilibrium models is finding magnetospheric configurations in which the magnetic pressure and tension forces are equilibrated by magnetospheric plasma pressure gradient forces under the slow flow (subsonic flow) approximation [*Wolf,* 1983] which is valid at most times except for periods of explosive activity [e.g., *Tsyganenko* 1990]. Furthermore, if the time scale of global magnetic field variation is not too short, one could describe the temporal evolution of the magnetosphere as being a series of still snapshot, each one of them a unique quasi-static equilibrium state. The slow convection during quiet magentospheric times and even the substorm growth phase can be described as sequences of quasi-static equilibrium [e.g., *Kropotkin and Lui,* 1995].

Several approaches to the equilibrium problem have been developed in the past. One set of approaches analyze the magnetosphere close to the Earth, where the magnetic field is close to a dipolar field, and the plasma equilibrium in either a dipole or a perturbed dipole file has been studied [e.g., *Zavriyev and Hasegawa*, 1989]. On the other hand, many studies [e.g., *Wiegelmann and Schindler*, 1995; *Birn and Hesse*, 1991] investigate the magnetotail equilibrium at distances larger than 20 R_E, where the so called "tail approximation" is valid, whereby variations of physical quantities in one direction (north-south) are much larger than variations in the other two directions. A few studies [e.g., *Cheng* 1992; *Becker et al.*, 2001] incorporated both the near-Earth and farther regions of the magnetosphere in equilibrium modeling, but in 2D only, thus missing important effects such as the field-aligned current formation.

Recently, *Zaharia* [2008] built up a 3D force-balanced magnetic field model from dayside of 6 R_E to nightside 18.5 R_E. The magnetic field model of *Zaharia* [2008] obtains the magnetic field by solving the single-fluid force balance equation $\mathbf{J}\times\mathbf{B} = \nabla\cdot\mathbf{P}$ in terms of Euler potentials as $B = \nabla\alpha \times \nabla\beta$, where **P** is plasma pressure and **J** is the current density.

1.4.2 Time-dependent models

Rather than just finding equilibrium configurations, the time-dependent models try to describe the time evolution of the magnetospheric plasma. The representative models are global 3D magnetohydrodynamics (MHD) simulations [e.g., *Raeder et al.,* 1995; *Clauer et al.*, 2000]. The global MHD simulations usually have poor resolution in many important regions in the near-Earth magnetosphere. This is partly due to the fact that they are intended to be global. The MHD models, assume an adiabatic evolution, in which the quantity PV^r (P being the plasma pressure, while V is the magnetic flux volume per unit flux) in conserved. However, observations [e.g., *Borovsky et al.,* 1998] show that this quantity is in fact not conserved at r < 15 R_E, which shows that plasma transport in the near Earth region might be an issue more complex than being described by adiabatic convection alone.

Another type of time dependent models is the convection models which are more suitable for the inner magnetosphere. The time-dependent guiding center distributions functions are obtained by following the drift motion of the particles guiding centers in a given magnetic field configuration. One example of convection model is the Rice Convection Model (RCM) [*Wolf* 1983; *Toffoletto et al.,* 2001], which includes an ionosphere with finite conductance, as well as multi-fluid representation of the magnetospheric plasma population.

1.4.3 Empirical models

Empirical models usually prescribe the magnetospheric magnetic field by adding to the Earth's internal dipolar field the magnetic fields produced by a framework of postulated magnetospheric currents, including the ring current, cross-tail current and field-aligned currents, representing the major observed current systems inside the magnetosphere, plus surface currents flowing on the magnetopuase surface that shield the space outside from the magnetospheric currents. The intensity and spatial characteristics of the postulated currents are parameterized, with the parameters found by fitting the magnetic field produced by the totality of the currents to field data from many observations, covering a large magnetospheric region but taken at different times under different solar wind conditions. Due to the calibration of the empirical models against large field databases collected over large periods of time, their magnetic field is intended to represent a statistical picture of the magnetispheric field, such as large scale and time averaged magnetic field configurations [e.g., *Tsyganenko* 1989; 1995; 1996]. Current empirical magnetic field models have been shown [e.g*., McCollough et al*., 2008] to perform well only in certain areas or under certain geomagnetic conditions. While empirical models provide realistic large-scale fields, they are not constrained physically by the force balance between magnetic field and plasma pressure [*Zaharia and Cheng*, 2003].

In my thesis research, the equilibrium model adopted from Zaharia [2008] combined with empirical plasma pressure model is used to model the 3D plasma and magnetic field configurations for different Kp and P_{SW} and for during substorm growth phase. The observed magnetic field is only used for validating the model results.

1.5 Objective of thesis and thesis organization

Accurate evaluation of physical processes during substorm growth phase, including formation of field-aligned currents (FACs), isotropization by current sheet scattering, and localized instabilities, relies on knowing the realistic 3 dimensional (3D) magnetic field configurations. However, such evaluations cannot be provided with sufficient accuracy or as a function of growth phase development by currently available empirical magnetic field models, which have been shown [e.g*., McCollough et al*., 2008] to perform well only in certain areas or under certain geomagnetic conditions. Therefore, **the ultimate goal of my Ph.D. research is to establish the very first empirical model that is capable of reliably describing the evolution of 3D force-balanced plasma pressure and magnetic field configurations during the substorm growth phase, and apply this modeling to investigate the underlying physics, such as dynamics of proton aurora due to current sheet scattering, ballooning stability of the plasma sheet configurations, and the substorm onset location in the plasma sheet.**

The work principle of my research is to first establish a 2D plasma sheet pressure model from observation, and then use the model pressure as input to the 3D force-balanced magnetic field model adopted form *Zaharia* [2008] to obtain the 3D plasma and magnetic field configuration. So the major tasks for my research include (1) process and statistically analyze a very large observational dataset from THEMIS (2007-2010) and GEOTAIL (1995-2005) satellites; (2) establish an empirical 2D plasma pressure model by using analytical form under different Kp and P_{SW} to provide the pressure distributions for modeling the 3D force-balanced magnetic field; (3) obtain the 3D plasma and magnetic field configurations from the force-balanced magnetic field model; (4) develop a novel empirical substorm growth phase plasma sheet pressure model by using the SVRM technique and evaluate the model accuracy; (5) establish the very first 3D substorm growth phase force-balanced magnetic field model by using the pressure model as input to obtain the 3D plasma, magnetic field and current system and evaluate the model accuracy; (6) apply the model to substorm events study to examine some underlying physical processes during the growth phase. The work (1), (2), (3) are the initial work to couple plasma pressure model with the magnetic field solver adopted from *Zaharia* [2008] which is the preparation for my substorm growth phase modeling. The uniqueness of my modeling is that the magnetic field is computed solely from plasma pressure distributions through the physical constrain of force balance, and magnetic field observations are only used to validate the model magnetic fields.

In this thesis, the observational dataset and the work principle of the pressure and magnetic field modeling will be introduced in chapter 2. Here, for the plasma sheet pressure model, we have developed two approaches: (1) use analytical function and (2) use he Support Vector Regression Machine (SVRM) technique to model large-scale pressure profiles. Some important features may be overestimated or underestimated due to the choice of function forms. Therefore, we improved the modeling accuracy by using SVRM to establish empirical pressure distributions that can as best represent the observations as possible.

In chapter 3, the results of model dependence on Kp and P_{SW} will be investigated. Here the force-balanced magnetic field configurations under different levels of Kp and P_{SW} are obtained using the observed equatorial isotropic plasma pressure distributions as input to the 3D equilibrium magnetic field model of *Zaharia* [2008]. We chose Kp since it is represent the convection intensity and its 3-hr average is more likely to reflect equilibrium conditions under different levels of solar wind driving than other shorter time-scale indices that reflect specific disturbances. We also chose P_{SW} since it has been shown to strongly regulate the plasma sheet pressure [*Borovsky et al.*, 1998]. In contrast to the simple pressure input used in *Zaharia* [2004], which is based mainly on a quiet time empirical 1-D pressure profile along midnight, here we have used realistic plasma pressure profiles obtained from an empirical 2-D pressure model established in *Wang et al.* [2013] using Geotail and THEMIS observations. As discussed in *Wang et al.* [2013], with these more realistic plasma pressure profiles, we obtained magnetic field configurations in fairly good agreement with observations. In this Chapter, the characteristics of the force-balanced magnetic field and how it changes with Kp and P_{SW} is firstly described. The stability of the 3D pressure and magnetic field configurations against interchange instability and the major differences between our magnetic field and the non-force-balanced Tsyganenko 89 (T89) magnetic field model [*Tsyganenko*, 1989] are discussed after.

In chapter 4, the current sheet scattering of 1-30 keV ions are estimated using the force-balanced magnetic field under different Kp and P_{SW} levels, and the equatorial IB from the THEMIS observations and low-altitude IB from the FAST measurements are identified. In addition, the role of current sheet scattering through the model-observation comparison is determined. A step further, the differences from the predictions using non force-balanced Kp-dependent Tsyganenko 87 (T89) model are briefly discussed to demonstrate the importance of force balance.

In Chapter 5, the evolution of 3D plasma sheet pressure distributions and magnetic field configurations, as well as the current system, during the substorm growth phase, is firstly investigated. Then the model accuracy is evaluated by comparing model results with observations within the plasma sheet. In addition, the plasma pressure and magnetic field responses to different solar wind dynamic pressure (P_{SW}) and sunspot number are also discussed. By applying our magnetic field model to a substorm event, we evaluate the dynamics of proton aurora due to current sheet scattering by comparing the magnetospheric ion isotropic boundaries (IBs) with proton auroral observations [e.g., *Ganushkina et al.* 2005; *Shevchenko et al.* 2010; *Yue et al.* 2014], and examine ballooning instability of the plasma sheet configurations, and determine the onset location in the plasma sheet by mapping the ionospheric onset location. The summary and conclusion will be present in Chapter 6.

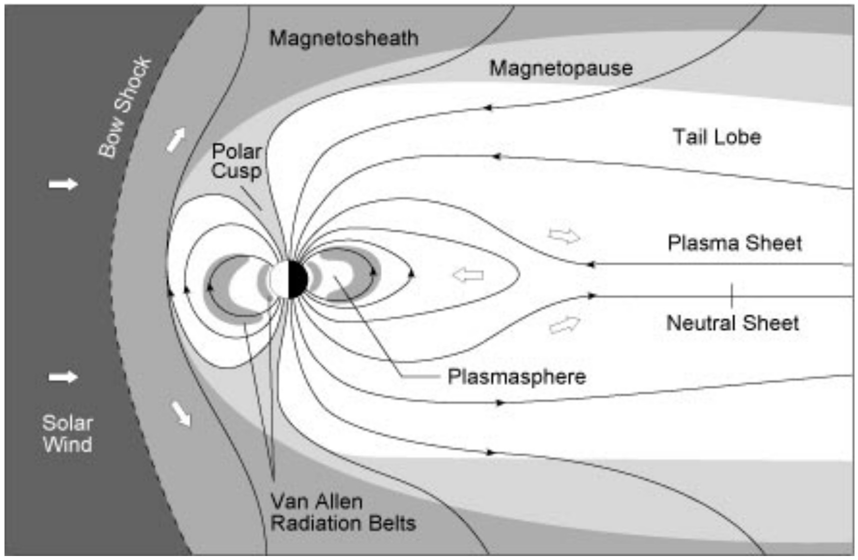

Figure 1.1 Overview of the Earth's magnetosphere. (Source of this image is from http://ase.tufts.edu/cosmos/print_images.asp?id=29)

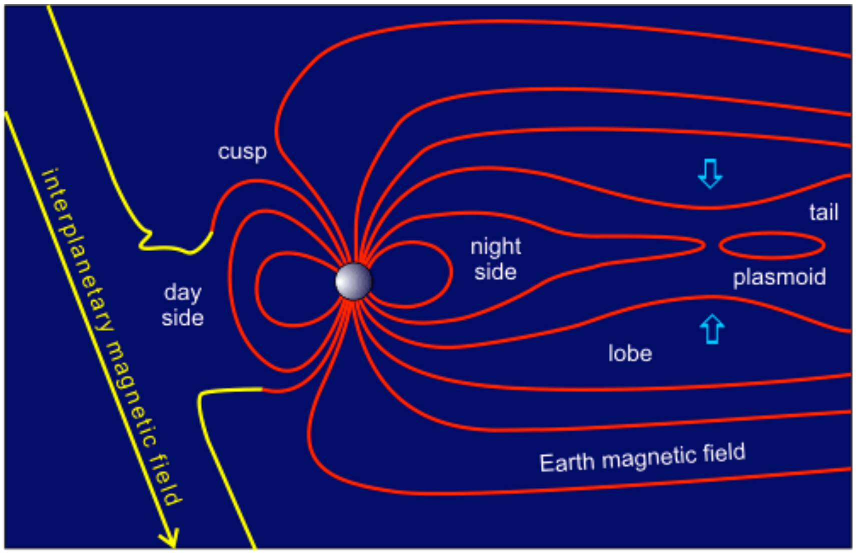

Figure 1.2 Sketch plot of magnetic field lines reconnection. (Source of this image is from http://www.aldebaran.cz/astrofyzika/plazma/reconnection_en.html)

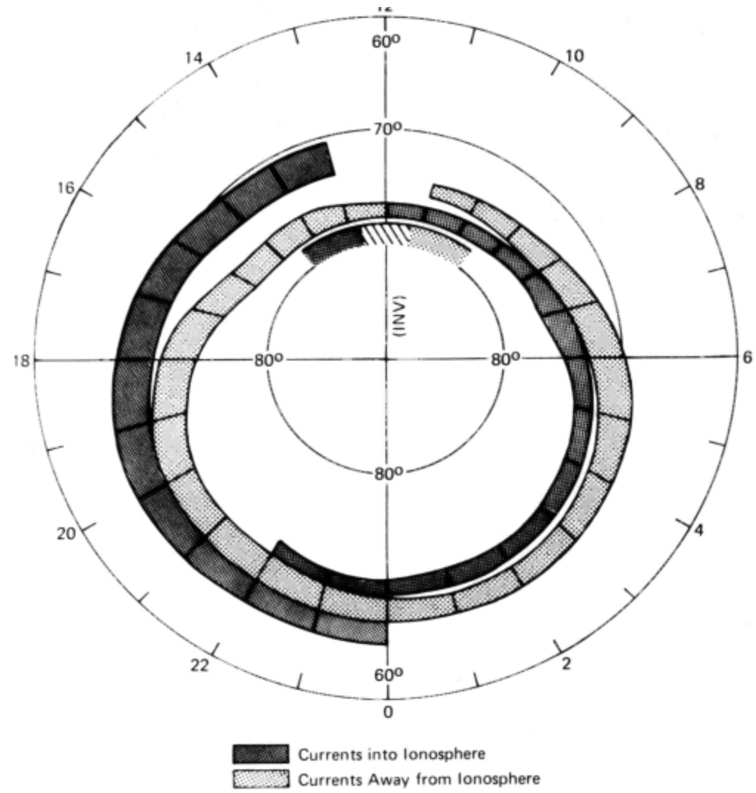

Figure 1.3 Region-1 and Region-2 field-aliged currents on top of the ionosphere. The center of the circle is the magentic pole, while the numbers show magentic local time (MLT) (from [Iijima and Potemra, 1976a])

CHAPTER 2 | Observational Data and Modeling Approach

In this chapter, the observational datasets used for the whole thesis research is first described. Then the modeling framework for constructing 3D forced-balanced plasma and magnetic field configurations based on observed pressure is introduced.

2.1 Observational data

Observations from two NASA missions, Geotail and THEMIS, are used in the study. Geotail data from January 1, 1995 to December 31, 2005 (data after 2006 is not used since Geotail stayed mostly at high latitudes in the magnetotail after 2006), and THEMIS data from March 23, 2007 to April 30, 2010. Aberrated GSM coordinates (with the aberration angle determined by one hour averaged solar wind velocity) are used. Geotail covers regions from r ~8 to 30 R_E. In the selected THEMIS periods, three of the five THEMIS spacecraft cover regions inside r ~12 R_E, while the other two cover regions inside r ~30 R_E. Therefore, by combining these two data sets we obtain observations of the magnetosphere from r ~30 R_E on the nightside to the dayside magnetopause. Plasma data from two instruments onboard Geotail are used: the ion and electron data from the Low Energy Particle (LEP) instrument [*Mukai et al.*, 1994] that covers the ion energy range from 21 eV/q to 44 keV/q and the electron energy range from 43 eV to 41 keV, and the proton data from the Energetic Particles and Ion Composition (EPIC) instrument [*Williams et al.,* 1994] that covers the ion energy range from 46 keV to 3005 keV (EPIC only measures > 32 keV and > 110 keV integral electrons so electron moments is not available). Magnetic field data is from the magnetic field (MGF) experiment [*Kokubun et al.,* 1994]. The ion moments are from a summation of the LEP and EPIC data and the electron moments are from the LEP data.

For THEMIS, the ions and electrons are measured by an electrostatic analyzer (ESA, 0.006 – 20 keV/q for ions and 0.007 – 26 keV for electrons [*McFadden et al*., 2008]) and a solid state telescope (SST, 35 keV – 6 MeV for ions and 30 keV – 6 MeV for electrons). Full distributions are used with time resolution of a few minutes. The total plasma moments are a summation of the ESA and SST moments. The magnetic field is measured by the FGM instrument [*Auster et al*., 2008]. Sunlight contamination to the SST is removed. The penetrating radiation contamination is removed from the ESA data by subtracting the minimum count value within the ESA energy ranges (see *Wang et al.* [2011] for more details). However, there is no reliable method to remove the penetrating radiation contamination to the SST. Since SST pressure becomes dominant with decreasing radial distance, pressure becomes less reliable inside r ~7 R_E where radiation contamination may be stronger. For ions, there is energy gap (from ~20 to 28 keV) between the highest ESA channel and the lowest SST channel. Fluxes within this energy gap are interpolated from the fluxes of the two nearby energy channels. For both Geotail and THEMIS, plasma pressure is a summation of ion and electron plasma pressure (note that Geotail only provides electron pressure from electrons below 40 keV, but pressure contribution from > 40 keV electrons is negligible even in the inner magnetosphere). The plasma pressure is assumed isotropic.

Note that there is no time overlap for the selected Geotail and THEMIS data. The overall THEMIS fluxes in the spatial overlap region are found to be smaller than the Geotail fluxes (up to a factor of 2), likely due to the solar wind density during the selected THEMIS period (average ~4 cm^{-3}) being lower than that during the selected Geotail period (average ~6.5 cm^{-3}). Nevertheless, the effect of P_{SW} on the plasma pressure is corrected when normalizing the pressure to a fixed P_{SW}. The solar wind parameters used in this study is from OMNI data, which has been propagated to the nose of the Earth's bow shock.

2.1.1 Data selection criteria

The equatorial plane is the center of current sheet where the radial component of magnetic field reverses its direction. At a fixed (X, Y) location, plasma pressure (P_p) is normally the largest while total magnetic pressure ($P_{b,t} = (B_x^2 + B_y^2 + B_z^2)/2\mu_0$) is the smallest at the equatorial plane. With increasing Z distance from the current sheet, the plasma pressure decreases while total magnetic pressure increases, resulting in a decrease in the plasma beta ($P_p/P_{b,t}$). Since it is not possible to determine the actual Z distance to the current sheet from a single point observation, the plasma beta is often used to indicate how far a satellite is away from the current sheet.

From the force balance equation, $\nabla P_p = 1/\mu_0\, (\nabla\times\mathbf{B})\times\mathbf{B}$, in the Z direction, one can obtain $P_p + P_b - 1/\mu_0 \int_0^z (\partial B_z/\partial x \cdot B_x + \partial B_z/\partial y \cdot B_y) dz = P_{p,eq}$, where $P_b = (B_x^2 + B_y^2)/2\mu_0$ is the radial magnetic pressure (note that P_b has no Bz component so that it is different from $P_{b,t}$), and $(1/\mu_0 \int_0^z (\partial B_z/\partial x \cdot B_x + \partial B_z/\partial y \cdot B_y) dz)$ is the magnetic curvature term. If the magnetic curvature term is zero, then total pressure $P_t = P_p + P_b$ at a fixed (X, Y) location should be a constant in the Z direction, thus is independent of the plasma beta. The magnetic curvature term is in general very small in the vicinity of the current sheet but becomes larger with increasing Z distance (decreasing plasma beta) and is larger in a more dipolar field.

Figure 2.1 shows how P_p, P_b , and P_t change with the plasma beta at different radial distances and MLTs. In general, in the region outside $r \sim 7\ R_E$ and when the plasma beta is larger 1, P_t is almost independent of the plasma beta and is quite close to $P_{p,eq}$, while P_p decrease substantially with decreasing plasma beta. Therefore in this study, in the region outside of $r = 7\ R_E$ only data with the plasma beta ≥ 1 were selected and the observed P_t is assumed to equal to $P_{p,eq}$. Inside r ~7 R_E, with decreasing r the plasma beta decreases quickly to below 1 because of sharply increasing magnetic field strength. Figure 2.1 shows that inside r ~7 R_E both P_t and P_p decrease with decreasing plasma beta because of increasing curvature term, but the decrease of P_t is much less significant than that of P_p. Thus for $r < 7$ R_E we only selected P_t with the plasma beta ≥ 0.1 and used it to represent $P_{p,eq}$, with the caution that this leads to underestimates of the actual $P_{p,eq}$. These plasma beta lower limits were so chosen in order to obtain as best estimate of $P_{p,eq}$ as possible and to collect sufficient data points for establishing a spatial distribution of $P_{p,eq}$ with statistical significance. Additionally, to avoid periods of fast flows when the above force balance assumption is less valid, we included only data with perpendicular and parallel plasma bulk flow smaller than 100 km/s.

2.2 The plasma pressure model

A few empirical pressure models have been developed to describe the spatial distribution of plasma pressure. *Spence and Kivelson* [1993] developed an analytical form for the midnight pressure profile from the tail to the inner magnetosphere during quiet times. Using Geotail data, *Tsyganenko and Mukai* [2003] established a 2D model for plasma pressure with dependence on the IMF and P_{SW} for the region of r = 10 to 30 R_E. Since 2007, five spacecraft from the THEMIS mission have extensively surveyed plasma pressure near the equator in the region of r ~2 to 12 R_E. These datasets allow us to construct empirical pressure model with more extensive spatial coverage.

2.2.1 Parametric method—analytical form

In this part, the goal is to establish an empirical model of 2D plasma pressure distributions at the equator as a function of Kp and P_{SW} based on observed plasma pressure. We chose Kp over other indices because it indicates global magnetosphere activity, which corresponds to global changes in the plasma and magnetic field configurations. As shown in Figure 2.2, higher Kp well indicates larger solar wind driving (as shown by higher cross polar-cap potential) as well as more active magnetosphere responses in the inner magnetosphere (more negative Dst) and in the plasma sheet (higher AE). The lower Dst is caused by stronger ring current, and thus more substantial magnetic field changes, in the inner magnetosphere. Higher AE indicates stronger ground disturbance around the auroral zone connecting to the plasma sheet, which is mainly attributed to the enhanced ionospheric and field-aligned currents. Kp is also found to be well correlated with the ionosphere isotropic precipitation boundary [*Newell et al*., 1998], which has been shown to give good indication of magnetic field line stretching [*Sergeev and Gvozdevsky*, 1995].

In addition, P_{SW} has been shown to strongly regulate the plasma sheet pressure [*Borovsky et al*., 1998]. The plasma sheet P_p is highly correlated with P_{SW}. We found that the correlation between P_t and P_{SW} is even higher than that between P_p and P_{SW}. To approximately correct the effect of P_{SW} in order to obtain a spatial P_t distribution corresponding to the same P_{SW}, we first did a linear power law fit to the correlation between P_t and P_{SW} within each 1 $R_E \times 1$ R_E X-Y area. Using the fit, we then obtained normalized P_t ($P_{t,n}$) corresponding to two P_{SW} levels: P_{SW} = 1.5 and P_{SW} = 3 nPa. This normalization was done for all areas outside r = 7 R_E (so inside r = 7 R_E, $P_{t,n}$ is the same as the observed P_t). Finally, we sorted $P_{t,n}$ to six Kp levels from Kp = 0 to 5 (there were not enough data for Kp > 6).

Here, we fit the distribution of the normalized pressure (P_n) to a model pressure (Pm) described by an analytic form as below:

$$P_{fit} = e^{b_1 R}\left[b_2 + b_3 \sin(\varphi) + b_4 \sin^2(\varphi) + b_5 \cos^2(\varphi)\right] +$$
$$R^{b_6}\left[b_7 + b_8 \sin(\varphi) + b_9 \sin^2(\varphi) + b_{10} \cos^2(\varphi)\right] + b_{11} \tag{1}$$

where r is the radial distance in R_E and φ is the azimuthal angle (0^o at noon, 90^o at dusk, 180^o at midnight, and 270^o at dawn). b_1 to b_5 mainly control the pressure in the inner magnetosphere while b_6 to b_{10} determine the plasma sheet pressure, b_{11} is the pressure residual. The parameters for the best fit were obtained by minimizing the difference between P_n and P_m.

The parameters for the best fit were obtained by minimizing the difference between $P_{t,n}$ and P_m using the Matlab fminsearch function, which uses the Nelder-Mead simplex algorithm as described in *Lagarias et al.* [1998] to find the minimum of a scalar function of several variables starting with an initial estimate. The scalar function in our case is defined as $\Sigma[\text{weight}\cdot(P_m\text{-}P_{t,n})^2]$, where weight is the number of measurements within each (X, Y) bin/total number of the measurements. Different initial estimates can give different fitting profiles but with quiet similar correlation coefficients and fitting errors between $P_{t,n}$ and P_m. A profile with lower fitting error may not necessarily give better overall representation of the observed profile because the lower error may simply be a result of better fitting in more localized region. Thus for each Kp-P_{SW} pressure distributions, we first conducted the fitting with many initial estimates. We then visually compared the fitted profiles with the observations and selected the one that gives the best large-scale representation. The values of the fitting parameters and the errors (90% confidence intervals) for each parameter estimated using the bootstrap method for different Kp are listed in Tables 2.1 and 2.2 for P_{SW} = 1.5 and 3 nPa respectively, together with the linear correlation coefficients and the root mean square (RMS) and mean fitting errors. The correlation coefficients for the Kp = 5 pressure are lower and errors are substantially larger because of relatively fewer available data than for the lower Kp cases.

Note that the goal is to use one analytical function to give model representatives of observed large-scale pressure distribution for different Kp and P_{SW} levels, the function is certainly not unique and the function terms do not have to be orthogonal to each other. We have tested many function forms, including those having only orthogonal terms, such as $sin(\varphi)$ and $\cos(\varphi)$, or terms of higher order, such as $sin^3(\varphi)$. Among the tests, the function (1) is the one that has smallest overall fitting errors for all the Kp and P_{SW} levels. The values of each fitting parameters do not present actual physical meaning of pressure and are not found to change regularly with increasing Kp or P_{SW}. It is the summation of all parameters that gives the meaningful model pressure profiles. Therefore, despite that some of the fitting parameters may have large jumps in their values between neighboring Kp or P_{SW} cases, P_m does not have such jumps and it change systematically with increasing Kp and P_{SW}.

2.2.1.1 Equatorial pressure distributions

Figure 2.3 shows the unnormalized total pressure (P_t), plasma density (N), and ion temperature (T_i) for Kp = 1 and 3 within two P_{SW} ranges ($0 < P_{SW} \leq 2$ nPa and $2 < P_{SW} \leq 4$ nPa). As Kp increases from 1 to 3, the overall T_i increases (in the region $-10 < X < -30$ R_E and $|Y| < 15$ R_E) by a factor of ~1.7 to 2.4 while N decreases by a factor of ~0.66 to 0.78. As a result of the opposite N and T_i changes, P_t only becomes slightly higher (a factor of < 1.2). The higher T_i during higher Kp is likely due to larger particle energization by stronger solar wind driving and convection electric field, as indicated by the higher cross polar cap potential drop at higher Kp shown in Figure 2.2. The decrease in N, on the other hand, is possibly due to stronger convection pushing the colder plasma sheet population toward the two flanks [*Wang et al.*, 2010]. The changes due to P_{SW} are quite different from the Kp effect. As P_{SW} increases by a factor of 2, the overall N increases by a factor of 2 to 2.5 while T_i changes only slightly by a factor of 0.8 to 1, resulting in an increase of P_t by a factor of ~1.6. The higher plasma sheet density and pressure is mainly a result of magnetosphere compression by the higher P_{SW}.

Figure 2.3d shows that electron contribution to the total plasma pressure increases with decreasing *r*. The electron pressure becomes important (> 0.2 of the total plasma pressure) inside *r* ~15 R_E and is more significant in the post-midnight than pre-midnight sector due to dawnward magnetic drift of higher energy electrons. Ion pressure, on the other hand, is relatively higher in the pre-midnight sector because high-energy ions magnetic drift toward dusk. The opposite dawn-dusk asymmetries for ions and electrons result in relatively dawn-dusk symmetric total plasma pressure.

Figure 2.4 shows how the midnight radial profiles and azimuthal profiles for $P_{t,n}$ and P_m change with Kp at r = 11-12 R_E under two P_{SW} levels. It can be seen that P_m profiles well represent the observed large-scale profiles and their systematical changes with increasing Kp and P_{SW}. Figure 2.5 shows direct and detailed comparisons of $P_{t,n}$ and P_m in their equatorial distributions and their radial and azimuthal profiles for 4 selected levels (P_{SW} = 1.5 and 3 nPa and Kp = 1 and 3). The fairly good overall agreement shown in Figures 2.4 and 2.5 (with the exception of Kp = 5 cases in the tail plasma sheet as indicated by the larger errors in Table 2.1 and 2.2) indicates that observed pressure is well represented by the model pressure. Note that there is a discontinuity in $P_{t,n}$ at *r* ~7 R_E, which is artificially due to the P_{SW} normalization being done only to data outside *r* = 7 R_E. The model pressure inside *r* = 10 R_E and its change with Kp are also consistent with previous AMPTE/CCE observations [*Lui*, 2003].

2.2.1.2 Pressure gradients and comparison with simultaneous THEMIS measurements

It is the pressure gradient in the force balance equation that determines a magnetic field configuration. Figure 2.6a shows the radial profiles of the radial pressure gradient (*dP/dr*) of P_m at midnight. Like the pressure profiles shown in Figure 2.5, pressure gradient increases with decreasing *r* with an order of magnitude increase from $X = -30$ to -10 R_E. The changes of *dP/dr* with Kp and P_{SW} vary with *X*. As Kp changes from 1 to 3, *dP/dr* increases by a factor of ~1.2 at $X = -30$ R_E while a larger increase of a factor of ~1.5 is seen at $X = -10$ R_E. An opposite *X* dependence is seen associated with the P_{SW} effect. As P_{SW} doubles from 1.5 to 3 nPa, a larger increase is seen at larger *r* (a factor of ~1.3 to 1.4 at $X < -20$ R_E) than at smaller *r* (a factor of ~1.2 at $X = -10$ R_E). This is due to the fact that P_t in the tail is better correlated with P_{SW} than in the near-Earth.

Figure 2.6b shows the MLT profiles of the azimuthal gradient (*dP/dφ*) of P_m at $r = 11.5$ R_E (positive *dP/dφ* means an eastward pressure gradient). $dP_m/d\varphi$ is in the order of 10^{-4} nPa/R_E, which is two to three orders of magnitudes smaller than *dP/dr*. Therefore, statistically there are almost no azimuthal pressure variations. This is different from the empirical pressure profile of *Tsyganenko and Mukai* [2003], which has relatively lower pressure at midnight than at other MLTs.

It is important that our model pressure from the statistical pressure profiles can provide realistic pressure gradients. As in *Xing et al.* [2009; 2011], instantaneous pressure gradients can be computed from the pressure simultaneously measured by any two of the five THEMIS spacecraft. To compute a pressure gradient from a THEMIS pair, we selected a pair with both spacecraft being in the region of plasma beta ≥ 1 and $|V_\perp| \leq 100$ km/s. To select data for reliable assessment of *dP/dr*, we required the MLT separation between the two spacecraft to be $\leq 5^o$ (1/3 MLT) and the radial separation (radial distance is $\sqrt{X^2 + Y^2}$) to be between 0.9 and 5 R_E and also be larger than their azimuthal separation. For *dP/dφ*, their radial separation has to be between 0.5 and 1 R_E and be smaller than their azimuthal separation. P_t is used to represent the equatorial plasma pressure, but without the normalization to a fixed P_{SW}. Despite three of the THEMIS spacecraft staying closely to each other most of the time, there are only few short periods when their alignment satisfies the above criteria. Nevertheless, data from these periods are valuable for evaluating our model pressure gradients.

The pressure gradients observed by the THEMIS pairs are also shown in Figure 2.6. Each red dot represents an average of the pressure gradients within a 10-minutes period with the standard deviation indicated by the red vertical line. For *dP/dr*, most of the observed gradients are quite close to the model gradients, indicating that the P_m can give quite realistic radial pressure gradients. For *dP/dφ*, the magnitude of each of the observed gradients is much larger than the model gradients and can be even comparable to *dP/dr*. However, the observed gradient points are scattered around zero, implying that statistically there would be no significant azimuthal gradients, as predicted by P_m.

2.2.1.3 Comparison with previous empirical models

Spence and Kivelson [1993] established an empirical model for the midnight plasma pressure for r = 2 to 35 R_E for Kp = 1 using the plasma sheet observations from *Spence et al.* [1989]. A more sophisticated empirical model for r = 10 to 50 R_E controlled by the solar wind conditions (IMF and P_{SW}) was established by *Tsyganenko and Mukai* [2003] using Geotail observations. However, pressure from ions above 40 keV and from electrons is not included in the *Spence and Kivelson* pressure (P_{SK}) nor the *Tsyganenko and Mukai* pressure (P_{TM}).

Figure 2.7a shows the comparisons between our model pressure (P_m) and those from the above two models. The IMF and P_{SW} inputs for the P_{TM} for Kp = 1 and 3 are specified using the median values indicated by the vertical dashed lines in Figure 2.2. For Kp = 1 and P_{SW} = 1.5 nPa, P_{SK} is similar to P_{TM} but both are almost a factor of 2 smaller than P_m. For Kp = 3, P_m remains a factor of ~2 higher than P_{TM}. Nevertheless, P_m and P_{TM} both show that plasma sheet pressure increases by a factor of ~1.6 as P_{SW} doubles.

The azimuthal variations of P_m at r = 11.5 and 17.5 R_E are compared with those of P_{TM} in Figures 2.7b and 2.7c. P_{TM} shows clear azimuthal pressure gradient with relatively lower pressure at midnight. In addition to not including pressure from ions above 40 keV and electrons, the reason for relatively lower pressure from P_{SK} and P_{TM} than our results is also likely due to data selection. Plasma pressure decreases with decreasing plasma beta. Even for plasma beta > 1, plasma pressure away from equator can be substantially lower than the pressure right at the equator. P_{SK} included all plasma pressure data regardless of the plasma beta and P_{TM} used plasma pressure data with plasma beta ≥ 1, thus they are lower than our pressure that used total pressure with plasma beta ≥ 1 in the plasma sheet. Since the magnetic field is more stretched at midnight compared with other MLTs, plasma pressure falls off more quickly with decreasing plasma beta. This difference likely causes P_{TM} to be lower at midnight than other MLTs even though the same beta ≥ 1 criterion was used at all MLTs. The azimuthal pressure gradient is important to the generation of field-aligned currents (FACs). Thus the azimuthal pressure gradient from P_{TM} may give rise to unrealistic FACs.

2.2.2 Non-parametric method—support vector regression machine

In this part, we have only used the dataset during substorm growth phase in order to develop the substorm growth phase plasma sheet pressure model, which is then used in modeling the 3D substorm growth phase evolution of plasma and magnetic field configurations.

We investigate the plasma sheet pressure change during substorm growth phase. Here, we have used a substorm list from *Hsu and McPherron* [2012]. The onset of each substorm was identified by a sharp drop in AL index (more than 100 nT in 20 min). There are more than 20,000 substorms thus identified from 1995 to 2010. The plasma pressure data during the substorm growth phase (here we assume that the substorm growth phase is the 60 min period before a onset) are then collected.

2.2.2.1 Factors controlling the growth phase pressure

Figure 2.8a shows the statistical results of cross polar cap potential drop (CPCP, calculated by using Weimer model [*Weimer,* 1995]) and AE variations in 2 hours prior to and 2 hours after substorms onset for three ranges of substorm intensity (in this study, we use the maximum AE value, AE max, during the 40 min period after an onset to indicate the intensity of a substorm). The median values of CPCP and AE increase as increasing substorm intensity. CPCP gradually increases while AE shows little change during substorm growth phase. And CPCP peaks around the substorm onset then gradually decays. While AE shows a sharp increase after onset, peaking around 30 min later, then gradually decays. Figure 2.8b and 2.8c show the number of data points and the corresponding equatorial medians of the growth phase pressure distributions for the same three different substorm intensities as shown in Figure 2.8a. Only data points with plasma beta larger than 1 were used (total ~1,250,000 points). It can be seen that the overall pressure is higher for more intense substorm. To find out what factors can be related to a larger increase in plasma sheet pressure during the growth phase to result in a more intense substorm, we investigated how the growth phase pressure is correlated with different solar wind parameters and with the time since the previous substorm.

Figures 2.9a to 2.9f show growth phase pressure (only data points with beta >1 and corresponding AE max > 300 nT) (red lines indicate linear or polynomial fitting) in the region of $-10 \le X \le -15$ R_E and $|Y| \le 5$ R_E as a function of P_{SW}, the time duration from the onset of the previous substorm, the observed monthly averaged sunspot number, 30-min average (over the 30 min period prior to each pressure data point) of CPCP, 30 min average of AE, and the time before the substorm onset. The sunspot number is considered since our dataset spans over one solar cycle. The pressure is seen to increase with increasing P_{SW}, CPCP and AE in general as indicated by the fitting curves. The correlation between pressure and the time since a previous onset is weak as shown by the red fitting curve, whereas the upper bound of pressure is higher when the time since a previous substorm is shorter, that is, when the growth phase of this substorm starts in earlier recovery phase of the previous substorm, indicating the higher pressure is partially due to the energy that was loaded during the growth phase of the previous substorm but was not dissipated during that substorm. This correlation with the pervious substorm is reflected on the correlation with AE shown in Figure 2.9e. Since AE reaches a peak during the expansion phase then decreases in the recovery phase, a growth phase that starts within the recovery phase of the previous substorm corresponds to larger AE than does a growth phase well separated from the previous substorm. Thus, the AE values during a growth phase can be used as a proxy to indicate the energy that was loaded during the previous substorm and still remains in the plasma sheet. The pressure increases first and then decreases with sunspot number, showing a peak at sunspot number of ~ 80. As shown in Figure 2.10 that the solar wind velocity peaks during the declining phase of the solar cycle, when the sunspot number is ~60-80 (marked by the two red vertical lines), while solar wind number density reaches its lowest. The fast speed solar wind combining with low solar wind density produces the hot and tenuous plasma in the plasma sheet, which result in large plasma pressure. On the other hand, the pressure shows little correlation with the time duration before the substorm onset statistically because of the very different temporal variations of CPCP, AE, and P_{SW} seen in each substorm. Figures 2.9g to 2.9i show the AE max as a function of growth phase pressure and 30 min averages of CPCP and AE (red lines indicate linear or polynomial fitting). The AE max increases as plasma pressure or CPCP or AE increases, indicating that higher plasma sheet pressure, in response to larger solar wind energy input and/or larger energy remaining from the previous substorm, results in a more intense substorm.

As shown in Figure 2.9, the plasma sheet pressure is highly correlated with CPCP and AE. However, instantaneous CPCP or AE value cannot uniquely determine the state of energy input from the solar wind or the energy remained from the previous substorm. First of all, while convection strength does determine the rate of energy loading, it does not uniquely specify the state of energy loading, which depends on the time history. For example, the plasma sheet pressure might keep increasing even though CPCP is enhanced but remains constant. In addition, the CPCP or AE temporal variation during the substorm growth phase can be very different case by case, which can readily be seen in the many events we have examined. The CPCP or AE may increase or decrease gradually, have almost no change, or fluctuate a lot during the substorm growth phase. To consider the effect of history, we defined two energy loading parameters that are the time integrals of CPCP and AE, that is, PCP energy loading ($\int_{t1}^{t} PCP{\cdot}dt$) and AE energy loading ($\int_{t1}^{t} AE{\cdot}dt$), where the integral is over time from a chosen time t_1 before onset to the time

t. We have tested t_1 = 30, 60 and 90 min and found that the energy loading parameters with t_1 = 60 min are best correlated with the AE max. We also created a new energy loading parameter that combines the two loadings, that is, PCPAE energy loading = PCP loading + 4/25 ·AE loading. The weighting factor 4/25 gives the range of AE loading to be the same as range as the PCP loading range, and thus gives the AE loading an equal weight to the PCP loading. We tested different weighting factors and found that 4/25 has the highest correlations with AE max. The units of PCPAE energy loading are kV·min.

Figure 2.11 shows the correlations between the AE max and the three energy loading parameters during different stages of a solar cycle (1995 and 2010 are near a solar minimum and 2001 is near a solar maximum). It can be seen that the linear correlation coefficients are always the highest for the PCPAE loading. Thus, in the following analysis, we use the PCPAE loading parameter as the energy loading factor, instead of using PCP and AE as separate loading parameters. Figure 2.12 shows the temporal variations of the PCPAE energy loading during the substorm growth phase for three different AE max ranges. The PCPAE loading increases as the growth phase proceeds. For larger AE max, the PCPAE loading at the beginning of the growth phase is higher, which is likely due to higher AE values resulting from the previous substorm. The PCPAE loading also increases more quickly and reaches a higher value before the onset for more intense substorms.

2.2.2.2 Regression analysis and empirical pressure model

To quantitatively understand how the three primary factors, PCPAE loading, P_{SW}, and the sunspot number control the plasma sheet pressure during substorm growth phase, we conduct regression analysis using a Support Vector Regression Machine (SVRM) technique. This allows us to construct a SVRM empirical pressure model to evaluate the plasma pressure changes in response to each of these factors. In the analysis, we consider the plasma pressure data locations in X and Y, and use Br to indicate the relative Z distance to the equatorial plane (Br = 0).

SVRM is regression analysis using the Support Vector Machine (SVM) [*Drucker et al.,* 1997]. SVM is a supervised machine-learning technique in the framework of statistical learning theory [*Vapnik and Lerner*, 1963; *Noble*, 2006]. The SVRM maps multi-dimensional data (in this study, X, Y, Br, P_{SW}, PCPAE loading, and sunspot number) into a high-dimensional feature space (plasma pressure in this study), via nonlinear mapping through a selected kernel function, and performs a linear regression in this space. SVRM is non-parametric, thus requiring no analytical forms for the model. In contrast, previous plasma sheet pressure models, such as *Spence and Kivelson* [1993], *Tsyganenko and Mukai* [2003], and *Wang et al.* [2013], are parametric and analytical forms are specified. These parametric models require large database to achieve reasonable accuracy, and the forms may not be sufficiently flexible to well represent the observed distributions of plasma sheet pressure. Compared with parametric analysis, the SVRM technique is expected to be more efficient since it can incorporate many types of high-dimensional, multi-scale input data, which is always problematic for parametric analysis. SVRM also avoids the traps of local minima, and it theoretically does not suffer "the curse of dimensionality", which is a problem for parametric models when available data become sparse as the dimensionality increases.

There have been some studies in space physics successfully using SVM for forecasting. For example, SVRM has been successfully applied by *Y. Wang et al.* [2013] in modeling the 3-D magnetopause shape. They used a magnetopause-crossing database from multiple satellite observations to construct a new 3-D magnetopause model with the shape of the magnetopause, including its cusps and complex dependence on various control parameters, automatically determined by using SVRM, and they achieved very high prediction accuracy compared with observed data, which is not guaranteed by the previous magnetopause models. *Gavrishchaka, and Ganguli* [2001] used SVM to predict AE index from solar wind and IMF data and they concluded that their AE model gives a reliable prediction of large-amplitude substorm events. An empirical model for predicting low-latitude storm-time ionospheric foF2 using the SVM technique was developed by *Ban et al.* [2010], and their results indicated that the model can capture the low-latitude ionospheric disturbances most of the time. *Liu et al.* [2011] predicted the hourly average solar wind velocity with SVM and found that the predicted velocity values are very close to the observations for most of the time, indicating that their SVM prediction is accurate and reliable. Furthermore, *Huang et al.* [2009] used SVM to forecast daily F10.7 index and found that their model can perform well with only a small fitting database.

In my thesis research, LibSVM (version 3.17), a freely available and widely used implementation of SVRM is used, which handles all the complex technical details for this technique [*Chang and Lin*, 2001]. Details of how to use LibSVM can be found in *Y. Wang et al.* [2013]. In LibSVM, different SVM types and kernel functions are supported. We chose the commonly used epsilon-SVR and Radial Basis Function (RBF), $\exp(-\gamma|u-v|^2)$, where *u* is data, *v* is prediction, and γ controls how far a discrete data point is effective in constructing a continuous fitted parameter function for fitting in the high-dimensional feature space. This combination is very flexible and robust in handling many problems and is free from many difficulties of some other combinations. The RBF is used first to map our data to high dimensional feature space. Then in this feature space, SVR is used to obtain a smooth model surface.

2.2.2.3 Constructing SVRM empirical plasma pressure model

We randomly selected 100,000 data points (out of 2,500,000) within the plasma sheet (defined here by requiring $Br/B_Z \leq 1$) for SVRM fitting. Adding more model fitting data will consume more computing resources since the complexity of SVRM fitting is quadratic of the number of fitting data. We chose 100,000 data points to do model fitting to balance the computational burden and model accuracy. The distributions of the selected data points are shown in Figure 2.13a, with more data points located in the transition region where the magnetic field configuration changes from dipole-like to tail-like configuration around r ~7 to 12 R_E than at other locations. As shown in Figure 2.13b, the majority of the data points correspond to Br between 0 and 30 nT, P_{SW} between 0 and 6 nPa, PCPAE loading between 0 and 10,000 kV·min, and the sunspot number between 0 and 140. Therefore, SVRM predictions outside these ranges may not be as reliable as those within the ranges.

There are three free parameters (α, C, γ) in the model fitting process. α, introduced through SVR, is the distance from the fitted surface within which no fitting error is counted for a data point. Here we set α = 0, thereby requiring the fitted surfaces to go through the center of the data distributions as much as possible; The error factor, C, introduced through SVR, is defined for data points falling outside of distance α. γ is the parameter in RBF. Using different C and γ, SVRM gives different model pressure distributions. A larger γ leads to a smaller data effective range and model reflects more local observations. And a larger C leads to tighter fitting of the data points, which can adversely affect model smoothness. The choices for C and γ are critical to guarantee the regression effectiveness. To reduce the computation complexity, we first performed a coarse grid search (γ is from 0.001 to 10 and C is from 0.01 to 300) to identify a region that includes the optimal combination of C and γ. We then conducted a fine grid search with a unit grid of C from 1 to 40 and γ from 1 to 4. We found that using $\gamma = 1$ and $C = 1$ yields the best regression accuracy, as is shown later in the comparisons between model pressures and observations. Figure 2.14 shows three examples of the model equatorial plasma pressure and the pressure gradients along the X and Y directions for ($\gamma = 1$, $C = 1$), ($\gamma = 1$, $C = 35$), and ($\gamma = 3$, $C = 35$) with Br = 0, $P_{SW} = 2$ nPa, PCPAE loading = 4000 kV·min, and sunspot number = 50. Clearly, there are more bumpy pressure and pressure gradient structures with a larger γ or C, which reflects more the local small-scale variations, though the difference between different C is not as strong as γ. Therefore, we chose $\gamma = 1$ and $C = 1$ for our pressure model for its accuracy and for giving smooth large-scale structures.

To provide error estimation of the pressure predictions from the model ($\gamma = 1$ and $C = 1$), we constructed a SVRM error model using the same control parameters (X, Y, Br, P_{SW}, PCPAE loading, and sunspot number). It enables us to obtain model errors appropriate to different locations and control parameters. Instead of fitting the pressure, we fitted the normalized deviations ($|P_{obs}-P_m|/P_{obs}$) between our model pressures (P_m) and the 10,000 observation data points (P_{obs}) used in the pressure model fitting. We assumed $\alpha = 0$, and searched a unit grid of γ from 1 to 4 and C from 1 to 40. Again, the ending search values of γ and C were determined after trials. We checked model results for the same set of standard control parameters of Br = 0, $P_{SW} = 2$ nPa, PCPAE loading = 4000 KV·min, and sunspot number = 50, and chose $\gamma = 1$ and $C = 1$ for the final error model, which gives error model accuracy and smoothness and as for the pressure model.

2.2.2.4 Model validation

After we established the pressure model and error model, we further verify the model performance by comparing observations selected from the database of ~2,800,000 data points with model predictions with inputs from the loading, P_{SW}, and the sunspot number corresponding to each observation point. Figure 2.15a shows the comparisons of model pressures with the observed ones at different locations near the equatorial plane. Here we selected the data to be close to the equatorial plane by requiring $Br/B_Z \leq 1$. As we can see, the predicted pressures match well with the observed ones in general. Figure 2.15b shows the deviations between the model and observed pressure as a function of Br, P_{SW}, PCPAE loading, and sunspot number of the 2,800,000 data points. The black lines show the median values of pressure deviations, which are less than 5% for all situations, and the upper quartiles are mostly less than 20%. Meanwhile, the pressure deviations show almost no change with Br, P_{SW}, PCPAE loading, and sunspot number, except for the larger deviations when the sunspot number is larger than ~135.

We further verified whether the predicted pressure structures could provide reliable pressure gradients by comparing them with the observed pressure gradients computed from simultaneous measurements from two THEMIS probes. We searched an aurora substorm list [*Nishimura et al.*, 2011] and found about 200 cases having either a good radial or azimuthal conjunction between two THEMIS probes so that we are able to compute directly pressure gradients. Figure 2.16 shows the comparisons of pressure and the magnitudes of pressure gradients in the X direction (requiring the probe separation $|dY| < 1\ R_E$ and $|dX|/|dY| > 2$) and Y direction (requiring the probe separation $|dX| < 1\ R_E$ and $|dY|/|dX| > 2$) between the THEMIS observations and predictions. We selected data points within the plasma sheet by requiring data having plasma beta > 0.1 for $r < 7\ R_E$ and beta > 0.6 for $r = 7$ to $10\ R_E$ and beta >1 for $r > 10\ R_E$. In general, the predicted pressures are highly correlated with the observations and the majority of the predicted pressure gradients match well the observations. The above two validations indicate that our SVRM model can reliably allow us to evaluate quantitatively the individual and combined effects from energy loading, P_{SW}, and the sunspot number on the large-scale plasma sheet distributions during the substorm growth phase.

2.2.2.5 Effect of P_{SW}, energy Loading, and sun spot number

Figure 2.17 shows how the pressures and errors predicted by the pressure model and error model change as P_{SW}, PCPAE loading or sunspot number increases within its reliable ranges while the other two parameters are kept constant. Results are shown at different X distances along midnight and along Y = 4 R_E. It can be seen in the left column that under a fixed energy loading the model pressure increases linearly as P_{SW} increases at all locations, and the increase is stronger when the corresponding energy loading is lower. These dependences are likely a result of the balance between P_{SW} and magnetosphere pressure (magnetic pressure in the lobes and plasma pressure on the equatorial plane). For example, when equatorial plasma pressure becomes higher due to higher energy loading, the resulting stronger lobe magnetic pressure makes it more difficult for Psw to compress the magnetosphere, as indicated by the studies of *Petrinec and Russell*, [1993] and *Shue et al.,* [1997] showing that the nightside magnetopause size under the same P_{SW} is larger when IMF Bz is more negative.

As shown in the middle column, the model pressure under a fixed P_{SW} increases non-linearly as energy loading increases. The pressure increases first with increasing energy loading then becomes relatively constant after loading reaches ~8000-10000 kV·min. The pressure increase with energy loading is relatively larger when the corresponding P_{SW} is lower, which is also likely the result of the balance between the Psw and magnetosphere pressure discussed above. In addition, the pressure increase with increasing energy loading is larger near midnight than away from midnight. This may be the result of two factors. The PCPAE energy loading includes both effects from convection (PCP loading) and the previous substorm (AE loading).

The pressure change due to particle energization under earthward convection strongly depends on the distributions of Bz. Typically, across the tail, the magnitude of the equatorial Bz is the smallest near midnight and |dBz/dX| is the largest along the Y = 0. Thus earthward electric drift will be larger, and particles will experience a larger Bz change along Y = 0 than away from midnight. This should result in larger adiabatic energization and pressure increase at midnight. The effect of the previous substorm represented by AE loading is also not uniform across the tail. As shown in *Wing et al*., [2007], the pressure increase after a substorm onset is larger near midnight than away from midnight, thus contributing to higher pressure near midnight for the growth phase of the following substorm.

As shown in the right column, the model pressure under a fixed energy loading increases nonlinearly as sunspot number increases. The model pressure at smaller r increases first then decreases, showing a peak at around sunspot number of ~80, which is consistent with the observations shown in Figure 2.9c. The pressure shows little change under smaller sunspot number farther from the Earth, while it decreases then increases at higher sunspot numbers, showing a dip around sunspot number of ~110. The sunspot number has been shown to correlate with different solar wind structures and polar-cap conductance [*Gonzalez et al.,* 1999; *Ohtani et al.,* 2014]. Previous studies [e.g., *Borovsky and Denton*, 2006] also showed that the high-speed solar wind is more likely generated at the declining phase of a solar cycle when the sunspot number has decreased to near half of the peak value at solar maximum. This correlation is seen in our dataset. For a given P_{SW} and energy loading, the solar wind velocity maximizes at sunspot number of ~60-80 while the solar wind number density reaches the lowest. Since there are strong and positive correlations between solar wind velocity and the plasma sheet temperature and between the solar wind number density and plasma sheet density [*Borovsky et al*., 1997], one would expect statistically that the plasma sheet is hotter and more tenuous when the sunspot number is near 60-80 than under other sun sport numbers. Also it has been shown that the plasma sheet pressure is generally higher for hot-tenuous plasma sheet than cold-dense plasma sheet [*Wang et al.,* 2009; 2010], the plasma sheet pressure is thus likely to be the highest when sunspot number is ~60-80. In addition, simulations from *Gkioulidou et al.* [2008] have shown that under the same CPCP driving, the shielding of convection electric field is less effective when the plasma sheet is hotter and more tenuous. As a result, the inner edge of the plasma sheet is further earthward and the plasma sheet pressure is higher for a hotter and more tenuous plasma sheet (see Figure 5 in *Gkioulidou et al.* [2008]). These previous studies thus provide a reasonable explanation for the dependence on the sunspot number and the larger dependences seen at smaller |X|.

Figures 2.18a to 2.18c show the equatorial pressure distributions for four different loadings (100, 2000, 4000, and 8000 kV·min) when P_{SW} = 2 or 5 nPa and sunspot number = 10 or 80 (80 is approximately the median sunspot number as shown in Figure 2.13a). As shown in Figure 2.12, these four loading values are typically seen at different growth phase stages of a moderate substorm with 100 at the beginning, 2000, 4000 at the middle, and 8000 at the end of the growth phase. Their midnight profiles are shown in Figure 2.18d. The overall predicted pressures are higher when under higher energy loading or P_{SW}. On the other hand, under the same loading and P_{SW}, pressures at median sunspot number are found to be higher in the near Earth region but lower in the tail compared to those under lower sunspot number (also compared to those under higher sunspot number, not shown). Figure 2.18e shows the azimuthal profiles at r = 10 R_E. The pressures are more dawn-dusk asymmetric with higher pressure at the pre-midnight

MLTs when P_{SW} is higher or the sunspot number is closer to the median values. These asymmetries become weaker when loading is higher.

2.2.2.6 A substorm event study

The spatial structure of the growth phase pressure and its quantitative correlations with different factors predicted by our empirical model can be used to understand the pressure changes observed by spacecraft during substorm events. Here we conduct an event study for a substorm on Dec. 31, 2008 (the onset defined by the AL drop occurred at ~05:38 UT while that defined by aurora occurred at ~05:32 UT). This event is chosen for having a large and monotonic change in P_{SW}. Figure 2.19a shows the variations of P_{SW}, CPCP, AE and PCPAE loading. During the growth phase, P_{SW} increased from 3.5 to 6 nPa in the first 5 min, then decreased gradually from ~6 to 2.6 nPa with some small fluctuations. Meanwhile, CPCP decreased sharply during the first 3 min, then gradually increased from ~35 to 90 kV and remained around 90 keV after ~05:15 UT. AE was high at the beginning because of the previous substorm. It decreased to 100 nT in about 20 min and then increased back to 200 nT prior to the onset (the vertical dashed line in Figure 2.19a marks the onset time), and AE max after the onset is ~480 nT. The PCPAE loading increased from ~100 to 6000 kV·min, corresponding to a typical moderate substorm as shown in Figure 2.12.

Figure 2.19b shows the trajectories of TH-C and TH-D in the X-Y plane in GSM coordinates during the growth phase. TH-D was at r ~6 R_E while TH-C was at r ~12 R_E and both were moving eastward and farther away from midnight. As shown in Figures 2.19c and 2.19d, they remained near the plasma sheet for most of the growth phase as indicated by the comparable magnitudes between the plasma pressures (black line) and total pressures (blue line), except for TH-D for two very brief durations at the beginning and near the end of the growth phase. We then predicted the evolution of pressures with the temporal profiles of the control parameters (X_{GSM}, Y_{GSM}, Br, P_{SW}, PCPAE loading, and the monthly averaged sunspot number = 0.8). To illuminate the effect of P_{SW} changes, we also evaluated the pressure change using constant P_{SW} = 2.6 nPa (the lowest P_{SW} during the growth phase). The model results and corresponding observations from TH-D and TH-C during the substorm growth phase are shown in Figures 2.19c and 2.19d, respectively. The predicted total pressures with time-dependent P_{SW} and constant P_{SW} are indicated by the red and green lines, respectively. It can be seen that the total pressure (blue line) observed by TH-D gradually decreased from ~1.8 to 1 nPa during the substorm growth phase. The predicted pressure with time-dependent P_{SW} (red line) agrees well in general with the observed pressure (blue line) in both magnitudes and its decreasing trend, except the two very short periods when TH-D went suddenly farther away from the current sheet at ~4:35 and ~05:20 UT. Br during these two periods was > 40 nT and exceeded the reliable Br range (< 30 nT) for the pressure model, thus causing the discrepancy between the predicted and observed pressures. In comparison, the predicted pressure at TH-D with constant P_{SW} (green line) still shows a slight decreasing trend despite that globally the plasma pressure is increasing under increasing loading. This is because TH-D was moving farther away from midnight to a location where, as shown in Figure 2.17, the pressure is relatively lower and the pressure increase in response to increasing loading is also smaller. The local temporal pressure increase is smaller than the spatial pressure decrease along TH-D trajectory, resulting in the slight pressure decrease under constant P_{SW}. Thus the observed substantial pressure decrease at TH-D should be mainly due to the decreasing P_{SW}.

On the other hand, at TH-C, both the observed pressure (blue line) and the predicted pressure with time-dependent P_{SW} (red line) show little change as the growth phase proceeds, and the two pressures are in good agreement. The predicted pressure with constant P_{SW} (green line) increases with time, contrary to the prediction at TH-D. This is because the loading effect is stronger at larger *r*, so the local temporal pressure increase exceeds the spatial decrease along the TH-C trajectory. However, this pressure increase due to the energy loading alone is similar to the decrease in response to the decreasing P_{SW} alone, resulting in no substantial pressure changes observed by TH-C. This event study shows that, despite under increasing energy loading, it is not necessary for spacecraft to see a pressure increase during the substorm growth phase, which in fact is quite common, because of the P_{SW} effect as well as the combined temporal and spatial effect along spacecraft trajectory as discussed above.

2.3 The 3D force-balanced magnetic field model

The magnetic field model of *Zaharia* [2008] obtains the magnetic field by solving the single-fluid force balance equation $\nabla P = \mathbf{J} \times \mathbf{B}$ in terms of Euler potentials as $\mathbf{B} = \nabla\alpha \times \nabla\beta$, where P is plasma pressure. In this model P can be either isotropic or anisotropic. The 3D force balance equation can be decoupled into 2 coupled "quasi-2D" equations in the directions parallel to ($\mathbf{B} \times \nabla\alpha$) and ($\mathbf{B} \times \nabla\beta$), respectively as follows:

For isotropic pressure, we obtain,

$$\mathbf{J} \cdot \nabla\alpha = \nabla \cdot [(\nabla\alpha)^2 \nabla\beta - (\nabla\alpha \cdot \nabla\beta)\nabla\alpha] = -\frac{\partial P}{\partial \beta} \tag{5}$$

$$\mathbf{J} \cdot \nabla\beta = \nabla \cdot [(\nabla\beta \cdot \nabla\alpha)\nabla\beta - (\nabla\beta)^2 \nabla\alpha] = -\frac{\partial P}{\partial \alpha} \tag{6}$$

For anisotropic pressure, we obtain,

$$\mathbf{J} \cdot \nabla\alpha = \nabla \cdot [(\nabla\alpha)^2 \nabla\beta - (\nabla\alpha \cdot \nabla\beta)\nabla\alpha] = -\frac{(\mathbf{B} \times \nabla\alpha)}{\sigma B^2} \cdot [\nabla P_\perp + (1-\sigma)\nabla(\frac{B^2}{2})] \tag{7}$$

$$\mathbf{J}\cdot\nabla\beta = \nabla\cdot[(\nabla\beta\cdot\nabla\alpha)\nabla\beta-(\nabla\beta)^2\nabla\alpha] = -\frac{(\mathbf{B}\times\nabla\beta)}{\sigma B^2}\cdot[\nabla P_\perp + (1-\sigma)\nabla(\frac{B^2}{2})] \qquad (8)$$

where $\sigma = 1 + {(P_\perp - P_\parallel)}/{B^2}$.

The constant α and β surfaces are found from solving the equations (5), (6) and (7), (8) numerically, through an alternating iterative process. Both boundary conditions and the inhomogeneous terms on the right hand sides ($\frac{\partial P}{\partial\alpha}$, $\frac{\partial P}{\partial\beta}$ and $\nabla P_\perp$) need to be prescribed.

Here, the pair of Euler potentials (α,β) are chosen as below:

$\alpha' = \alpha + F(\beta)$

$\beta' = \beta$

with $F(\beta)$ to be determined. Here α is defined to be proportional to the poloidal magnetic flux into the Earth, the other potential β is chosen to be equivalent to the azimuthal angle. Since β is equivalent to the azimuthal angle, $F(\beta)$ must be periodic, i.e., $F(\beta+2\pi) = F(\beta)$. The outer boundary condition for α is obtained by tracing empirical magnetic field (e.g., Tsyganenko models) from a prescribed ellipse shape on the equatorial plane. By obtaining $F(\beta)$ through prescribing an outer contour of α, the freedom of choosing the inner contour disappears; a more complete description of this model has been given by *Zaharia* [2008]. The third coordinate, χ, determines the position along the field line and completes the nonorthogonal flux coordinate system (α,β,χ).

The pressure gradients, $\frac{\partial P}{\partial\alpha}$, $\frac{\partial P}{\partial\beta}$ and $\nabla P_\perp$ in (5), (6) and (7), (8) are prescribed by a given pressure spatial profile. The prescribed pressure is kept spatially fixed on the equatorial plane and $P(\alpha,\beta)$ changes at each iteration as α and β change. The iteration process is repeated until the $\alpha = cont.$ and $\beta = const.$ surfaces converge to some tolerance, i.e., when the cumulative difference between α or β between two consecutive iterations decreases to a specified amount (here set to be 0.5%), indicating force balance is achieved.

Table 2.1. Values of fitting parameters b1 to b9 for P_m in equation (1) for different Kp and P_{SW} = 1.5 nPa. R_{corr} is the linear correlation coefficient between P_m and $P_{t,n}$. Err_{RMS} is the normalized RMS error. Err_{Mean} is the normalized mean error.

	Kp = 0 P_{SW} = 1.5	Kp = 1 P_{SW} = 1.5	Kp = 2 P_{SW} = 1.5	Kp = 3 P_{SW} = 1.5	Kp = 4 P_{SW} = 1.5	Kp = 5 P_{SW} = 1.5
b1	–0.8700 ±0.0484	–0.7890 ±0.0565	–0.7888 ±0.0639	–0.6887 ±0.0657	–0.6590 ±0.1408	–0.7311 ±0.1161
b2	213.5363 ±36.7470	123.7894 ±26.1173	73.3651 ±30.6172	99.6864 ±23.4886	60.2186 ±35.6205	137.1203 ±511.8743
b3	0.0322 ±8.4077	–0.1999 ±1.5009	38.6285 ±1.8424	–5.7370 ±1.3305	–27.2739 ±1.4691	166.9548 ±9.4334
b4	99.2106 ±26.9372	73.8102 ±24.8810	99.9520 ±38.5686	15.4089 ±12.4035	29.3575 ±27.6130	231.5938 ±441.4238
b5	–1.2410 ±0.6442	–1.2334 ±0.8023	–2.0651 ±0.3870	–1.2622 ±0.8439	–1.5970 ±0.1755	–1.7076 ±0.8687
b6	7.3564 ±1.5667	11.2507 ±3.0741	69.7594 ±4.7404	15.3724 ±2.8034	39.4608 ±18.0344	53.7482 ±132.4751
b7	–0.5093 ±0.0855	0.0502 ±0.1339	0.2883 ±0.1741	0.0242 ±0.1715	1.3241 ±0.3648	–3.5660 ±1.2279
b8	2.0266 ±0.2359	–0.0773 ±0.3020	9.8675 ±0.3484	0.2230 ±0.3125	–4.0530 ±1.5940	–12.5359 ±8.138
b9	0.0056 ±0.8397	-0.0611 ±0.9703	0.0787 ±0.3038	–0.0864 ±0.4947	–0.0393 ±0.1880	0.0104 ±0.2769
R_{corr}	0.94402	0.93681	0.9255	0.93407	0.87015	0.85403
Err_{RMS}	0.028	0.033	0.032	0.036	0.034	0.034
Err_{Mean}	0.102	0.093	0.112	0.131	0.124	0.236

Table 2.2. Values of fitting parameters b1 to b9 for P_m in equation (1) for different Kp and P_{SW} = 3 nPa. R_{corr} is the linear correlation coefficient between P_m and $P_{t,n}$. Err_{RMS} is the normalized RMS error. Err_{Mean} is the normalized mean error.

	Kp = 0 P_{SW} = 3	Kp = 1 P_{SW} = 3	Kp = 2 P_{SW} = 3	Kp = 3 P_{SW} = 3	Kp = 4 P_{SW} = 3	Kp = 5 P_{SW} = 3
b1	–0.9072 ±0.0518	–0.9024 ±0.0602	–0.8432 ±0.0669	–0.8264 ±0.0811	–0.6909 ±0.3460	–0.7906 ±0.1316
b2	240.0024 ±47.0330	152.1005 ±31.7535	65.3578 ±34.2491	109.6771 ±31.4862	8.1615 ±82.7838	188.7615 ±84.8879
b3	–2.8333 ±4.6522	2.6496 ±2.4269	–63.4070 ±1.1343	–6.4229 ±0.2219	–31.6261 ±0.3266	209.6659 ±3.6729
b4	135.1886 ±39.0879	126.1990 ±37.2681	172.1954 ±52.6818	25.9049 ±15.8282	43.7472 ±74.4886	218.4614 ±167.0783
b5	–0.4292 ±0.1658	–1.2436 ±0.5513	–1.5136 ±0.2516	–1.5213 ±0.5247	–1.7950 ±0.2437	–1.7408 ±0.3538
b6	3.7857 ±1.2484	16.7792 ±7.8300	34.4588 ±2.0089	39.0839 ±21.9181	88.8841 ±33.9701	76.1308 ±24.6083
b7	–0.0752 ±0.0976	–0.0745 ±0.2987	0.6017 ±0.2004	–0.5118 ±0.4317	1.3109 ±1.7290	–2.8949 ±1.5301
b8	0.2609 ±0.5078	–0.1996 ±0.5059	–2.5027 ±0.4430	0.0237 ±0.7579	–11.9868 ±0.8781	–15.0630 ±3.8129
b9	–0.7513 ±0.7740	–0.0718 ±0.7139	0.0093 ±0.5570	–0.0090 ±0.0205	0.0306 ±0.0818	0.1342 ±0.1815
R_{corr}	0.93959	0.93112	0.92439	0.932	0.86305	0.83832
Err_{RMS}	0.029	0.034	0.033	0.037	0.035	0.033
Err_{Mean}	0.096	0.088	0.129	0.136	0.132	0.375

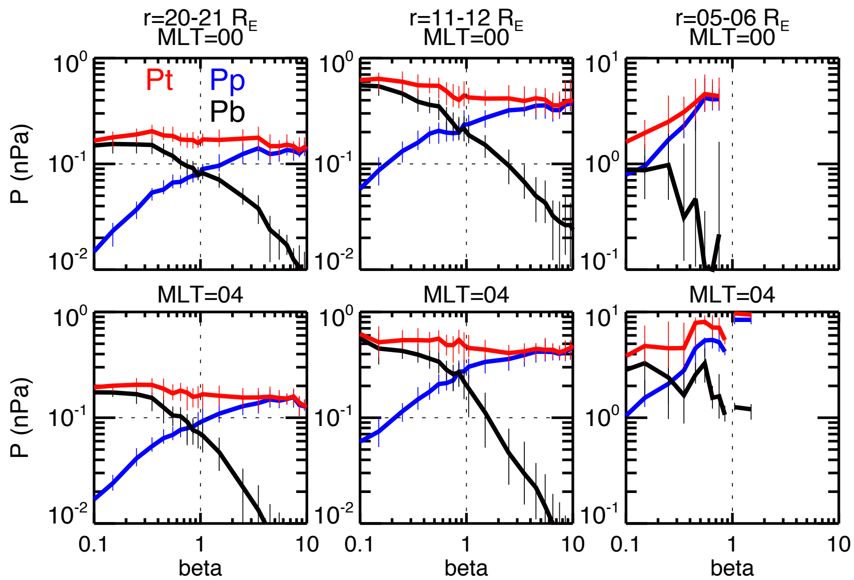

Figure 2.1. Total pressure (the red curves), plasma pressure (the blue curves), and magnetic pressure (the black curves) as a function of plasma beta at different radial distances and MLTs.

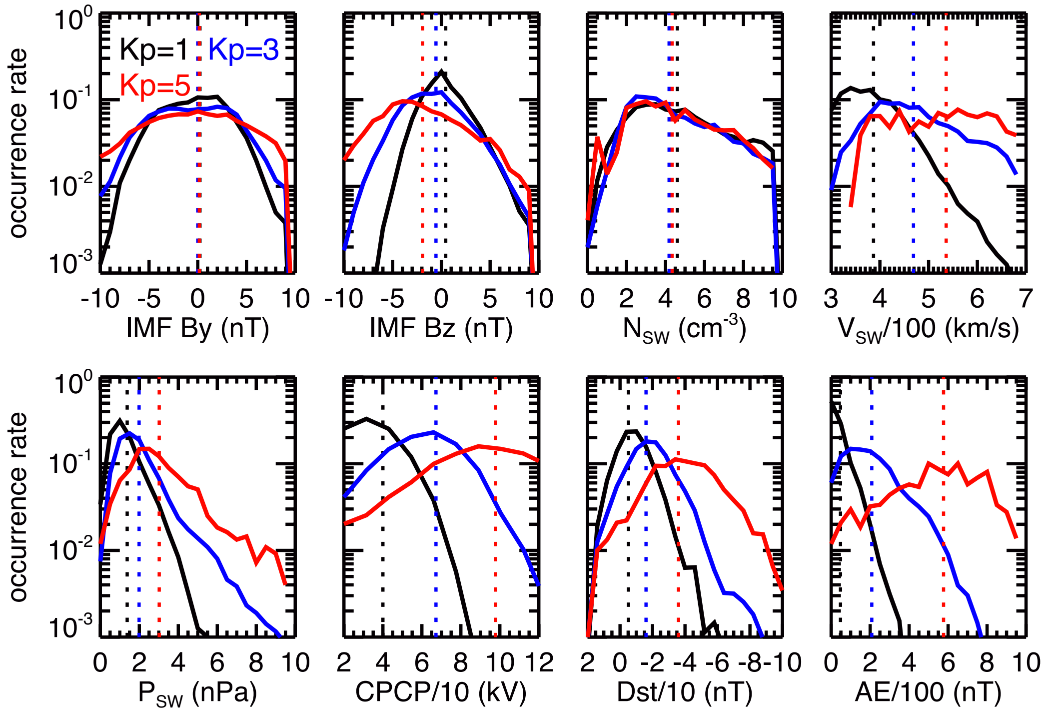

Figure 2.2. Occurrence rate for the IMF B_y, IMF B_z, solar wind density (N_{sw}), solar wind speed (V_{sw}), solar wind dynamic pressure (P_{sw}), the cross polar-cap potential (CPCP), Dst, and AE for Kp = 1 (the black curves), 3 (the blue curves), and 5 (the red curves). The cross polar-cap potential drop is estimated using the Weimer empirical model [*Weimer*, 1995]. The vertical dotted lines indicate median values.

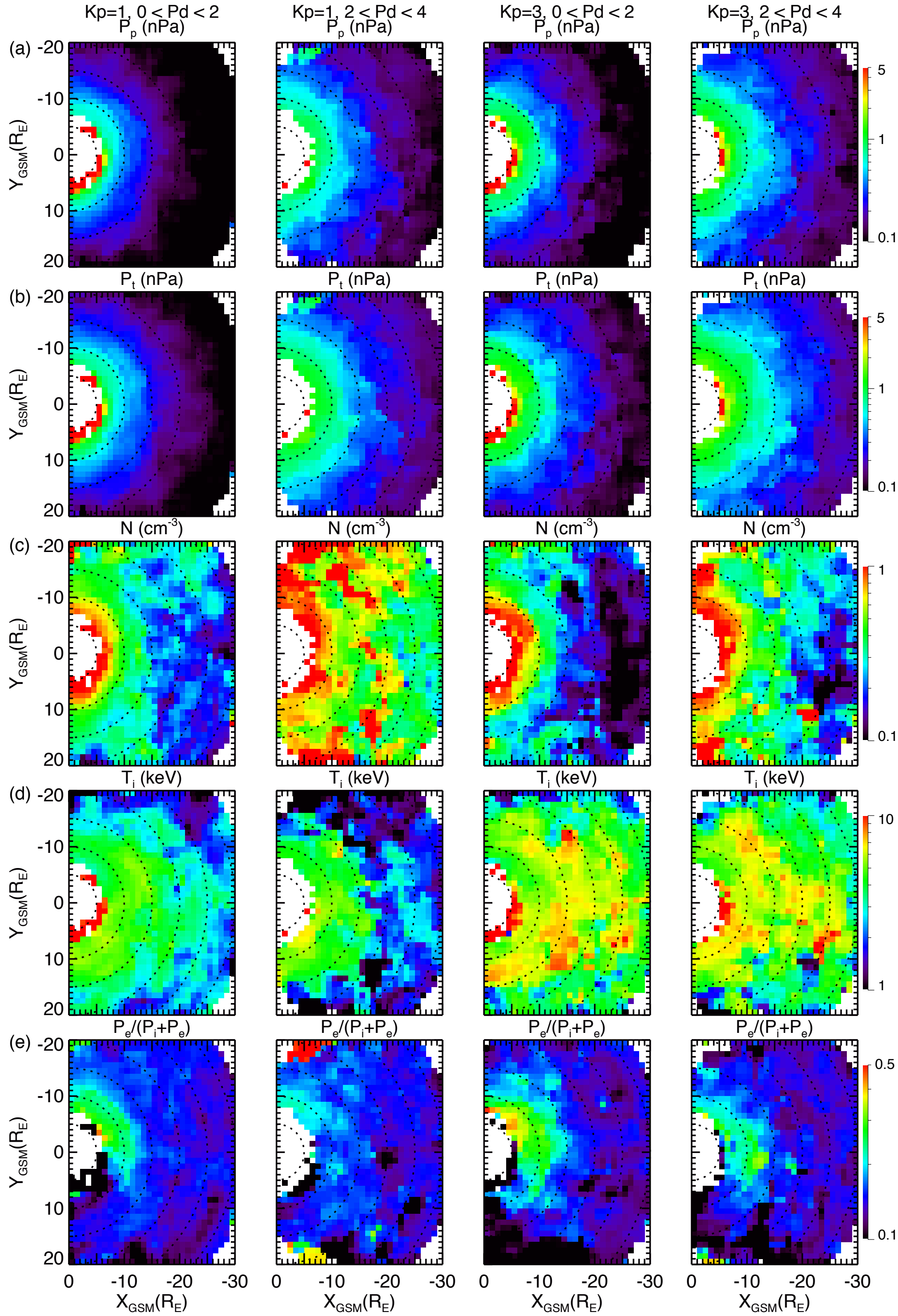
Kp=1, 0 < Pd < 2
Kp=1, 2 < Pd < 4
Kp=3, 0 < Pd < 2
Kp=3, 2 < Pd < 4
P_p (nPa)
P_t (nPa)
N (cm^{-3})
T_i (keV)
$P_e/(P_i+P_e)$
(a)
(b)
(c)
(d)
(e)
$Y_{GSM}(R_E)$
$X_{GSM}(R_E)$

Figure 2.3. Equatorial distributions of (a) plasma pressure, (b) total pressure, (c) number density, (d) ion temperature, and (e) electron to total plasma pressure ratio for four different Kp and P_{SW} ranges.

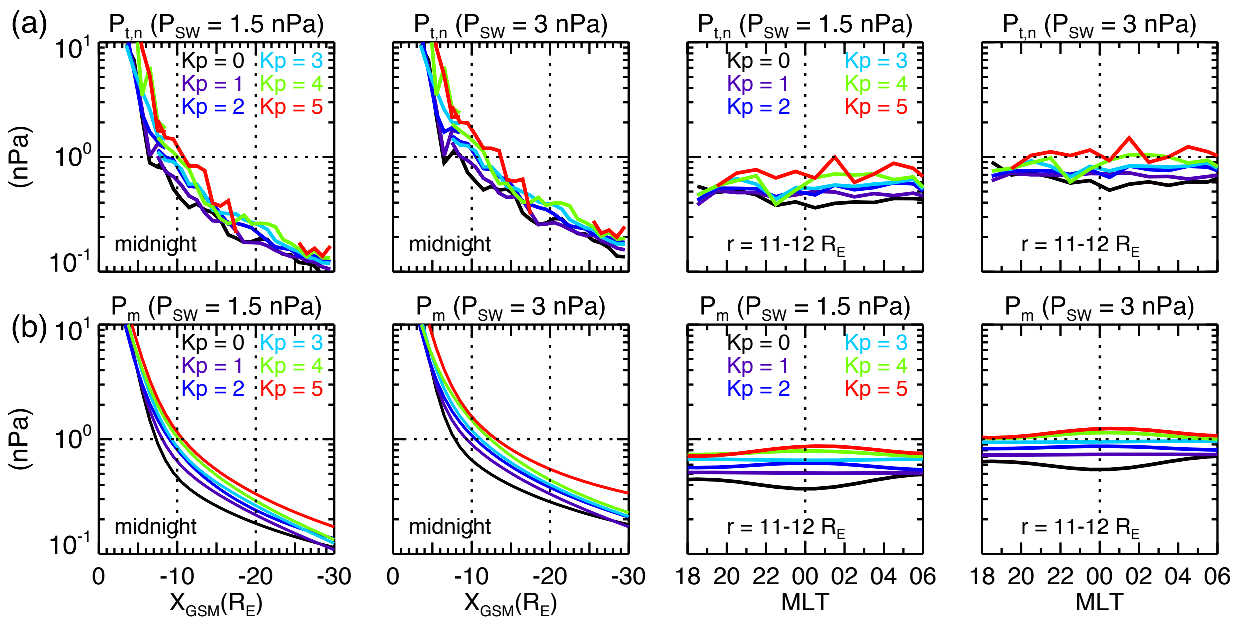

Figure 2.4. The radial profiles at midnight (the left two columns) and azimuthal profiles at *r* = 11-12 R_E (the right two columns) of (a) the observed pressure, $P_{t,n}$ and (b) the model pressure, P_m for P_{SW} = 1.5 and 3 nPa and Kp = 0 to 5.

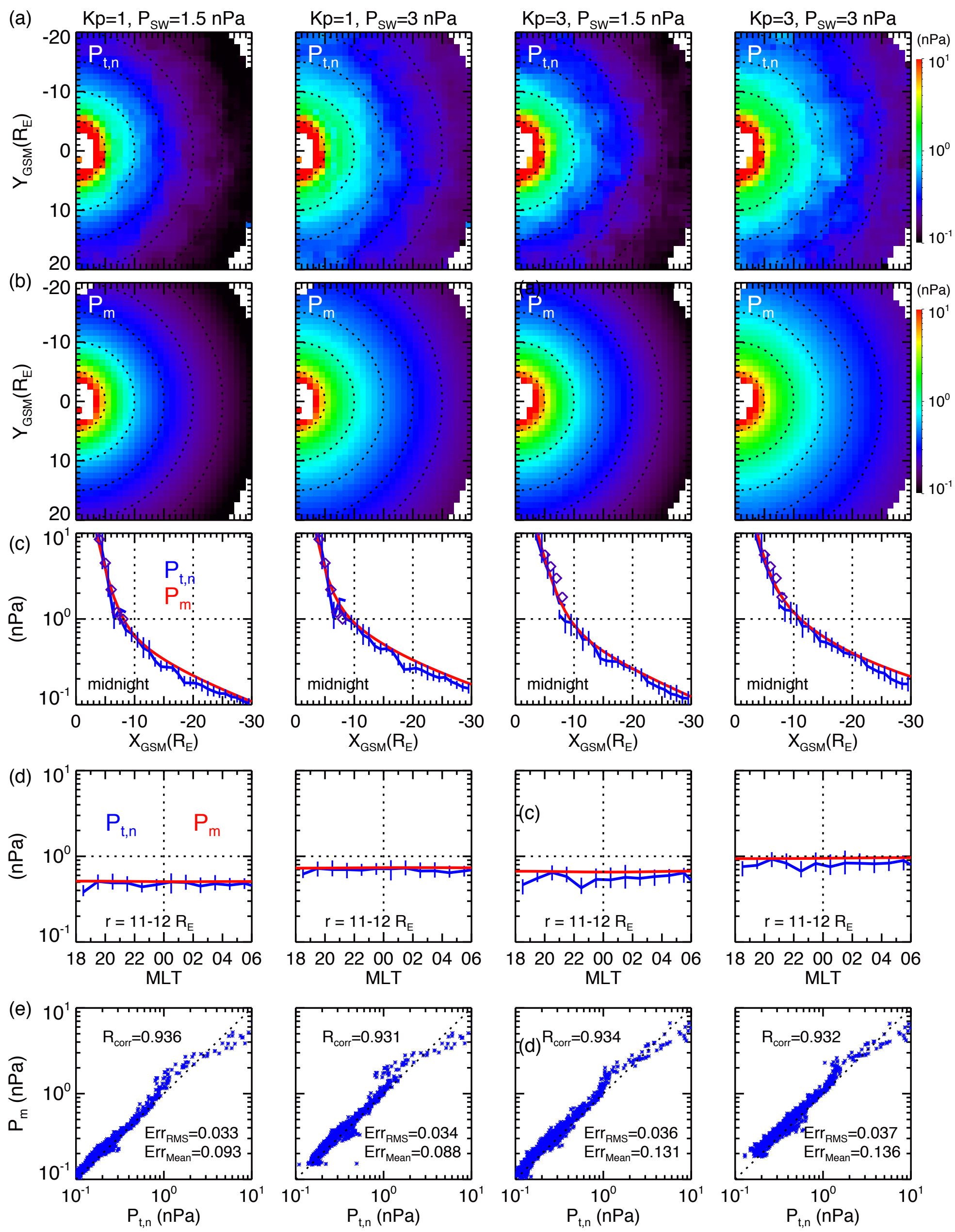

Figure 2.5. Equatorial distributions of (a) the normalized total pressure ($P_{t,n}$) , (b) empirical model pressure (P_m). (c) Comparisons between the normalized pressure (the blue curves) and model pressure (the red curves) in (c) the midnight radial profiles and (d) azimuthal profiles at r = 11-12 R_E for Kp = 1 and 3 and P_{SW} = 1.5 and 3 nPa. The diamonds in (c) are AMPTE/CCE

observations from *Lui et al.* [2003] for Kp < 2 (in the two Kp = 1 plots) and for Kp > 3^+ (in the two Kp = 3 plots).

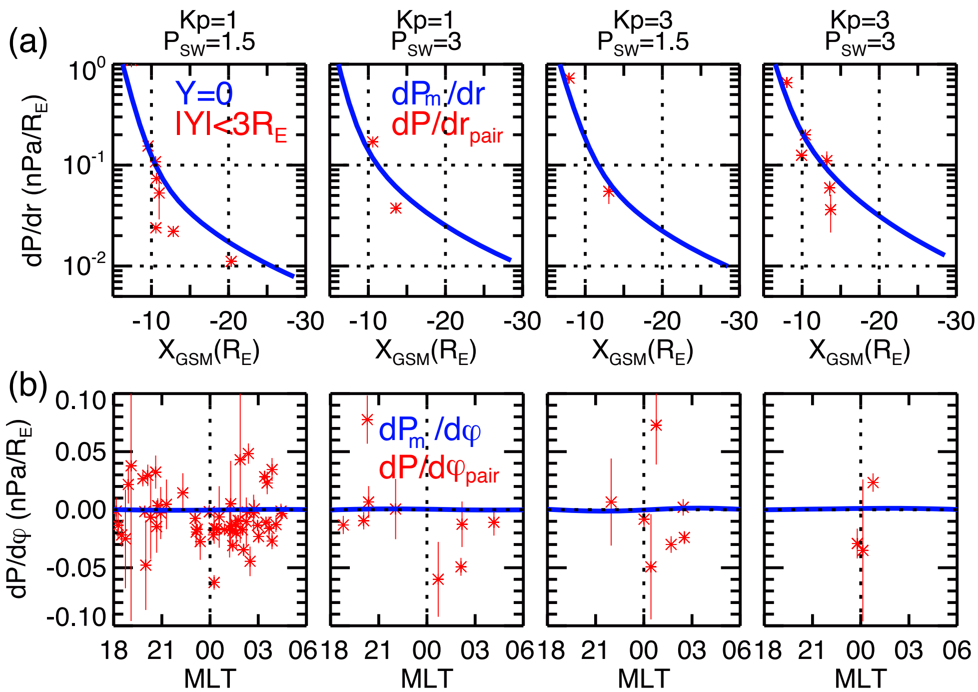

Figure 2.6. (a) The midnight radial profiles of dP/dr and (b) the MLT profiles of dP/dφ at r =11-12 R_E of the model pressure (the blue curves). The red dots are gradients computed from the pressure measurements simultaneously measured by two of the THEMIS spacecraft (with dot indicating the average over a 10 minutes period and vertical line indicating the standard deviation).

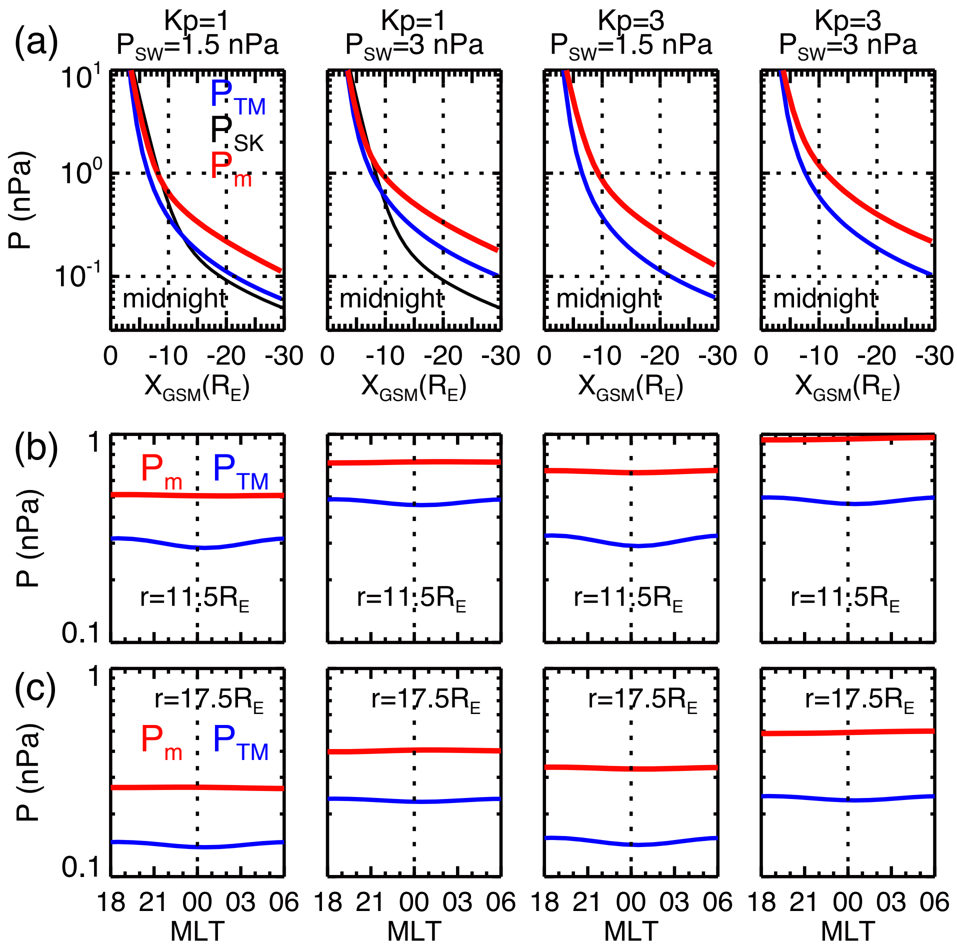

Figure 2.7. (a) Comparisons of the midnight radial profiles of pressure from our model (the red curves), the Tsyganenko and Mukai 2003 model (the blue curves), and Spence and Kivelson 1991 model (the black curves). Comparisons of the MLT profiles between our model and (the black curves). Comparisons of the MLT profiles between our model and Tsyganenko and Mukai 2003 model at (b) r = 11.5 and (c) r = 17.5 R_E.

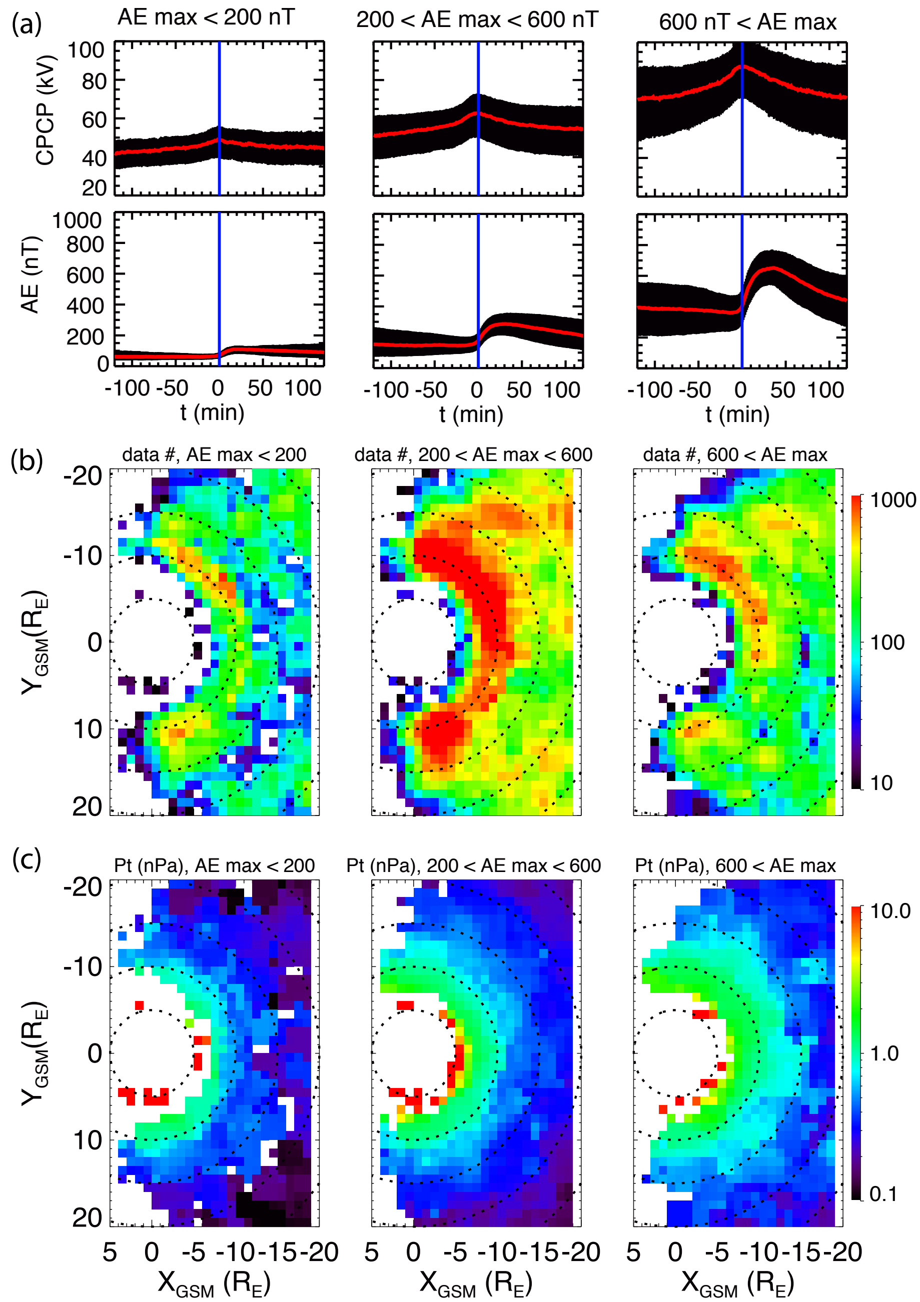

Figure 2.8. (a) The statistical results for three different intensity of substorms (AE max < 200nT; 200 nT< AE max < 600 nT; 600 nT < AE max). (a) CPCP and AE variations in 2 hours prior to and 2 hours after substorm onset. The vertical blue lines make the substorm onset time, the red

line is the median value, and the range is upper and lower quartiles. (b) The data points and (c) plasma sheet pressure distributions during substorm growth phase (0-60 min before onset).

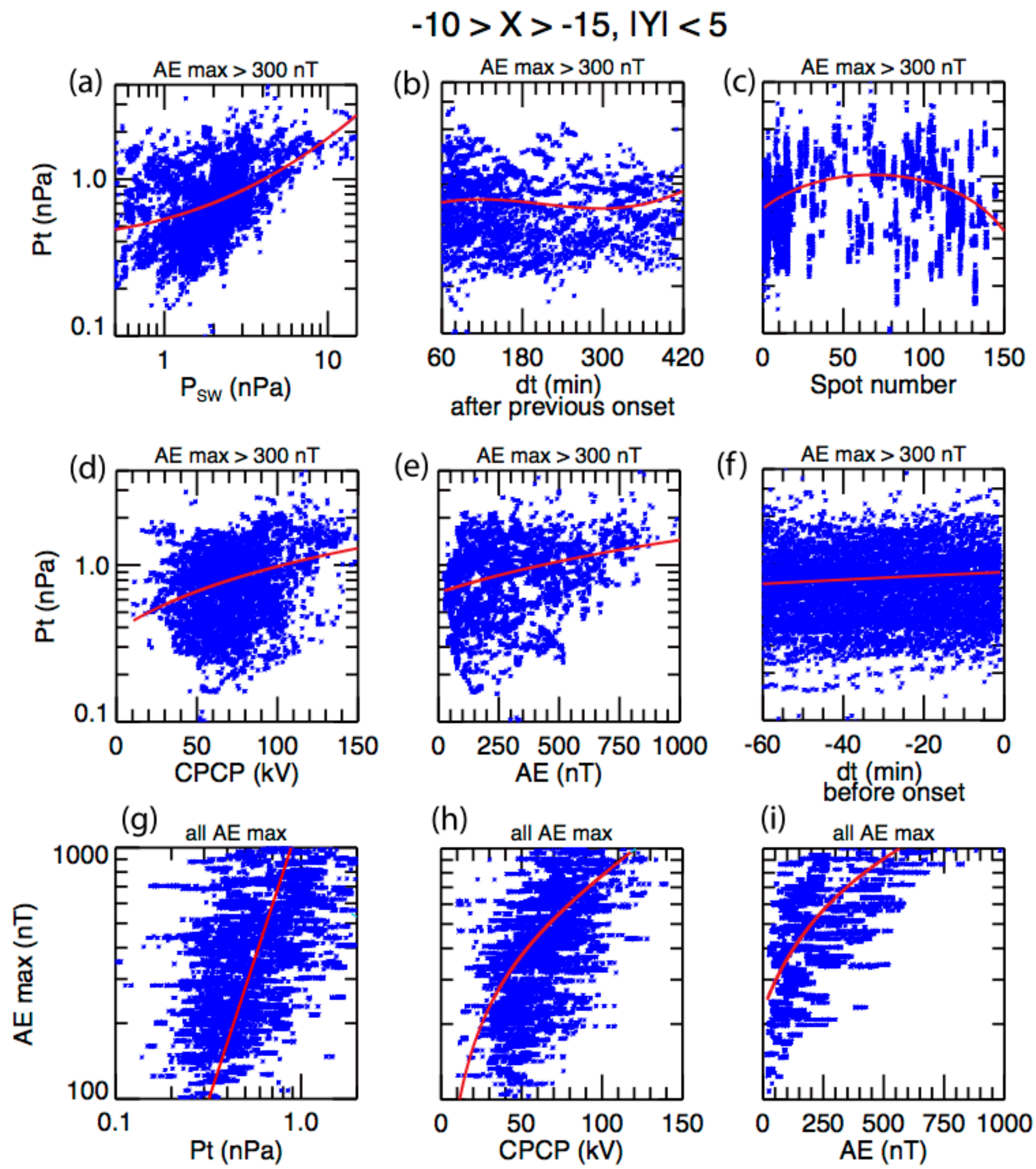

Figure 2.9. a-f: Plasma sheet pressures during substorm growth phase (0-60 min before onset) as functions of P_{SW}, the time duration from previous substorm, the sunspot number, CPCP, AE, and the time duration before the substorm onset at region of -10 < X_{GSM}< -15 R_E and -5 < Y_{GSM}< 5 R_E for substorms that AE max > 300 nT. g-i: the AE max as functions of plasma sheet pressure, CPCP and the AE index during substorm growth phase (0-60 min before onset) at region of -10

< X_{GSM}< -15 R_E and -5 < Y_{GSM}< 5 R_E. The red line in each panel is the linear or polynomial fitting curve.

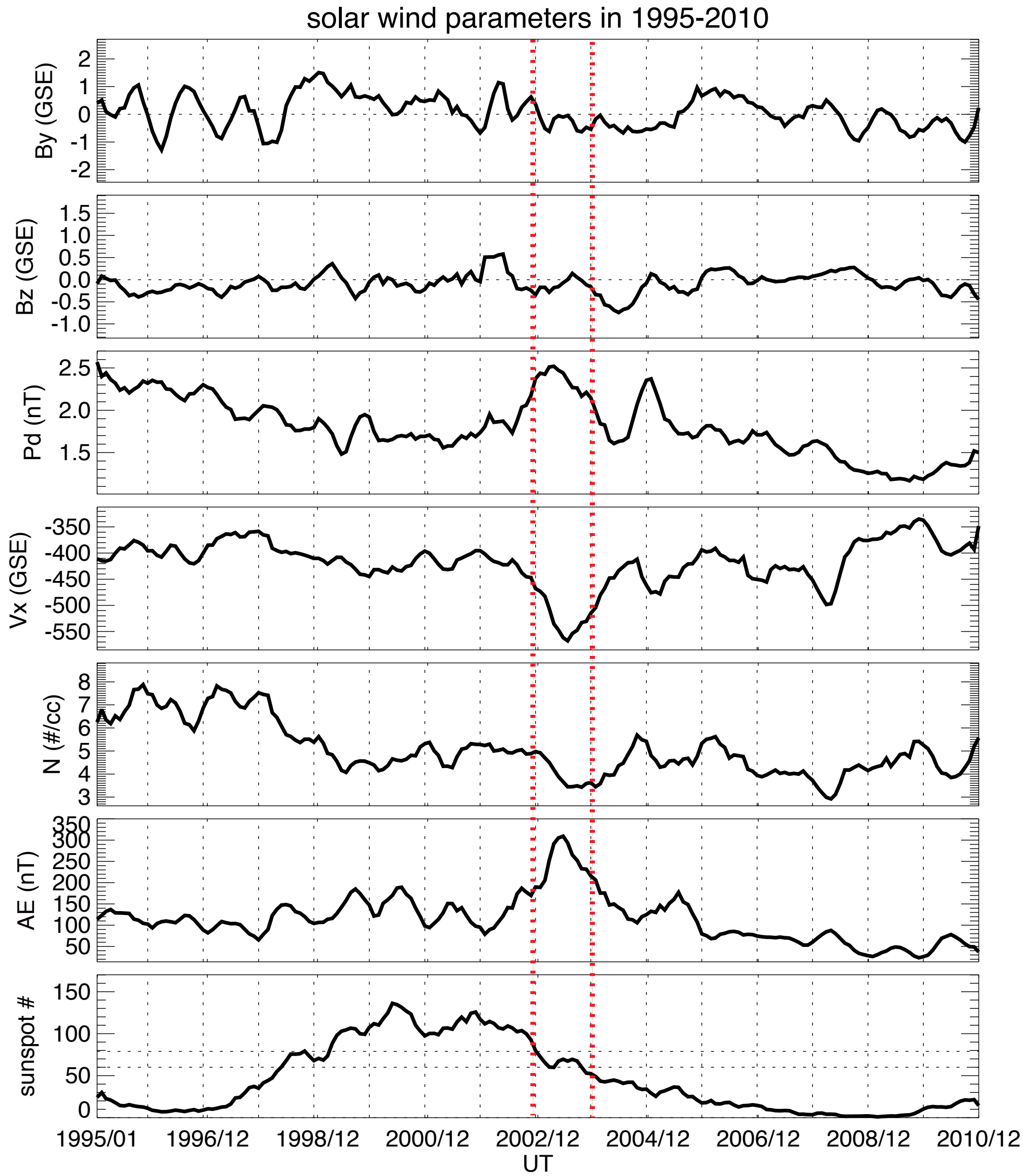

Figure 2.10. The monthly averaged solar wind parameters and AE index during 1995-2010. The plots from top to the bottom panels are IMF B_Y, B_Z in GSE coordinate, solar wind dynamic pressure, solar wind V_X component in GSE coordinate, number density, AE index and sunspot number.

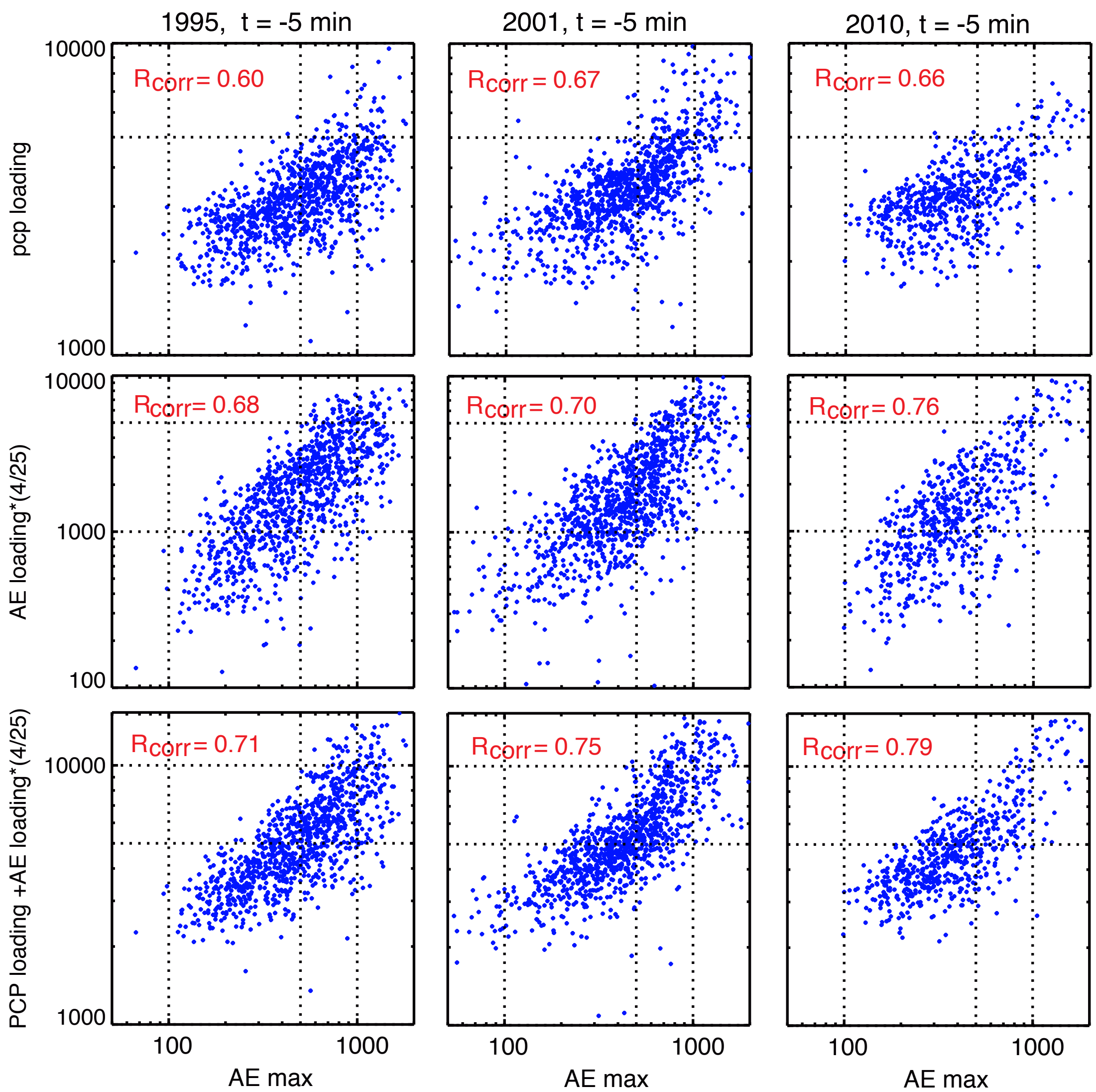

Figure 2.11. Illustration of the linear correlations between the PCP loading, AE loading and PCPAE loading and the AE max at 5 min before substorm onset for year 1995, 2001 and 2010.

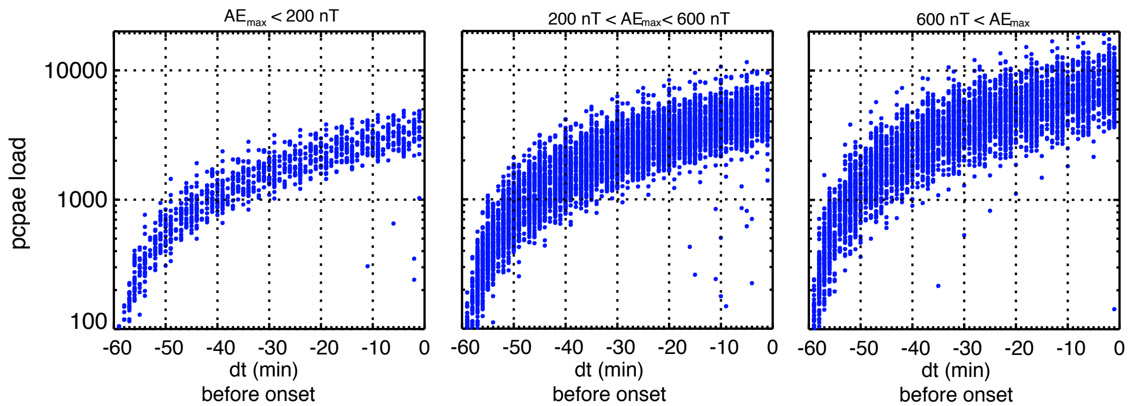

Figure 2.12. PCPAE loading variation during substorm growth phase (60 min substorm growth phase duration) for small substorms (AE max <200 nT), moderate substorms (200 < AE max < 600 nT) and intense substorms (600 nT < AE max)

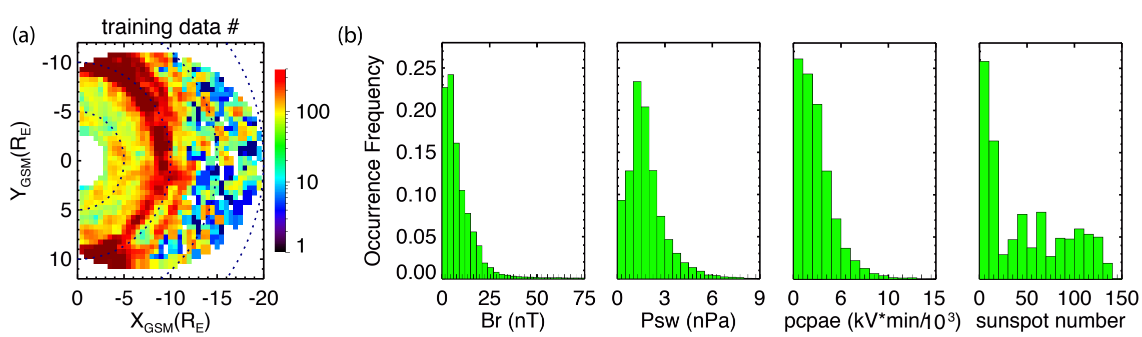

Figure 2.13. (a) Distribution of the pressure fitting data points on the equatorial plane inside the area we interested. (b) Distributions of four control parameters (Br, P_{SW}, PCPAE loading and sunspot numbers) for pressure fitting.

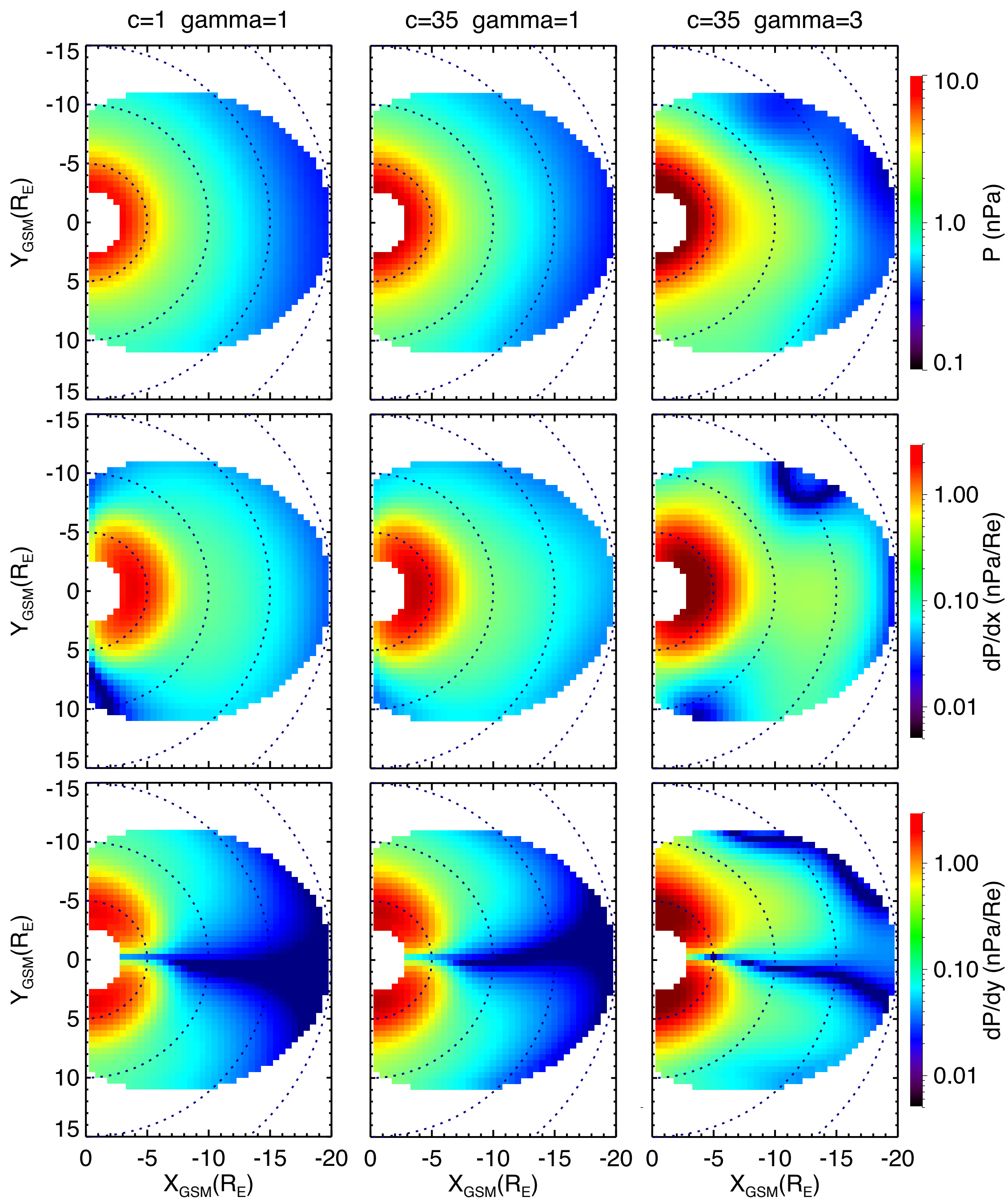

Figure 2.14. Equatorial distributions of plasma pressure, pressure gradient in direction of X_{GSM} and Y_{GSM} coordinate for different c and ϒ choices.

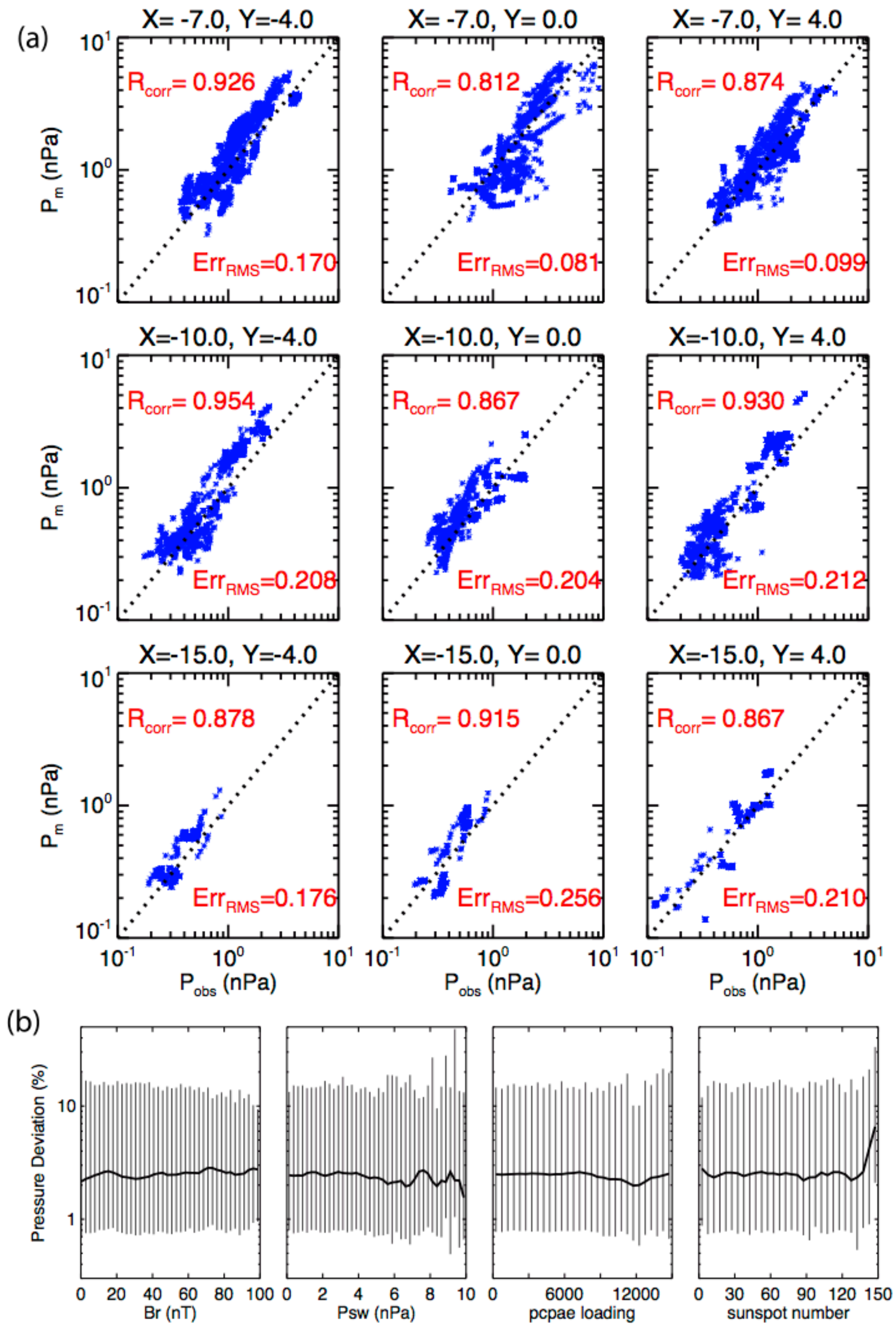

Figure 2.15. (a) The comparison of modeled and observed pressures at different locations. R_{corr} is the linear correlation coefficient between Pm and P_{obs}. Err_{RMS} is the normalized RMS error. (b) The statistical results of normalized deviations between the modeled and observed pressures as

functions of Br, P_{SW}, PCPAE loading and sunspot number. The black solid lines are the median values, and the errors are the lower and upper quartiles.

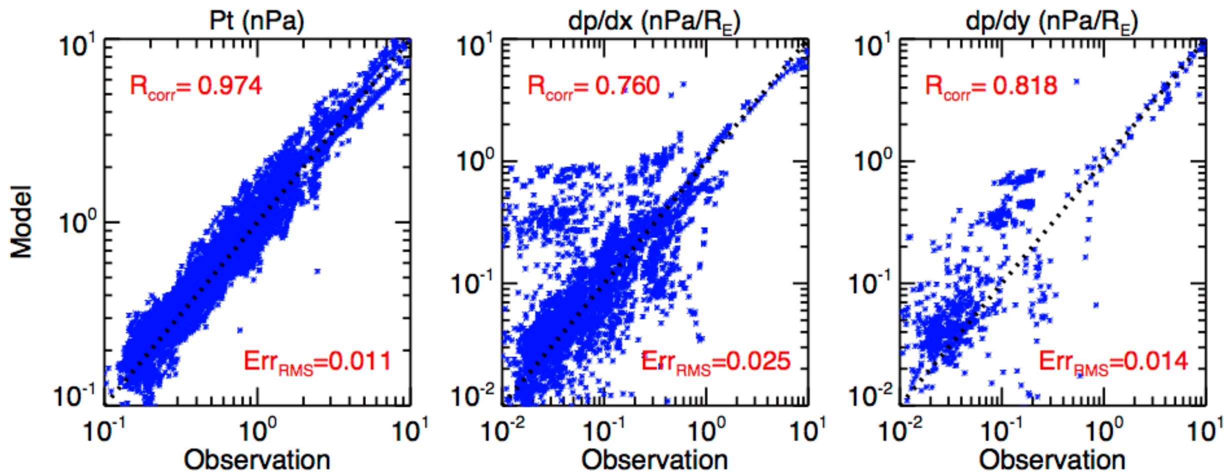

Figure 2.16. Comparison of the modeled and the observed pressures and pressure gradients in directions of X_{GSM} and Y_{GSM}. R_{corr} is the linear correlation coefficient between Pm and P_{obs}. Err_{RMS} is the normalized RMS error.

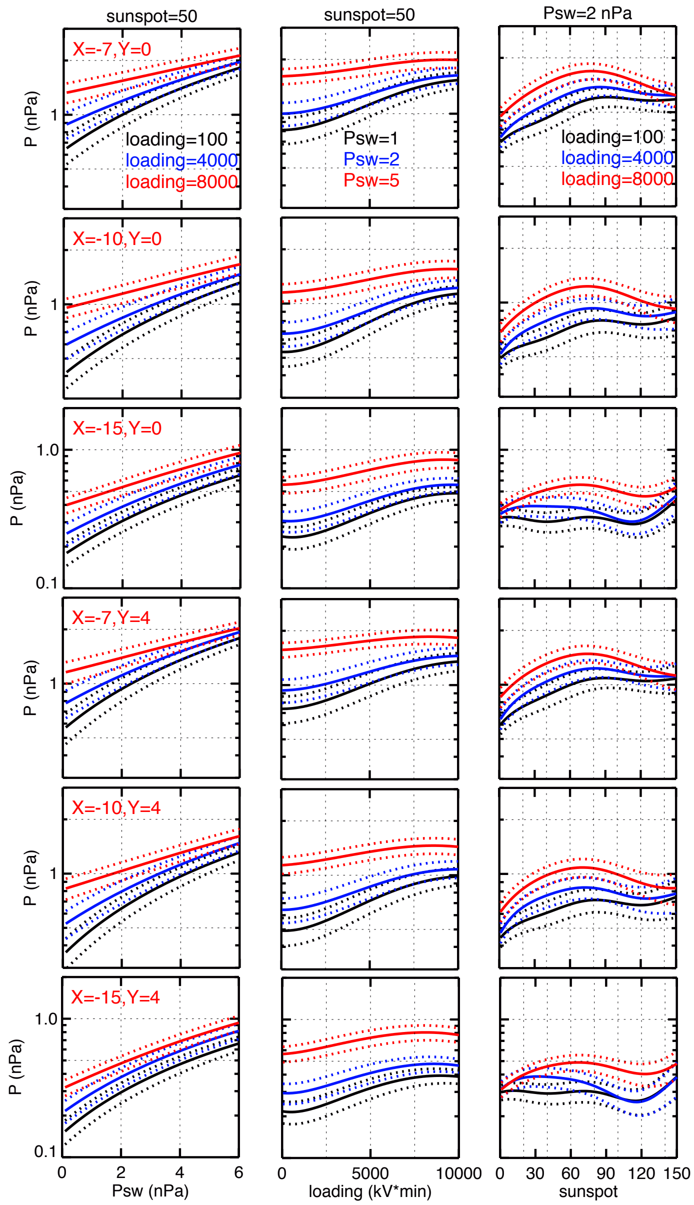

Figure 2.17. The modeled equatorial (Br = 0) pressures and their error bounds at different radial distance of pre-midnight and midnight meridian as functions of P_{SW}, PCPAE loading and sunspot number within their reliable ranges. Left column: the red, blue and black lines represent PCPAE loading at 100, 4000 and 8000 kV-min, respectively and sunspot number = 50 for all cases. Mid column: the red, blue and black lines represent P_{SW} equals 1, 2 and 5 nPa, respectively and

sunspot number = 50 for all cases. Right column: the red, blue and black lines represent PCPAE loading at 100, 4000 and 8000, respectively and P_{SW} = 2 nPa for all cases.

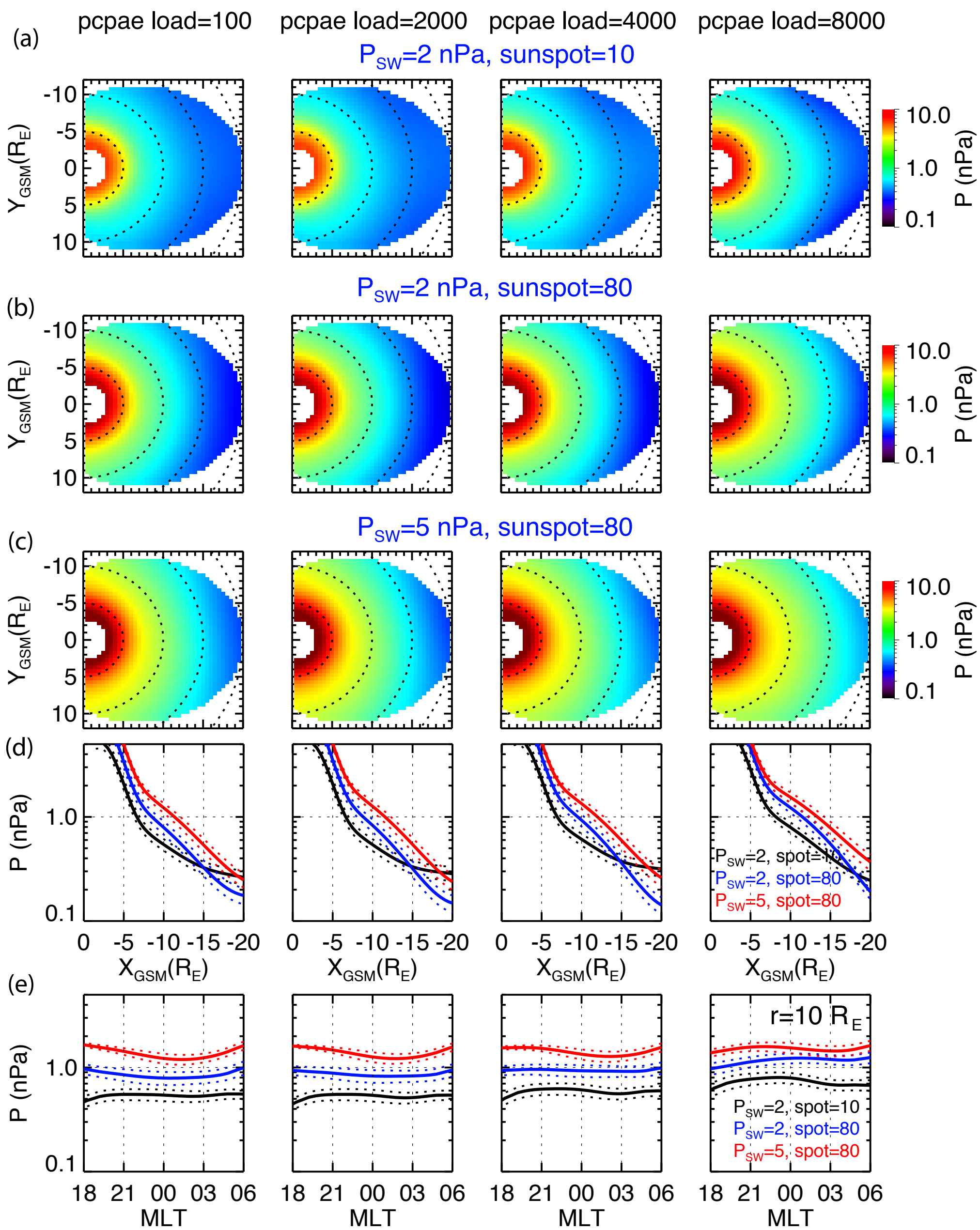

Figure 2.18. Distribution of modeled pressures on the equatorial plane and their radial and azimuthal (at r = 10 R_E) profiles with error bounds for 4 energy loading cases (PCPAE loading = 100, 2000, 4000, 8000 kV-min) with different control parameters. (a) P_{SW} = 2 nPa, sunspot = 10;

(b) P_{SW} = 2 nPa, sunspot = 80; (c) P_{SW} = 5 nPa, sunspot = 80; (d)-(e): The radial and azimuthal pressure profile with different control parameters. The black, blue and red lines are for P_{SW} = 2 nPa, sunspot = 10; P_{SW} = 2 nPa, sunspot = 80; P_{SW} = 5 nPa, sunspot = 80, respectively.

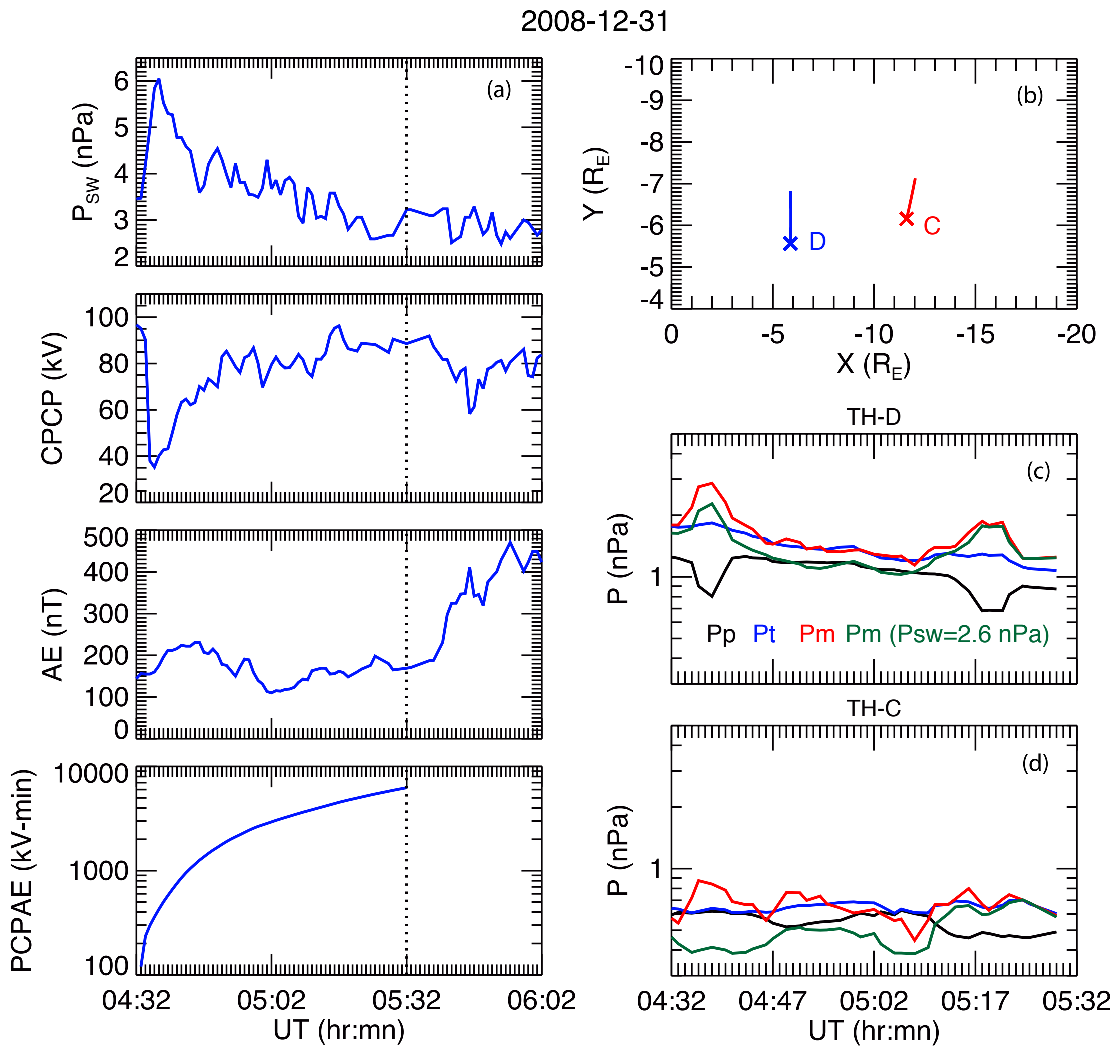

Figure 2.19. Example of modeled and observed pressure comparison during 60 min growth phase of Dec 31, 2008 substorm. The substorm onset is occurred at 05:32UT from aurora. (a) The variation of P_{SW}, CPCP, AE and the PCPAE loading based on OMNI data 1 hour prior to and 30 min after onset. The dashed vertical line marks the substorm onset time. (b) TH-C and TH-D trajectories at X-Y plane in GSM coordinates. The blue and red lines are the TH-D, TH-C,

respectively. (c)-(d) The comparison of the modeled and observed pressures from TH-D and TH-C. The black, blue, green and red lines are the observed plasma pressure, total pressures, the model pressure with constant P_{SW} = 2.6 nPa and the modeled pressure with time-dependent P_{SW}, respectively.

CHAPTER 3 | Dependences of Plasma Pressure, Magnetic Field and Current Structures on Kp and P_{SW}

Using the modeling framework and observational data described in Chapter 2, the plasma sheet plasma, magnetic field, and current structures for different Kp and P_{SW} levels are investigated. The stability of the 3D pressure and magnetic field configurations and the major differences between my force-balanced magnetic field and the non-force-balanced Tsyganenko 89 (T89) magnetic field model are then discussed [*Tsyganenko*, 1989].

3.1 Plasma pressure, magnetic field, and current structures under different Kp and P_{SW}

To understand the characteristic differences in the magnetic field configurations in response to increasing Kp and P_{SW}, we computed force-balanced magnetic field for Kp = 1 and 3 and P_{SW} = 1.5 and 3 nPa using the empirical analytical pressure distribution model described in Chapter 2.1.1. In this section, we investigated how the pressure, magnetic field, and current density profiles obtained from the 3D magnetic field model in the equatorial plane and along the midnight meridian change with increasing geomagnetic activity (Kp) and solar wind dynamic pressure (P_{SW}). Figure 3.1 shows that absolute differences between ∇P and **J**×**B** for the four cases are only about 1%, indicating very good force balance.

3.1.1 3D pressure, magnetic field, and current density profiles

Figure 3.2 shows the empirical plasma pressure model and the model Bz and westward azimuthal current density (J_φ) in the equatorial plane for four cases: Kp = 1 and 3 and P_{SW} = 1.5 and 3 nPa. As shown in Figure 3.2a, the plasma pressure has no significant azimuthal variations, and Bz is smaller at midnight than near the flanks while J_φ peaks around midnight. No dawn-dusk asymmetry is found in these profiles. Along the midnight meridian as shown in Figure 3.2b, plasma pressure, pressure gradient, and Bz increase, while plasma beta and magnetic flux tube volume decrease, with decreasing radial distance (*r*). Here flux tube volume has been taken from the equatorial plane to the ionosphere. The pressure and pressure gradient increase as Kp or P_{SW} increases. The Kp effect dominates in the near-Earth region inside r ~10 R_E (comparing the black with green curves or the blue with red curves), while P_{SW} affects plasma pressure mainly in the tail (comparing the black with blue curves or the green with red curves). As Kp increases, stronger convection electric field (see Figure 1f of *Wang et al.* [2013], the median cross polar-cap potential is ~30 kV for Kp = 1 and ~70 kV for Kp = 3) pushes the plasma sheet further inward, resulting in a larger increase in pressure in the near-Earth region than in the tail. To maintain force balance with this increased pressure gradient force, Bz decreases closer to the Earth but increases in the tail, while the J_φ peak intensifies and moves earthward and J_φ in the tail weakens. Accordingly, plasma beta increases in the inner magnetosphere but decreases in the tail. Additionally, the Bz changes cause the flux tube volume to decrease in the tail but increase in the near-Earth. As discussed in Section 3.1.4, magnetic field lines become more stretched.

The effect of increasing P_{SW} is global compression of the magnetosphere. As shown in Figure 3 of *Wang et al.* [2013], the effect on the plasma pressure is more significant in the tail than in the near-Earth region. As a result, there are overall increases in Bz and J_φ in the tail (in contrast to the decreasing J_φ with increasing Kp) but much smaller changes in the near-Earth region compared with the Kp effect. The plasma beta in the tail, on the other hand, remains similar as P_{SW} increases.

3.1.2 Variations in the Z-direction

The model results along the midnight meridian plane are shown in Figure 3.3a, and their variations with *Z* at X = –10 and –20 R_E are shown in Figure 3.3b. Plasma pressure decreases with increasing Z, since pressure is constant along field lines and field lines at higher Z map to larger equatorial distance where pressure is smaller. Bz, on the other hand, does not decrease monotonically with increasing r and Z. There is positive dBz/dr at Z ≥ ~1 R_E beyond X ~ –10 $R_{E,}$ and this feature moves earthward as Kp and P_{SW} increase. The positive dBz/dz has been observed by THEMIS [*Saito et al*., 2010; 2011], however no corresponding local Bz minimum in the equator plane as predicted by *Saito et al*. is seen in our magnetic field.

B_{XY} is seen to increase with Z. At the same Z, B_{XY} increases with increasing P_{SW} regardless of radial distance. However, during the higher Kp, B_{XY} increases at smaller r but decreases at larger r. As a result of the P decrease and B_{XY} increase, plasma beta decreases very quickly with increasing Z. Comparing the Z profiles of the B_{XY} with the Harris current sheet model [*Harris*, 1962] shows the current sheet thickness for Kp = 1 decreases from ~ 3 R_E just within the outer boundary at X = –30 R_E to ~1.4 at X = –13 and then increases again slightly to ~1.8 R_E at X = –10 R_E. The thickness minimum is collocated with the equatorial J_φ peak. As the plasma sheet moves earthward under higher Kp, the minimum also moves to inside X ~ –10 R_E while the overall thickness in the tail increases. The thickness and its X-profile do not change significantly with increasing P_{SW}. Constant J_φ contours are approximately aligned with the field lines.

Therefore, in the region earthward of the equatorial J_φ peak, J_φ at the same X is seen to first increase inside Z ~1 R_E then decrease with increasing Z, resembling a bifurcated current structure.

3.1.3 Field-aligned currents

Figure 3.4 shows the equatorial mapping of integrated field-aligned current (FACs) density $J_{||}$ in the ionosphere computed using the Vasyliunas equation [*Vasyliunas,* 1970, 1984]:

$$\frac{J_{||}}{B_{iono}} = \frac{\mathbf{B}_{eq}}{B_{eq}^2} \cdot \left(\nabla V \times \nabla P_{eq}\right)$$

where the subscripts 'iono' and 'eq' are referred to the values in the ionosphere and equatorial plane, respectively. Also shown are the magnitudes of the angle between ∇V and ∇P_{eq} for the four cases. Note that the FACs inside r ~6 R_E are not reliable due to larger uncertainty in the plasma pressure and azimuthal gradients. In the tail there are downward (upward) FACs at the pre-midnight (post-midnight) MLTs, which is the Region 2 (R2) FACs. There is no Region 1 FACs generated inside 30 R_E, indicating that the R1 FACs shown in the statistical *Iijima and Potemra* [1976a] are likely located in more distant tail (higher latitudes) and/or open field lines, not covered by our model domain. In addition, the R2 FACs move earthward together with the plasma sheet as Kp increases, but their magnitudes decrease mainly due to the decrease in radial flux tube volume gradient as well as the angle between ∇V and ∇P_{eq} as shown in Figure 3.4b. With increasing P_{SW}, despite a decrease in *dV/dr*, the overall FAC magnitudes are enhanced mainly due to an increase in pressure gradient and the angle between ∇V and ∇P_{eq} as demonstrated in Figure 3.4b. Additionally, despite little changes in their equatorial locations, as discussed in Section 3.1.4, their corresponding ionosphere latitudes do move equatorward due to the more stretched field lines. Furthermore, as shown in Figure 3.4c the total entropy $PV^{5/3}$ increases with increasing distance away from the Earth. The overall $PV^{5/3}$ has no clear change with increasing Kp. However, it increases with increasing P_{SW}, suggesting that the changes in pressures and flux tube volume associated with the P_{SW} effect are not simply due to adiabatic compression.

Some previous studies have suggested that substantial R1 FACs could be formed in the plasma sheet [e.g., *Wing and Newell,* 2000*; Zaharia and Cheng.* 2003]. However, *Wing and Newell* [2000] did not use a force-balanced magnetic field, limiting the validity of their results. *Zaharia and Cheng* [2003] used an artificial pressure profile having an assumed azimuthal pressure maximum at midnight closer to Earth, and an azimuthal pressure minimum farther down the tail. Their profile thus gives R2 FACs closer to the Earth and R1 FACs further away. On the other hand, *Zaharia* [2008] established 3D force-balanced magnetic field with a pressure profile having almost no azimuthal variations and obtained only R2 FACs in the plasma sheet.

FACs are determined by the angles between the gradients of V and P. As described in *Wang et al*. [2013], our analytical pressure model captures the smooth variations in the large-scale pressure. It shows azimuthal pressure gradients becoming smaller with increasing radial distance, but no change in the direction of the gradients. Thus the R2 FACs are seen to extend to our tail boundary. However, our prediction of the directions of FACs at large radial distances are not with absolute confidence, since the azimuthal variations of the observed pressure there are very small and the statistical uncertainty is large as shown in *Wang et al.* [2013].

Iijima and Potemra [1976b] showed that the R-2 FACs are larger with higher auroral electroject index. However, a higher auroral electroject can be associated with transient mesoscale disturbances in the plasma sheet such as bursty bulk flows (BBFs) The strong effect of BBFs on ionospheric currents has been seen in observations [*Lyons et al.,* 2013] and in simulations, such as the RCM-E [*Yang et al*., 2011], where BBFs generate mesoscale FACs with magnitudes comparable to or larger than those of the large-scale FACs. The BBFs create R2 sense FACs earthward of the BBFs and R1 sense FACs along the BBFs. BBFs are more frequent during higher Kp, however, such transient mesoscale variations are averaged out in our long-term smooth pressure profiles so their associated mesoscale FACs are not added into our large-scale FACs.

3.1.4 Field-line mapping

Magnetic field mapping is one of the most important applications of a 3D magnetic field configuration. Figure 3.5 shows comparisons of magnetic field line mappings for the different Kp and P_{SW}. Figure 3.5a shows the field lines originating from different fixed ionosphere latitudes. As Kp or P_{SW} increases, the magnetic field lines become more stretched with more significant stretching corresponding to the increasing Kp. Figure 3.5c shows the ionosphere mapping of the four equatorial line-segment locations shown in Figure 3.5b. At the same X, the field lines at smaller |Y| are mapped to lower ionospheric latitudes due to more stretched field lines at midnight than other MLTs. For structures along the same Y, the ionospheric mapping locations are aligned nearly longitudinally at midnight but become aligned much more latitudinally away from midnight. There is a slight dawn-dusk asymmetry with lower mapping latitudes at the post-midnight MLTs. The overall mapping latitudes are up to 0.5^{o} lower as P_{SW} doubles but can be more than 1^{o} lower as Kp changes from 1 to 3. It is important to remember that an observed equatorward (poleward) motion of ionospheric phenomena, for example aurora, does not necessarily correspond to an earthward (tailward) motion in the equatorial plane, and thus ionosphere motion may simply be associated with a change in the field line mapping.

3.1.5 Comparisons of observed magnetic field with force-balanced model magnetic field

Figures 3.6a and 3.6b show comparisons between the equatorial distributions of observed B_z near the equatorial plane (beta > 5) and the model B_z at Z = 0 from the force-balanced magnetic field model described in Chapter 2.2. The observed B_z in the plasma sheet for all Kp and P_{SW} is relatively lower at midnight than near the flanks, and the overall B_z in the plasma sheet increases with increasing Kp and P_{SW}. One exception is seen in the B_z near midnight beyond $X = -20$ R_E for Kp = 1 as it appears to decrease, rather than increase, with increasing P_{SW}. The model B_z reproduces reasonably well the spatial distributions and their overall response to Kp and P_{SW}. Figure 3.6c shows that the model Bz in the plasma sheet outside r ~10 R_E increases with decreasing *r* rather slowly for Kp = 1 but faster for Kp = 3, which agrees generally well with the observed radial variations with slightly lower magnitudes than the observations.

To evaluate the model magnetic field variations in the *Z* direction, we plot in Figure 3.7 how $|B|$ changes with plasma beta in the model and the observations. Plasma beta is used to represent *Z* variations since the exact *Z* distances to the equatorial plane cannot be determined in the observations and plasma beta decreases with increasing *Z*. Figure 3.7 shows that $|B|$ at lower beta (higher *Z*) increases with increasing Kp with larger increase seen at smaller *r*. Compared with the Kp effect, there are more significant increases with increasing P_{SW} and the increases are seen throughout the plasma sheet. The model $|B|$ agrees fairly well with the observations, in both magnitudes and their responses to Kp and P_{SW}. Therefore, our empirical pressure and the associated force-balanced magnetic field can well represent the observed 3D plasma pressure and magnetic field configurations and their dependences on Kp and P_{SW}.

3.2 Discussion

3.2.1 Plasma sheet stability

Plasma instability in the Earth's magnetosphere has been discussed in many studies, including large scale interchange instability [*Cheng,* 1985; *Southwood and Kivelson,* 1987; *Xing and Wolf,* 2007; *Xing,* 2008], and localized, explosive ballooning instability [*Cheng and Qian*, 1994*, Chen and Liu*, 1998]. To examine whether our pressure and magnetic field equilibriums are susceptible to interchange instability, we computed the growth rate against long wavelength perturbation $r \propto -\cos\alpha + \frac{\beta R}{2(1+\frac{5}{6}\beta)}$ [*Xing,* 2008; *Xing and Wolf*, 2013] where α is the angle between $\nabla PV^{5/3}$ and ∇V, $R = \frac{V}{PV^{5/3}}\left|\frac{\delta(PV^{5/3})}{\delta V}\right|$, and β is the plasma beta averaged over the entire flux tube. Figure 3.8a shows contour lines of flux tube volume and $PV^{5/3}$ for the Kp = 3 and P_{SW} = 3 nPa case. The two sets of lines are aligned with each other near midnight and have angles much smaller than π/2 in the flanks, implying that the plasma sheet is interchange stable. Figure 3.8b shows the growth rates estimated under the same conditions, the growth rates being close to –1 over the entire calculation domain of the plasma sheet. Similar growth rates are found for all other cases, indicating that the plasma sheet is interchange stable, consistent with the conclusion of *Xing and Wolf* [2007] derived from using non-force-balanced empirical plasma pressure and magnetic field models.

As discussed in the previous studies [e.g., *Lui et al.,* 1992, *Cheng and Lui*, 1998, *Cheng and Zaharia*, 2004], the criterion for the ballooning instability requires high plasma beta (> 50), and the most unstable modes are located in the strong cross-tail current sheet region [*Cheng and Lui*, 1998, *Cheng and Zaharia*, 2004]. As shown in Figure 3.2, the high beta region (beta > 50) is confined in tail region ($X < -10\ R_E$) and around midnight ($|Y| < 10R_E$) (not shown here). The peak of cross tail current is at r from 10 to 15 R_E, depending on activity level and solar wind driving, indicating that this is the most likely region to be unstable to the ballooning modes. This is also consistent with *Cheng and Zaharia* [2004].

3.2.2 Comparisons with the non-force-balanced T89 magnetic field

We compare our force-balanced magnetic field configurations with the statistical Geotail and THEMIS magnetic field profiles in Figure 3.6 and 3.7 and find fairly good agreement. In this section, we investigate if there is any characteristic differences between our magnetic field and the T89 field, which is not force balanced. The T89 is built by fitting the model field generated from a framework of postulated currents, including the ring current, tail current and magnetopause current as well as including the effect of warping the tail current sheet, to observed magnetic fields. Several studies have evaluated the T89 magnetic field against observations. *Weiss et al.* [1997] used a database of magnetic conjunctions between DMSP at low altitudes and LANL satellites at geosynchronous orbit to evaluate the accuracy of T89. They found that T89 is under stretched at geosynchronous orbit. In addition, *McCollough et al.* [2008] did a statistical comparison of commonly used external magnetic field models and concluded that T89 can only provide gross pictures of magnetosphere during quiet times, and does not predict well the dayside magnetic field.

Figure 3.9 shows the T89 magnetic field and J_φ for Kp = 1 and Kp = 3. From Figures 3.9a, 3.9b, and 3.9d, the equatorial Bz profiles and the increase in the tail Bz and decrease in flux tube volume with increasing Kp are qualitatively consistent with our results. However, there are three major differences from our magnetic field: (1) As shown in Figures 3.9c, the equatorial dBz/dr becomes positive beyond X ~ –15 R_E so that a local Bz minimum can be seen in the equatorial plane for both Kp levels. (2) There is no positive dBz/dz anywhere in the T89 field as shown in Figure 3.9e. (3) The T89 J_φ contours are not aligned with field lines so that currents always peak at the equator and monotonically decrease with increasing Z as shown in Figure 3.9f.

Figure 3.10 shows the difference of magnetic field lines mapping between our field and the T89 for Kp = 1 and Kp = 3. For Kp = 1, T89 mapping latitudes are very similar to our results for Kp = 1 and Psw = 1.5 nPa. This indicates the T89 can well represent the quiet time magnetic field configuration, consistent with the evaluation of *McCollough et al.* [2008]. For Kp = 3, the T89 maps to lower latitudes (up to 1^o) compared with our model, indicating that the T89 is over stretched during higher Kp levels.

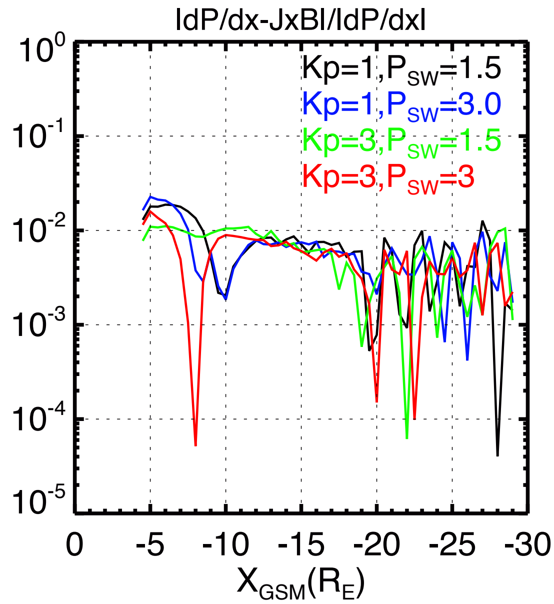

Figure 3.1. Illustration of achievement of force balance (plotted is the normalized residual force imbalance at midnight on the equatorial plane).

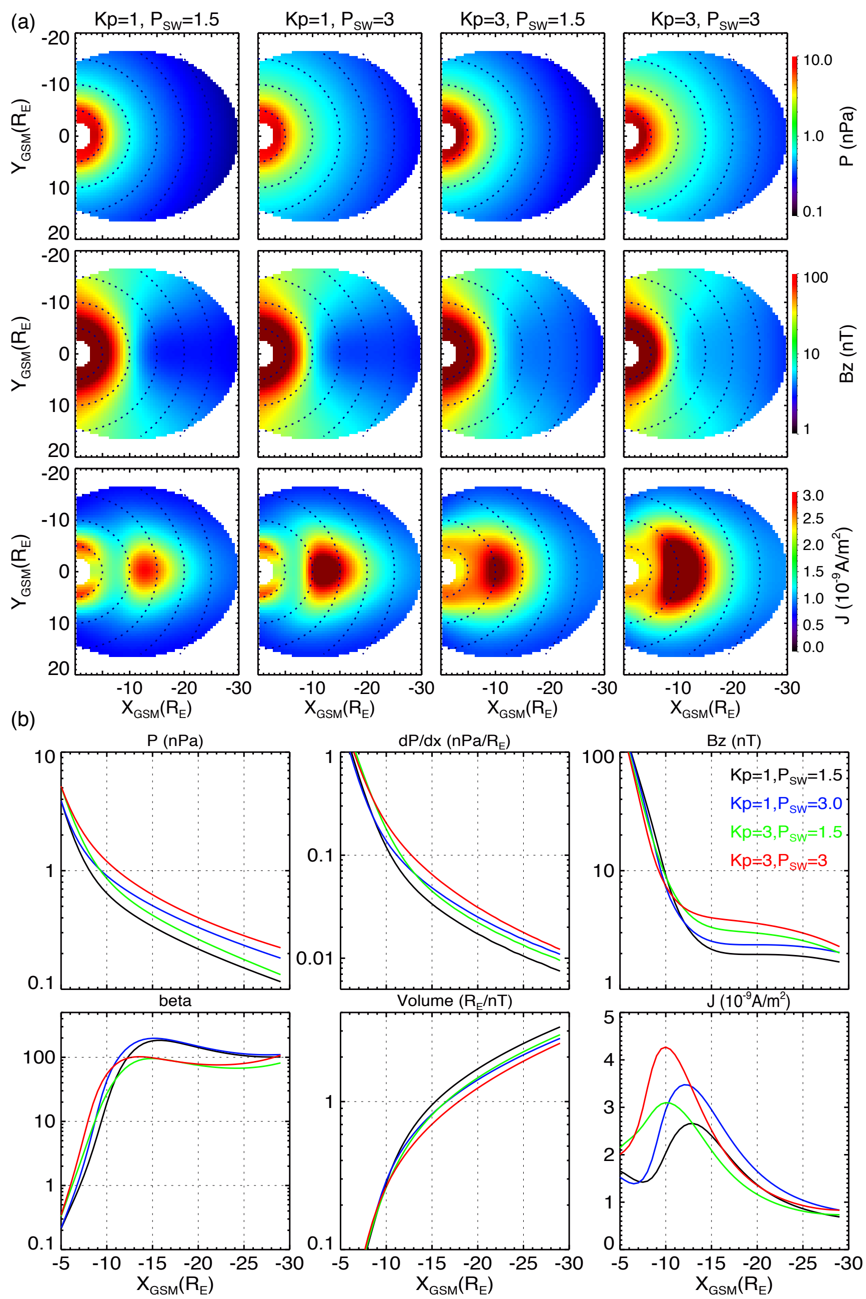

Figure 3.2. (a) Plasma pressure, Bz and westward J_φ on the nightside equatorial plane for the 4 cases. (b) The midnight radial profiles of equatorial plasma pressure, plasma pressure gradient, Bz, plasma beta, flux tube volume per unit flux from the equatorial plane to the ionosphere, and westward J_φ for the 4 cases (black: Kp = 1, P_{SW} = 1.5 nPa; blue: Kp = 1, P_{SW} = 3.0 nPa; green: Kp = 3, P_{SW} = 1.5 nPa; red: Kp = 3, P_{SW} = 3.0 nPa).

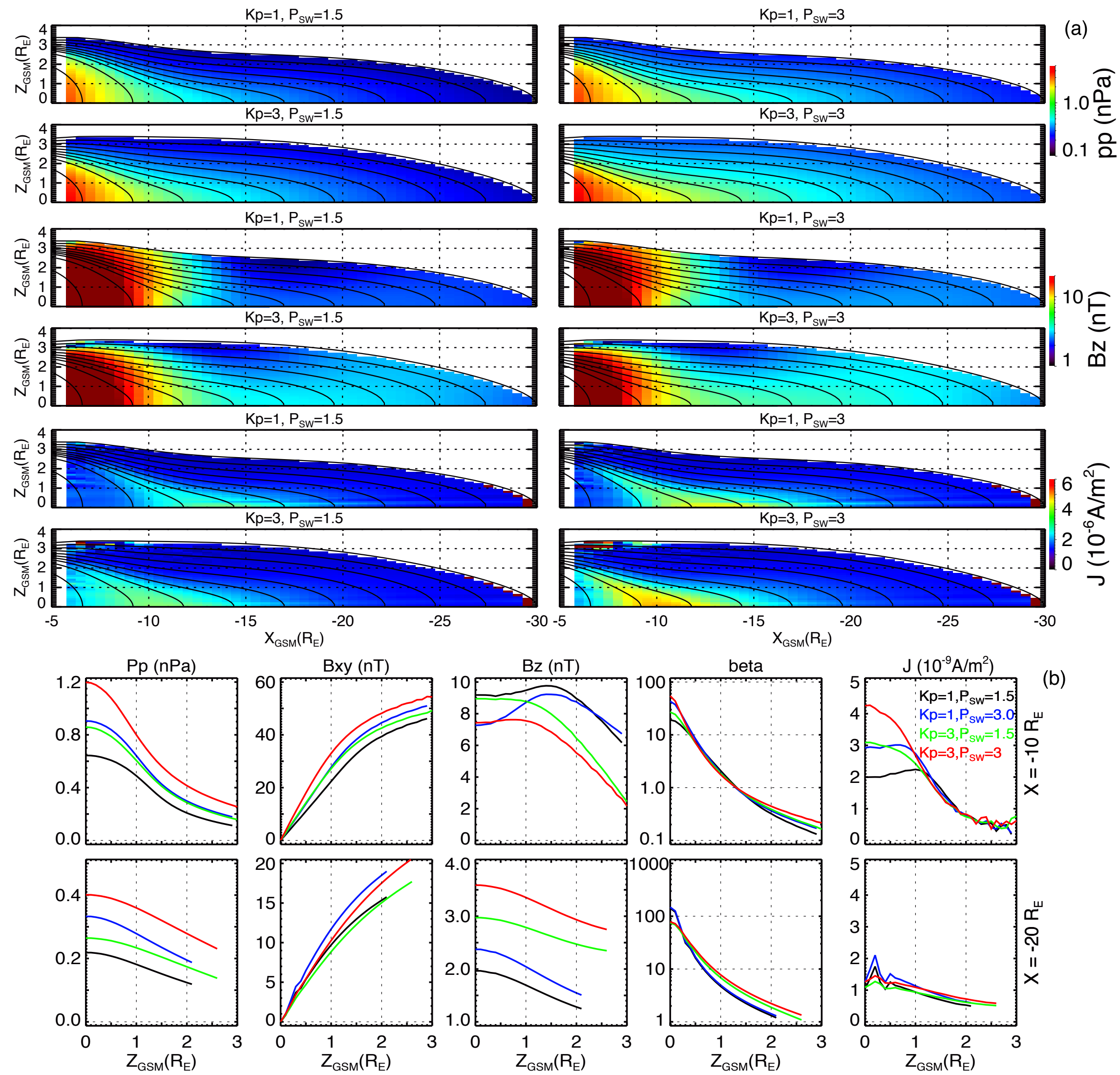

Figure 3.3. (a) Plasma pressure, Bz, and westward J_φ in the midnight X-Z plane for the 4 cases. The black curves are magnetic field lines. (b) The Z-profiles of plasma pressure, Bxy, Bz, plasma beta, and westward J_φ at Y = 0 and X = –10 and –20 R_E for the 4 cases (black: Kp = 1, P_{SW} = 1.5 nPa; blue: Kp = 1, P_{SW} = 3.0 nPa; green: Kp = 3, P_{SW} = 1.5 nPa; red: Kp = 3, P_{SW} = 3.0 nPa).

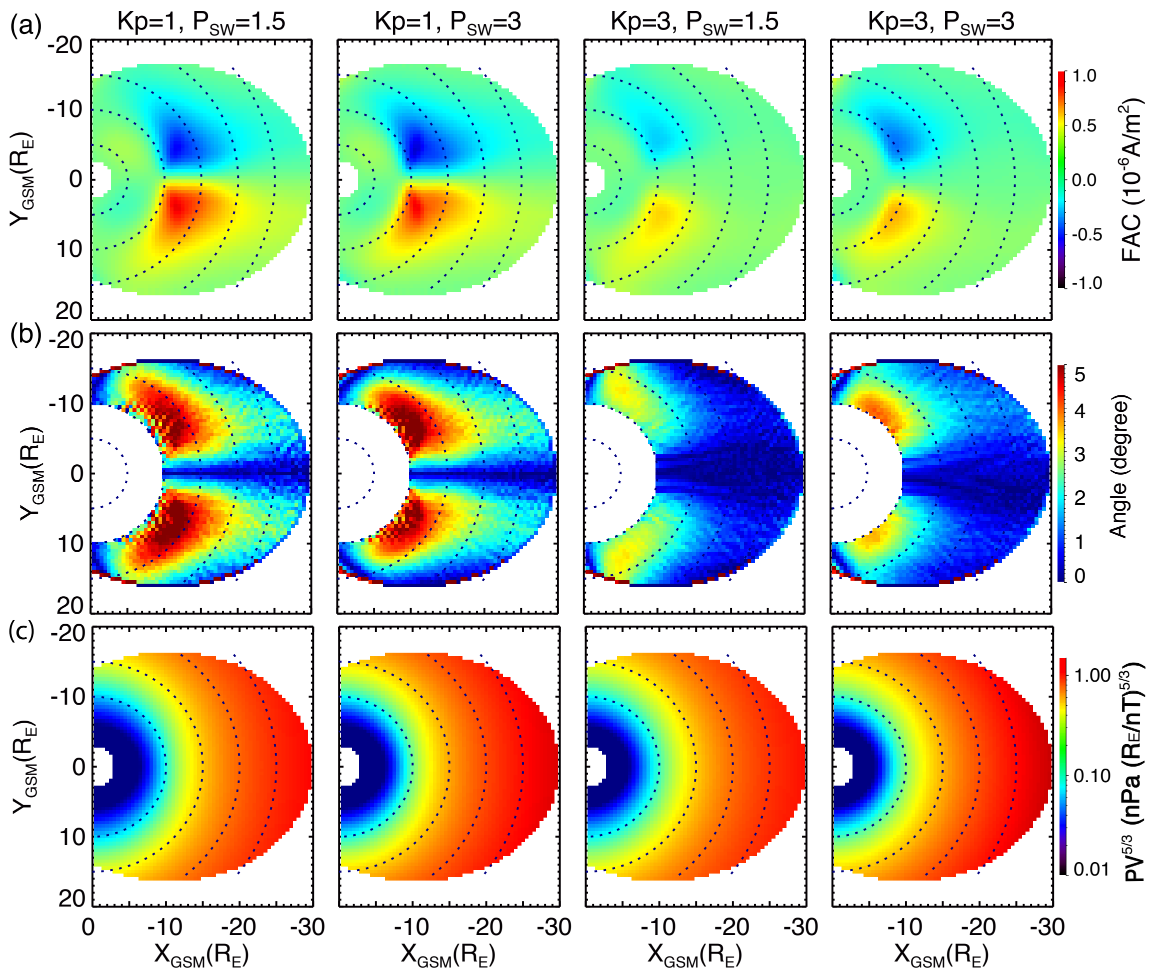

Figure 3.4. (a) The ionospheric FACs mapped to equatorial plane for one hemisphere. (b) the magnitude of the angle between ∇V and ∇P_{eq} for the 4 cases. (c) $PV^{5/3}$ distribution on the equatorial plane.

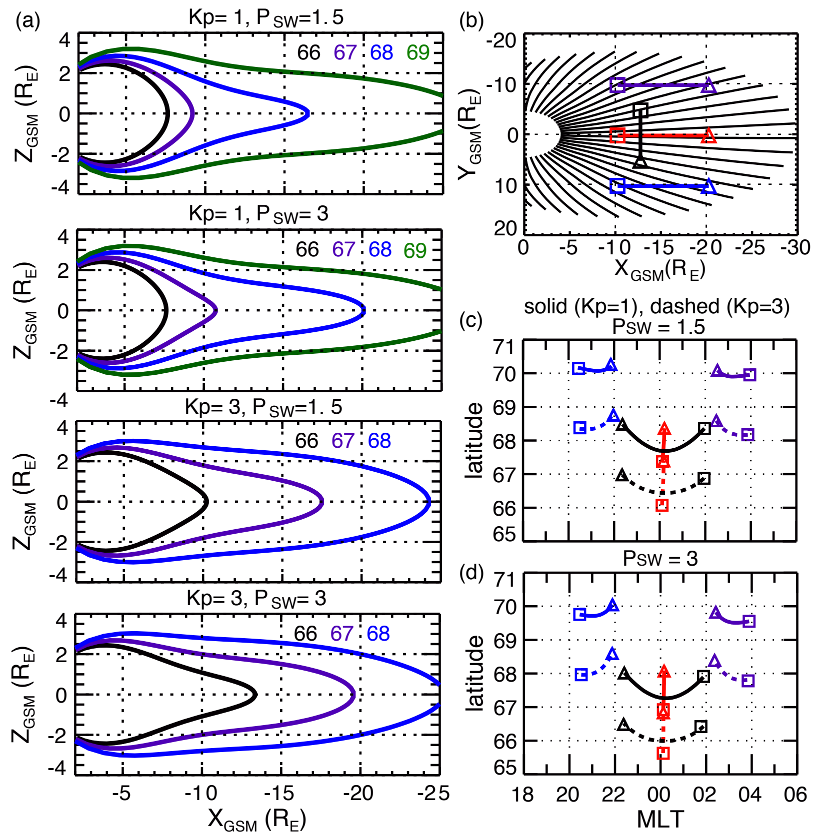

Figure 3.5. (a) Magnetic field lines from different ionospheric latitudes (66°: black curves; 67°: purple curves; 68°: blue curves; 69°: green curves) for the 4 cases. (c) Comparisons of the mapping latitudes between Kp = 1 (the solid curves) and Kp = 3 (the dashed curves) for different equator locations shown in (b) under P_{SW} = 1 (top) and P_{SW} = 3 nPa (bottom).

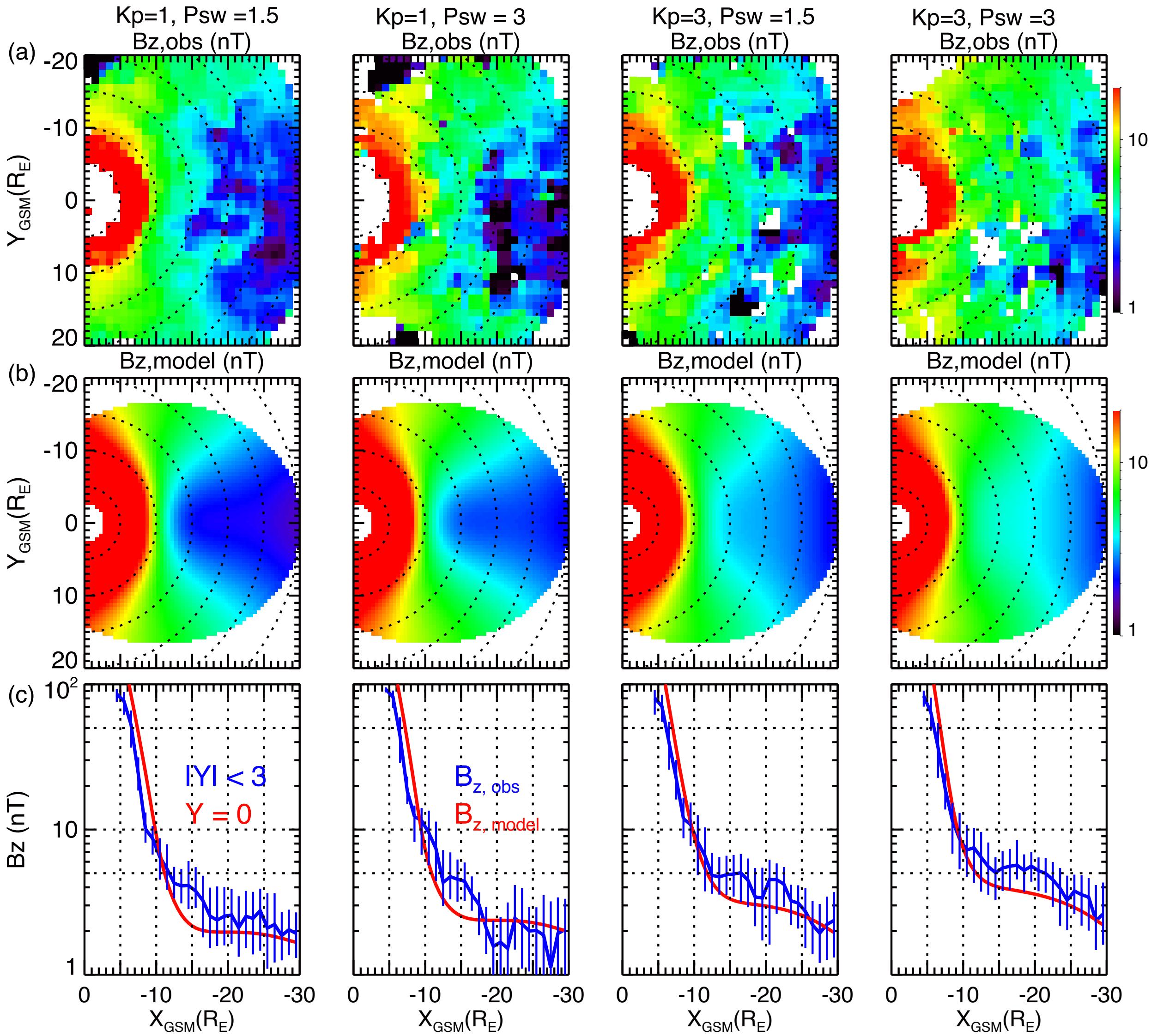

Figure 3.6. Equatorial distributions of (a) observed B_z and (b) model force-balanced B_z from Paper 2. (c) Comparisons of the radial profiles of observed B_z (the blue curves) and the model B_z (the red curves) near the midnight MLT.

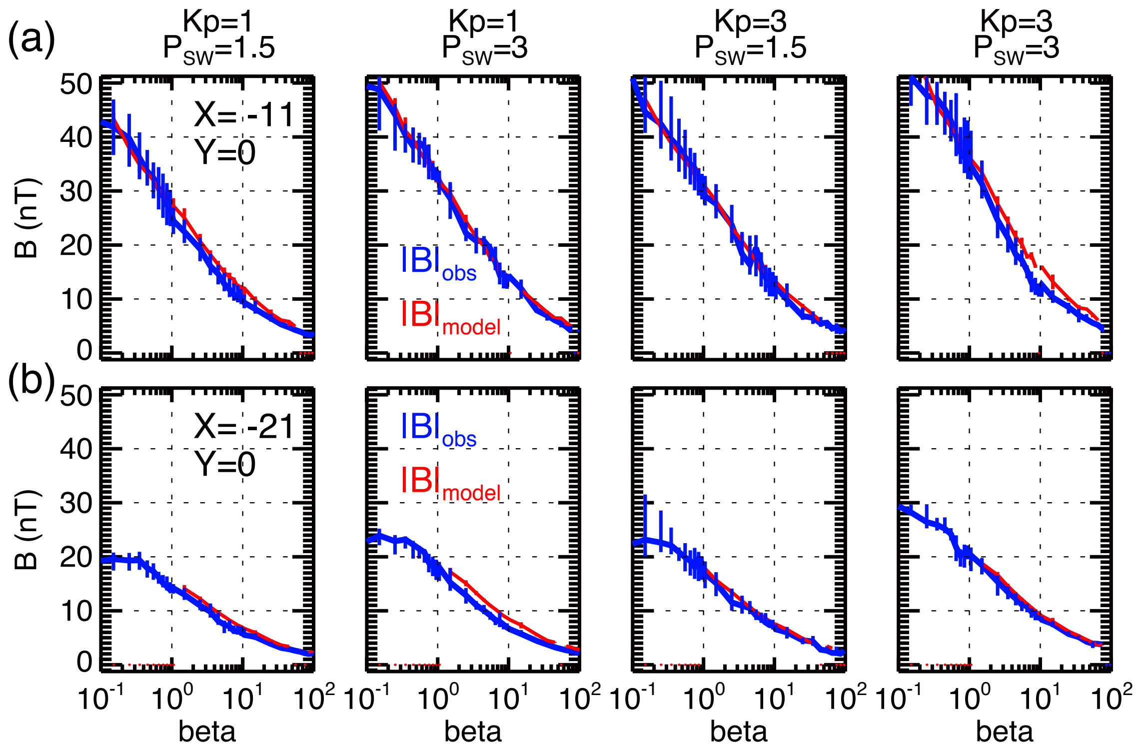

Figure 3.7. Total magnetic field as a function of plasma beta at (a) X = –11, Y = 0 R_E and (b) X = –20 and Y = 0 R_E for the observed (the blue curves) and model magnetic field (the red curves).

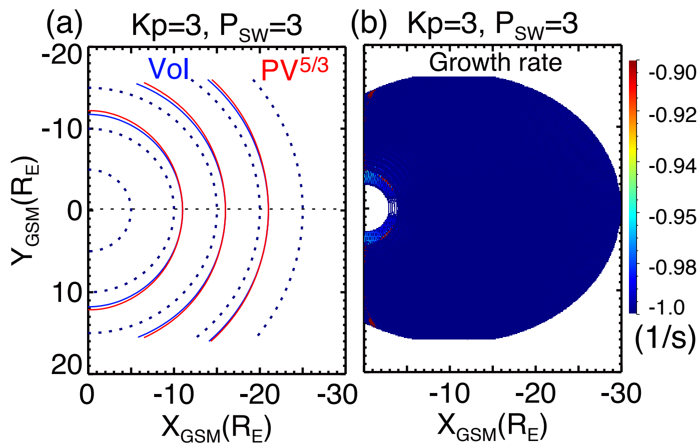

Figure 3.8. Illustration of interchange instability: (a) Contours of constant flux tube volume (Vol) and $PV^{5/3}$ in the equatorial plane and (b) the growth rate for interchange instability for Kp = 3 and P_{SW} = 3 nPa case.

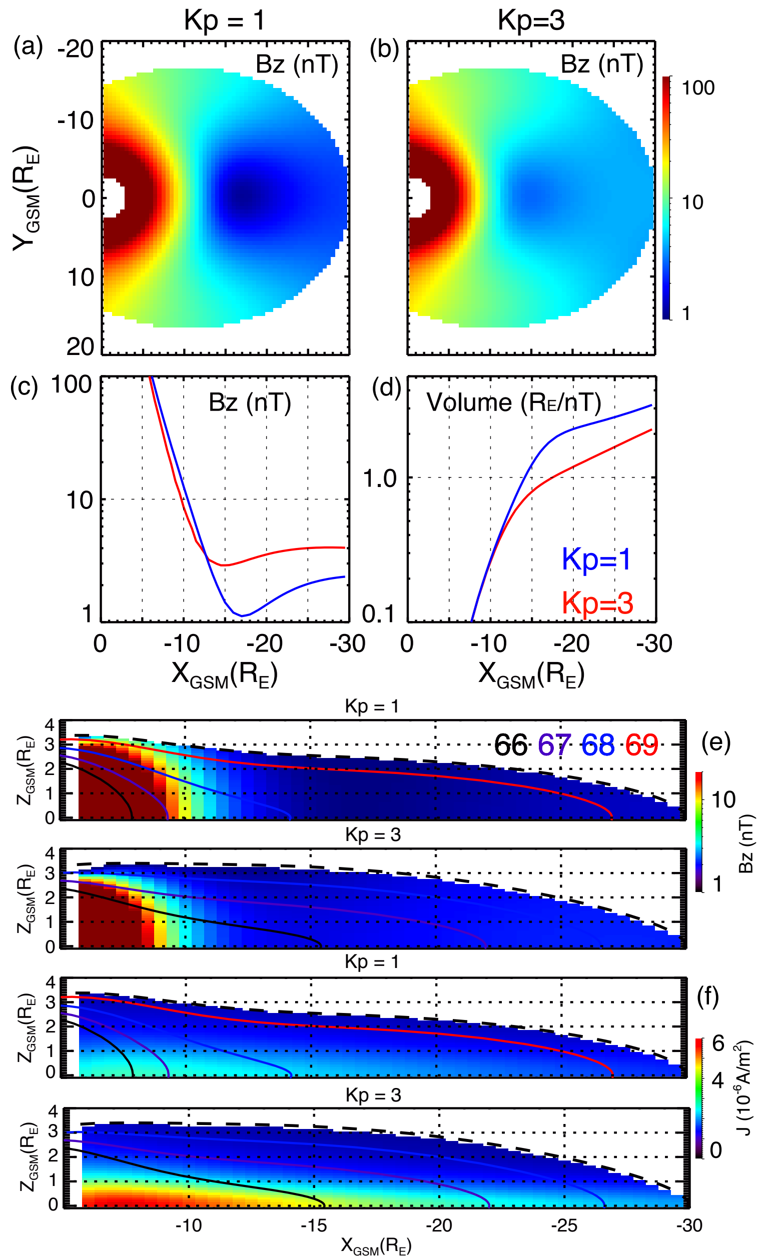

Figure 3.9. The T89 Bz in the equatorial plane for (a) Kp = 1 and (b) Kp = 3. The midnight radial profiles of (c) equatorial Bz and (d) flux tube volume form the T89 model for Kp = 1 (the blue curves) and Kp = 3 (the red curves). The X-Z profiles of (e) Bz and (f) westward J_φ along the midnight meridian from the T89 model for Kp = 1 and Kp = 3. The curves represent the T89 magnetic field lines from different ionosphere latitudes (66^o: black, 67^o: purple, 68^o: blue, 69^o:

red).

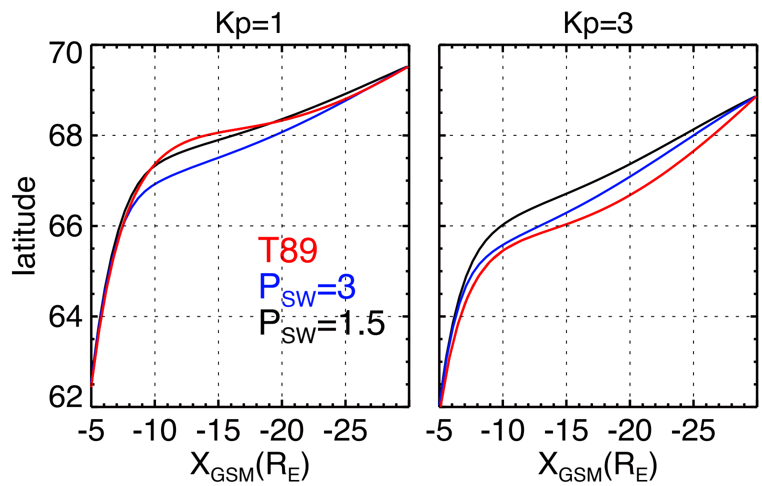

Figure 3.10. The mapping ionosphere latitudes versus the corresponding equatorial radial distance at midnight for Kp = 1 (the left panel) and Kp = 3 (the right panel) from the T89 and our model. The T89 results are shown in the red and our results for Kp = 1 in black and Kp = 3 in blue.

CHAPTER 4 | Current Sheet Scattering and Ion Isotropic Boundary

The stretched magnetic field configuration in the presence of a current sheet in the nightside part of the magnetosphere leads to pitch-angle scattering of particles due to violation of the first adiabatic invariant. When field lines become more stretched and the corresponding magnetic field curvature radius Rc becomes more comparable to the gyroradius ρ, particles undergo nonadiabatic pitch-angle scattering, resulting in isotropic pitch-angle distribution and filling of the loss cone. Based on the previous studies [*Sergeev and Tsyganenko*, 1982; *Sergeev et al*. 1983, 1988; *Sergeev and Gvozdevsky*, 1995], the pitch-angle scattering due to the current sheet becomes effective when the ratio of Rc to ρ is lower than ~8. The current sheet scattering is energy-dependent because of its ρ dependence. It is capable of scattering plasma sheet ions of thermal energy (> 1 keV), consistent with the observed isotropic populations [*Wang et al*., 2012]. By using the Tsyganenko-01 model, *Lvova et al*. [2005] showed that the protons with energies of ~80 keV, the transition between adiabatic and nonadiabatic behavior on the nightside occurs at 5−9 R_E at the equator under different solar wind conditions.

Current sheet scattering has been considered as a major cause of the isotropic boundary (IB) observed in the tail and at low altitudes, this boundary separating pitch-angle distributions with an empty loss cone from those with a full loss cone. As a low-altitude satellite moves poleward, it encounters first the IB at auroral latitudes and then the polar-cap boundary. The proton IB corresponds to the earthward edges of isotropic protons at the equator. It has been shown observationally that the latitude of the IB is a function of magnetic local time (MLT), particle energy, and the state of the magnetosphere. The ion IB and the equatorward boundary of the associated proton aurora are statistically located at higher magnetic latitudes at dusk and dawn than at midnight [*Donovan et al*., 2003a; *Lvova et al*., 2005]. The IBs are located at lower latitudes for higher energy ions [*Newell et al.,* 1998; *Shevchenko et al.* 2010] and under stronger geomagnetic activities [*Lvova et al*., 2005]. In addition to the current sheet scattering, wave-particle interaction can also cause pitch-angle scattering and filling of the loss cone. In the inner magnetosphere, EMIC waves can sufficiently scatter ions above 1 keV [*Jordanova et al*., 2001].

Past studies have provided evidence for the role of current sheet scattering in controlling the IB latitudes. For example, *Sergeev et al*. [1993] showed that the IB for 100 keV protons at various local times has a very high correlation (~ 0.9) with the inclination of the B-field as measured on the nightside at the geosynchronous orbit, indicating that the IB latitude is effectively controlled by the tail magnetic field. By using the Tsyganenko-01 model, *Ganushkina et al.* [2005] computed IB locations and compared them with the statistical distributions of the 31-80 keV proton IB measured by the Polar satellite at mid-altitudes and those observed by NOAA satellites at low-altitudes. They concluded that pitch angle scattering by the tail current sheet is the basic mechanism controlling the transition from isotropic to anisotropic distributions in the near-equatorial region. *Shevchenko et al.* [2010] investigated mapping accuracy in the T96, AM-01, and AM-02 models by comparing hundreds of 80 keV proton IBs observed by NOAA satellite with the model predicted IBs due to tail current sheet scattering. Their results indicate that a field model that can more accurately reproduce the observed magnetic field in the current sheet predicts better the IB latitudes. However, the above observational studies and comparisons with models focused mainly on high-energy ions (> 30 keV). For ions of the typical plasma sheet thermal energy (1 to 30 keV), the IB latitudes and the role of current sheet scattering remain to be determined from observations and models.

In the previous investigations of the role of current sheet scattering in controlling IBs described above, empirical magnetic field models were used. However, these empirical magnetic field models are not in force balance with observed plasma pressures and can overestimate or underestimate the magnetic fields in different regions [*McCollough et al.*, 2008]. The *Shevchenko et al.* [2010] study has pointed out the importance of using more accurate magnetic field model in predicting IBs.

In Chapter 2 and 3, we have developed an empirical modeling approach to obtain 3D force-balanced magnetic field configurations in the near-Earth magnetosphere inside 30 R_E that is entirely different from other empirical magnetic field modeling, such as the Tsyganenko models. Previous empirical models were built by fitting the model magnetic field from a framework of postulated currents to observed magnetic field. Our model magnetic field, on the other hand, is solved from the force-balance equation with observed equatorial plasma pressure. Since the model is not based on the observed magnetic field, we used magnetic field data for validation and found fairly good agreement over wide ranges of Kp and P_{SW}. Since our model is in force-balance and shows good agreement with magnetic field observations, it should provide better estimates of current scattering and the associated IB than do other empirical magnetic field models.

In this Chapter, we estimate the current sheet scattering of 1-30 keV ions using our force-balanced magnetic field, identify the equatorial IBs from the THEMIS observations and low-altitude IBs from the FAST measurements, and determine the role of current sheet scattering through the model-observation comparisons. With the computed 3D force-balanced magnetic fields described in Chapter 3, we are able to calculate the field curvature radius Rc, the proton gyro-radius ρ, and tail current sheet (TCS) scattering parameter, $K = Rc/\rho$, in the equatorial plane using Rc = Bz/(dBr/dz), where Bz is the equatorial magnetic field and Br is the radial component of the magnetic field off the equatorial plane, ρ = mV/eBz, where m is the mass; V is the velocity of the particle; e is the electron charge.

4.1 Current sheet scattering in the plasma sheet

Figure 4.1 shows the radial variations of the main parameters obtained from the 3D force-balanced magnetic field and the associated TCS scattering parameter K for Kp = 1, P_{SW} = 1.5 (Figure 4.1a) and for Kp = 3 and P_{SW} = 3 (Figure 4.1b). The top panels show the magnetic field lines along the midnight meridian originated from different ionospheric latitudes (different colors indicate different latitudes). The second panels show the equatorial magnetic field B_Z. The third panels show the Br component at Z = 0.5 R_E. The last three panels show the equatorial field line curvature radius, gyro-radius, and K for protons of two typical near-Earth plasma sheet energies (1 keV in blue lines and 30 keV in red lines). The solid horizontal black line in the bottom panels marks K = 8. As shown in Figure 4.1a and 4.1b, B_Z decreases sharply with increasing radial distance r from dipole-like to tail-like. This transition region is at ~12 R_E for Kp = 1 and moves earthward to ~9 R_E for Kp = 3. Tailward of the transition region, B_Z decreases slowly with increasing r in the magnetotail. Similar radial variations are seen in Br. As discussed in Chapter 3, the earthward motion of the transition region is a result of the magnetic field at smaller r becoming more stretched. This strengthens the magnetic force to balance the increased pressure gradient resulting from the enhanced earthward driving of the plasma sheet by stronger convection during higher Kp. The curvature radius computed from Br is about 1 R_E in the inner magnetosphere but drops sharply at ~8 (6) R_E to a minimum value of 0.15 (0.25) R_E at ~13 (11) R_E for Kp = 1 (3). The variation of Bz causes the gyro-radius ρ to rapidly increase outward from the Earth in the transition region and then increase gradually in the tail. For protons of the same energy, the gyro-radius for Kp = 3 is larger in the inner magnetosphere and smaller in the tail than that for Kp = 1. As a result of the above radial variations of the curvature radius and the gyro-radius, the K values of 30 keV protons for Kp = 1 is ~100 at r ~ 5 R_E and drops rapidly to 8 at r = 8 R_E and remains below 8 in the tail. This indicates that the 30 keV protons tailward of r = 8 R_E are expected to undergo pitch-angle scattering and have an isotropic pitch-angle distribution with a filled loss cone, while those earthward of r = 8 R_E do not. The IB for the 30 keV protons is thus located at r = 8 R_E at midnight. The IB moves earthward for the same proton energy during higher Kp, or for higher energy under the same Kp.

Figure 4.2 illustrates the equatorial distributions of the scattering parameter K for 1 and 30 keV protons for different Kp and P_{SW} levels. It can be seen that the K values for different energy protons have similar spatial variations with K being the lowest at midnight tail and increasing toward the dawn and dusk flanks and toward the Earth. The black stars mark the IB locations where K = 8. The IB location is closest to the Earth at midnight and moves to larger r toward dawn and dusk due to the magnetic field being more stretched at midnight than at dawn and dusk. The IB for the same energy at all MLTs moves earthward with increasing Kp or P_{SW}. For the same Kp and P_{SW} level, the IBs for 30 keV protons at all MLTs are a few R_E earthward of those for 1 keV protons.

Protons in the equatorial plasma sheet tailward of IB are expected to be isotropized by TCS scattering, thus becoming highly isotropic in their pitch-angle distributions. We investigated the pitch-angle anisotropy of ions of different energies observed by THEMIS from the tail plasma sheet to the inner magnetosphere. The anisotropy is indicated by A,

$$A \equiv \frac{\int_0^{\pi/2} f(\alpha_0)\sin^3\alpha_0\, d\alpha_0}{\int_0^{\pi/2} f(\alpha_0)\cos^2\alpha_0 \sin\alpha_0\, d\alpha_0} - 1$$
,

where *f* is phase space density and α_0 is pitch-angle. A pitch-angle distribution with $|A| < 0.1$ is considered highly isotropic. Figure 4.3 shows the occurrence rates of highly isotropic ions of 12.3 and 27.7 keV observed by THEMIS as well as the modeled IB for these two energies (black stars) for different Kp and P_{SW} levels. (The observed anisotropy for 1 keV ions is not compared because it has been shown to be strongly affected by field-aligned ionosphere outflow during disturbed time [*Wang et al.*, 2012]). The occurrence of isotropic distribution is high at larger r but drops sharply to very low in the inner magnetosphere. The sharp drops for 27.7 keV are located at smaller radial distances than those of 12.3 keV. The locations of the sharp drops match reasonably well with the modeled IBs for both energies at midnight and post-midnight MLTs, indicating that TCS scattering is likely the main isotropization mechanism. However, near dusk during higher Kp levels, occurrence is still high in the region earthward of the modeled IB. Simulations have shown that enhanced EMIC waves during a storm can result in pitch-angle scattering predominantly in the inner magnetosphere from the dusk to noon MLTs [*Jordanova et al.,* 2001]. THEMIS wave observations also show that EMIC waves are more frequently observed in that region [*Usanova et al.*, 2012]. Thus isotropization due to higher wave power during higher Kp may account for this discrepancy near dusk.

4.2 Isotropic boundary latitudes

Strong pitch-angle scattering by the TCS or waves results in filling of the loss cone. Thus an IB should be a boundary separating distributions with or without filled loss cone. However, the loss cone at the equator is much smaller (~1 degree or so) than the pitch-angle resolution of particle detectors, for example, 22 degrees for the THEMIS detectors, is far larger than the size of the equatorial loss cone. It is thus worthwhile to also examine observations from a low-altitude satellite, such as FAST, to determine the IB. Figure 4.4 illustrates three examples of IB observed by FAST. The top three panels show the ion energy fluxes above 1 keV as a function of latitude over three different pitch-angle ranges. FAST was in the northern hemisphere in these three passes, so the particles at 0-30^o pitch-angle are within the downward loss cone, those at 60-150^o pitch-angle are trapped, and those at 150-210^o pitch-angle are within the upward loss cone going away from the ionosphere. The last panel shows the ratio between the precipitating fluxes and the trapped fluxes, a ratio of 1 indicating a completely full loss cone. The IB can be identified as the boundary where the ratio drops sharply from 1.

In Figure 4.4a, the IB latitudes show strong energy dependence, decreasing approximate linearly with increasing *ln*(E), consistent with what would result from the TCS scattering. However, sometimes the IB has almost no energy dependence as shown in Figure 4.4b. There are also limited cases with the IB latitude higher for higher energy ions as illustrated in Figure 4.4c. This is likely due to scattering by EMIC waves, since EMIC waves are capable of scattering lower energy protons into loss cone more efficiently based on simulated pitch-angle diffusion coefficients [*Liang et al,* 2014]. Since the IBs caused by the TCS and by waves have opposite energy-dependences, the IB shown in Figure 4.4b and many more cases with complex IB latitude distributions may result from a combination of both TCS and wave scattering.

Figure 4.5 shows statistical distributions of the IB latitudes observed by FAST as a function of MLT for different Kp and P_{SW} levels. These IB events are selected by examining the FAST pitch-angle spectrograms of ion energy flux integrated from 1 keV to the highest available energy channel (approximately 20 keV), and the IB latitudes are determined as the location of a sharp transition from a near-isotropic distribution (except for an upgoing loss cone) to a near-empty downgoing loss-cone occurs as illustrated in Figure 2 of *Donovan et al*. [2003b], and thus the IBs here include all the different types of IB as discussed above. The FAST IB latitude is the lowest at midnight and moves to higher latitudes towards dawn/dusk. The IBs move to lower latitudes as Kp or P_{SW} increases. Also shown in Figure 4.5 are the modeled IBs of 10 (blue lines) and 30 keV (red lines) protons mapped to the ionosphere for different Kp and P_{SW}. It can be seen that the dependences of modeled IB latitudes on MLT, Kp, and P_{SW} are consistent with those of the FAST IBs, indicating TCS scattering is a major mechanism for the IB formation.

As shown in Figure 4.2, the modeled equatorial IB is closer to the Earth at midnight than at dawn and dusk due to tail magnetic field being more stretched at midnight. In addition, the equatorial IBs map to lower latitudes under more stretched field lines. Thus the IB latitude is the lowest at midnight. Similarly, higher Kp or P_{SW} causes stronger cross-tail current and thus more stretched magnetic field lines, resulting in earthward motion of the equatorial IB and lower mapping latitudes of IB. The modeled IB matches fairly well with FAST IB for Kp = 0. As Kp becomes higher, the agreement at midnight remains generally good but discrepancy becomes larger at other MLTs, more so at the pre-midnight MLTs. The lager discrepancy near dusk is similar to that seen in the equatorial comparisons shown in Figure 4.3, and can be likely contributed by scattering by EMIC waves.

4.3 Isotropic boundary due to current sheet scattering

Our results indicate that current sheet scattering is generally the dominant mechanism for the IB formation except on the duskside during active times where we often see discrepancies. To further investigate if TCS scattering can account for the energy-dependence of IBs during active times when the effects of other processes are minimized, we selected cases having the observed at higher latitudes for lower energy like the example shown in Figure 4.4a. We identified 339 FAST IB cases with IB showing clearly this kind of energy dependence for Kp = 3 (255 out of 2170 cases) and for Kp = 4 (84 out of 1034 cases). For high Kp cases, due to the increasing wave activity and disturbances such as tail flow bursts and substorms, the clear energy dependence cases as shown in Figure 4.4a are infrequent.

To quantify the energy-dependence, we define a slope parameter, slope = (lat1–lat2)/(ln(E1)–ln(E2)), here we choose E1 = 1 keV and E2 is the highest energy measured by the ESA (varies from 16 to 25 keV), and lat1 and lat2 are the IB latitudes corresponding to energies E1 and E2, respectively. We choose to use logarithm because the IB shows more clearly the linear dependence with logarithmic energy as illustrated in Figure 4.4a. Figure 4.6 shows the slope comparisons between our model (the red curves) and the observation (the blue curves) as a function of MLT for Kp = 3 and 4 (note that the observation result is only sorted with Kp). It can be seen that the modeled slopes match reasonably well with the FAST slopes, This further confirms the important role of TCS scattering in the IB formation, but also implies that other processes can be important when magnetic activity is high.

4.4 Comparison of T89 modeled IB with FAST observations

As discussed in Chapter 3, our force-balanced magnetic field configurations in the tail plasma sheet are characteristically different from those of the T89 field. Here we investigate the difference in the IB predictions between the T89 and our field. Figure 4.7 shows modeled IBs computed from the T89 fields for 10 and 30 keV protons under different Kp and their comparisons with the FAST IBs. Since the only control parameter for the T89 model is Kp index, we have binned the FAST IB observation to different Kp levels only (including all P_{SW} levels) in Figure 4.7. In general, the T89 IBs move to higher latitudes from midnight towards dawn/dusk and they move to lower latitudes as energy increases, similar to the IBs computed from our force-balanced fields. In general, T89 IB latitudes are higher than the FAST IB latitudes for all Kp levels, and the discrepancy is larger at the pre-midnight than post-midnight MLTs for Kp > 2. Compared with our results shown in Figure 4.5, our IBs are closer to the observed IBs, particularly for high solar wind dynamic pressure and/or low Kp levels. In addition, the latitude difference between the 10 and 30 keV T89 IBs is ~0.8, about a factor of 2 larger than that in our IBs. Figure 4.8 shows the slope comparisons between the T89 and FAST IBs for Kp = 3 and 4. The T89 slope matches relatively well with the observations for Kp = 3 but less well for Kp = 4. On the other hand, our slopes shown in Figure 4.6 have good agreement with the observations for both Kp = 3 and 4. The above improvement in predicting the IBs achieved by our model indicate that taking into account the physical requirement of force-balance leads to a more accurate description of the magnetic field configuration, and also reinforces the confidence in our conclusions regarding the role of current sheet scattering for < 30 keV ions.

4.5 Discrepancy between our modeled IB and the observations

As shown above, our modeled IB displays some discrepancies with the THEMIS/FAST observation, especially around the duskside during geomagnetic active times. In addition to the wave scattering mentioned previously, it can also be due to our model underestimating the ring current pressure and thus magnetic field stretching in the inner magnetosphere during more active time. For the empirical pressure model we established and used as the input for computing the force-balanced magnetic field, the pressure data inside r = 8 R_E are from the THEMIS measurements between 2007 and 2010, a period that closely surrounds the solar minimum. We compared the probability distributions of Dst and P_{SW} for the periods of 2007-2010 and 1997-2002 (the period for the majority of the FAST data used in the statistics shown in Figure 4.5). There is no clear difference in P_{SW} during different Kp levels. However, the difference in Dst is small when Kp is low but becomes larger with increasing Kp. For Kp = 4, the average (standard deviation) is -29 (±20) nT for 2007-2010 and -19 (±14) nT for 1997-2002. The relatively lower Dst during the THEMIS period indicates relatively lower ring current pressure and less stretched field lines, which likely contributed to the latitude discrepancy between our predicted IB and the FAST IB. Therefore, in the future, adjusting the model ring current pressure by a factor based on the Dst during the target period, as well as including more data in our empirical pressure model from THEMIS and other satellites during different phases of a solar cycle, should further improve the accuracy of our modeled magnetic field configuration.

In addition, the disagreement during geomagnetic active time may arise from other processes such as those related to tail flow bursts and substorm expansions. It is well known that flow bursts and substorms have a preference for the premidnight region, suggesting a dawn-dusk asymmetry scattering related to these disturbances.

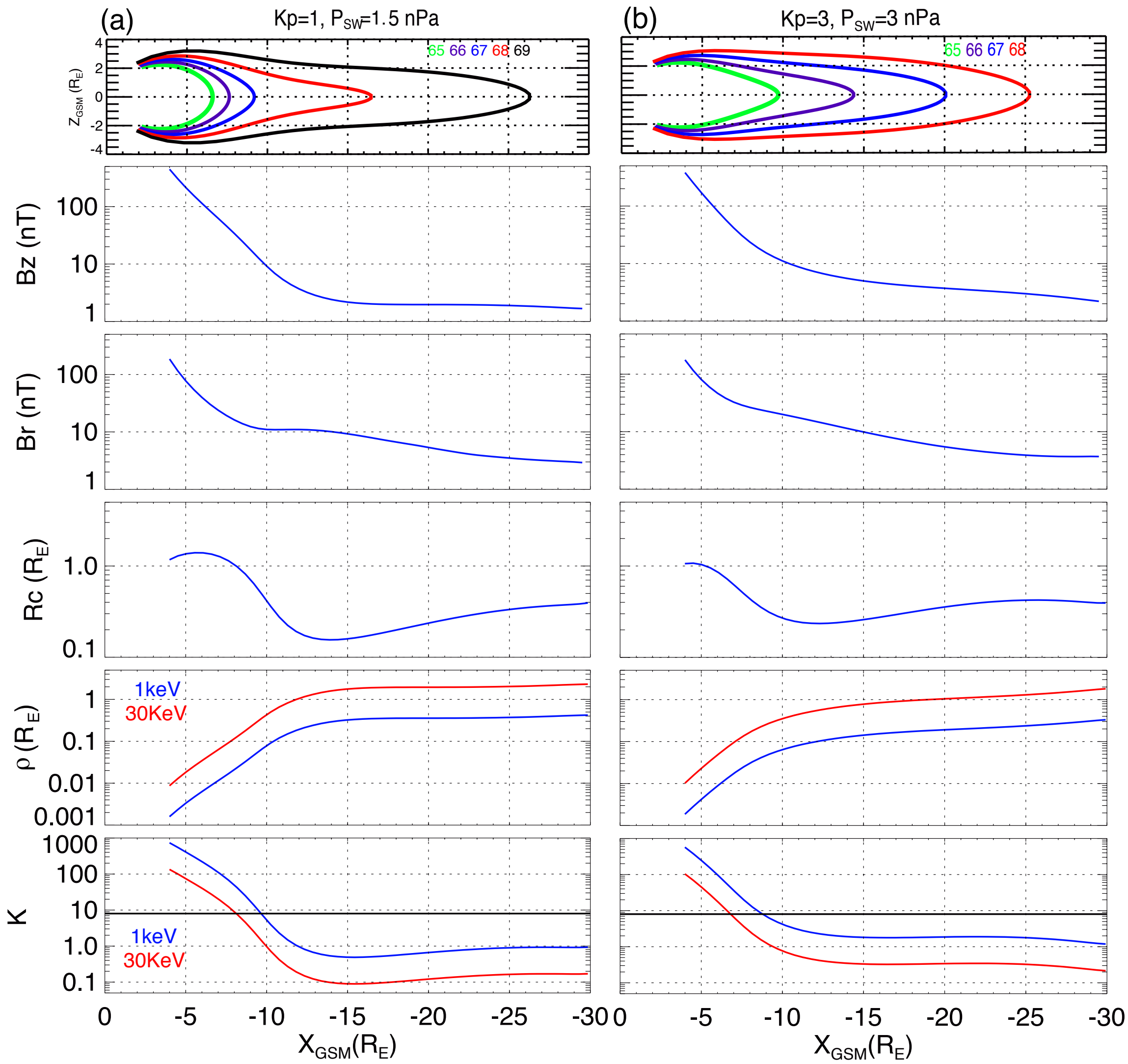

Figure 4.1. Midnight radial profiles of the key parameters of IB calculation for (a) Kp = 1 and P_{SW} = 1.5 nPa and (b) Kp = 3 and P_{SW} = 3 nPa cases. The first panel shows the magnetic field lines of different ionospheric latitudes; the second panel shows Bz at Z = 0; the third panel shows Br at Z = 0.5 R_E; the fourth panel shows the equatorial magnetic field curvature; the last two panels show the equatorial gyro-radius and the TCS scattering parameter K for 1 (blue curve) and 30 (red curve) keV protons.

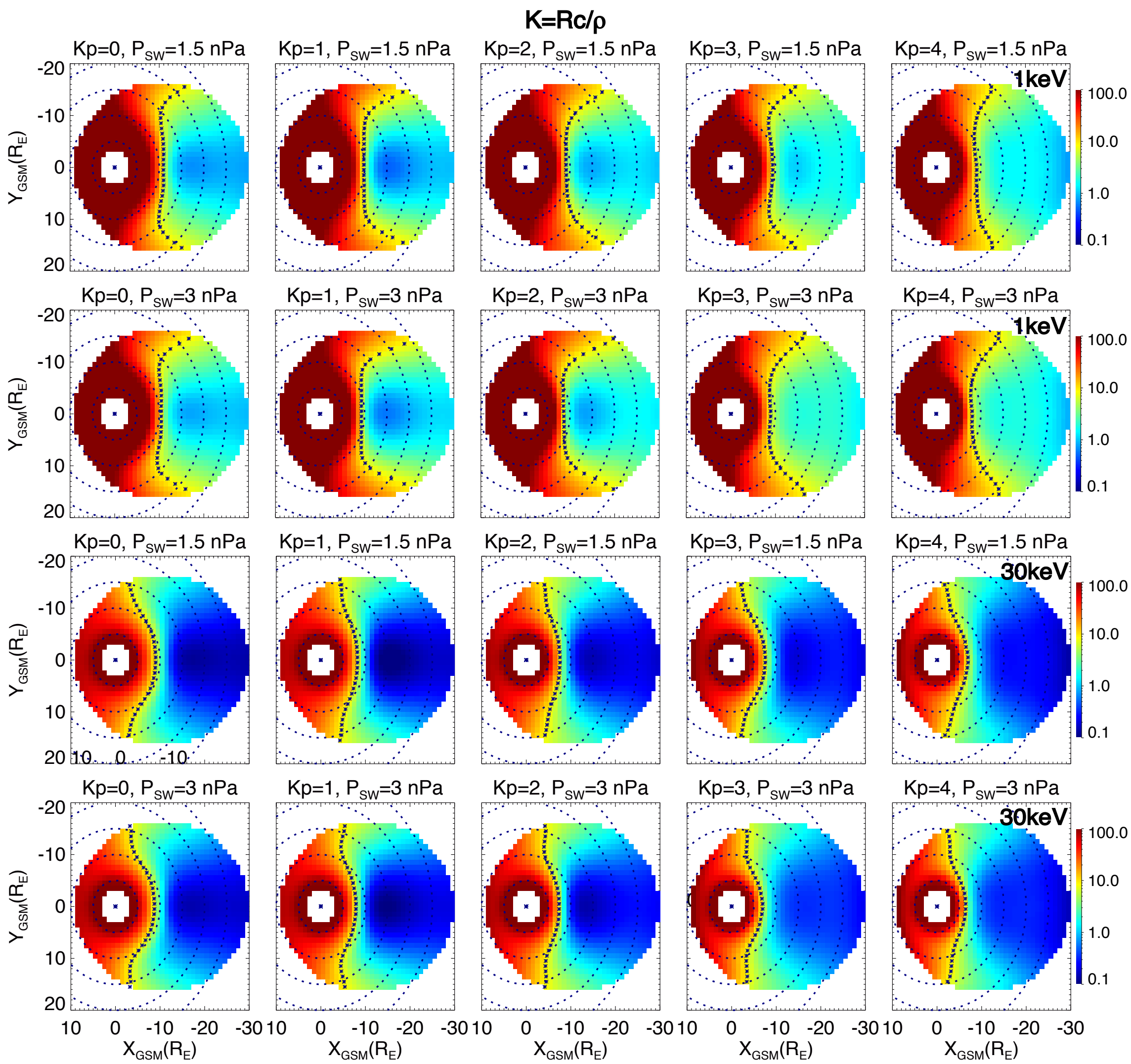

Figure 4.2. The TCS scattering parameter K for 1 and 30 keV protons on the equatorial plane for different Kp and P_{SW} levels. The black stars mark K = 8.

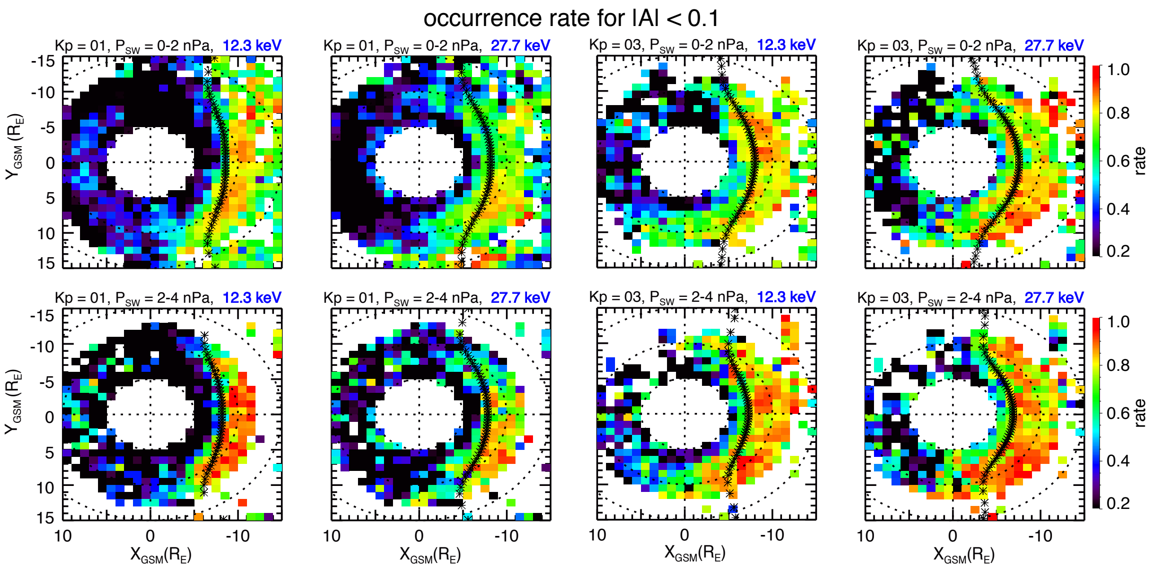

Figure 4.3. The occurrence rates for highly isotropic protons of 12.3 and 27.7 keV observed by THEMIS for different Kp and P_{SW} levels. The Black stars mark the modeled IB for the two proton energies.

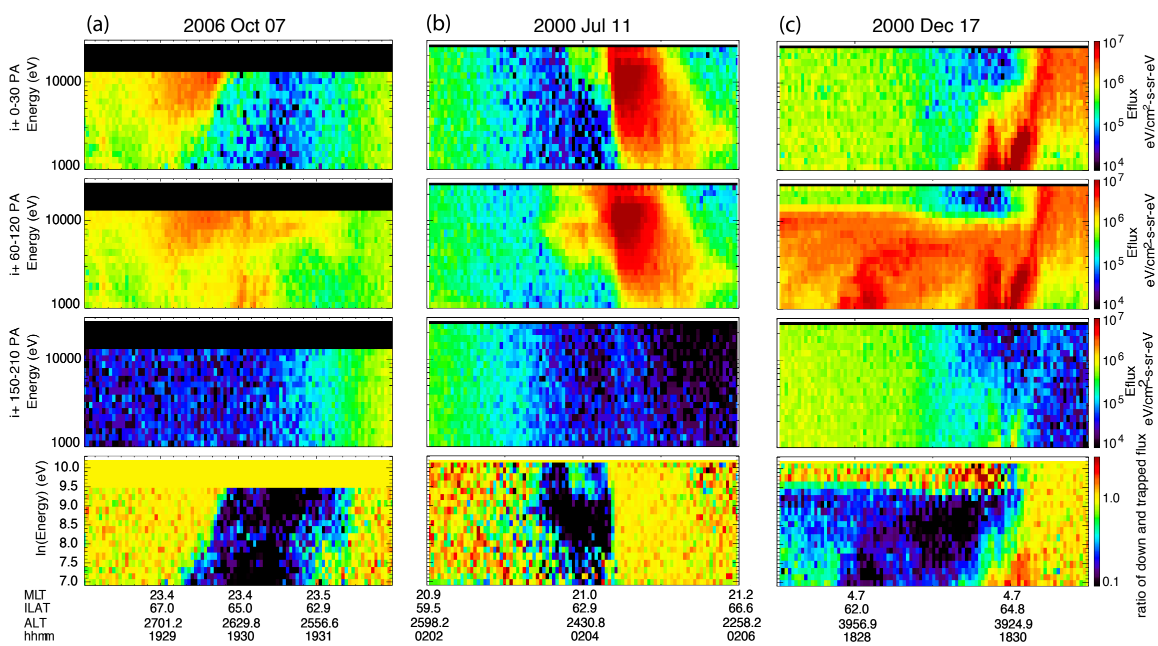

Figure 4.4. The ion energy fluxes measured by FAST within three different pitch-angle ranges and the ratio of precipitating and trapped ion flux of ion from 1 to 30 keV ions (note that the Y

axis for the ratio plots is *ln*(E) for better showing the energy dependence) for three events: (a) Oct. 7, 2006; (b) Jul. 11, 2000; (c) Dec. 17, 2000. The X axis shows magnetic local time (MLT); invariant latitude (ILAT) and the altitude (ALT) of FAST satellite and the universal time.

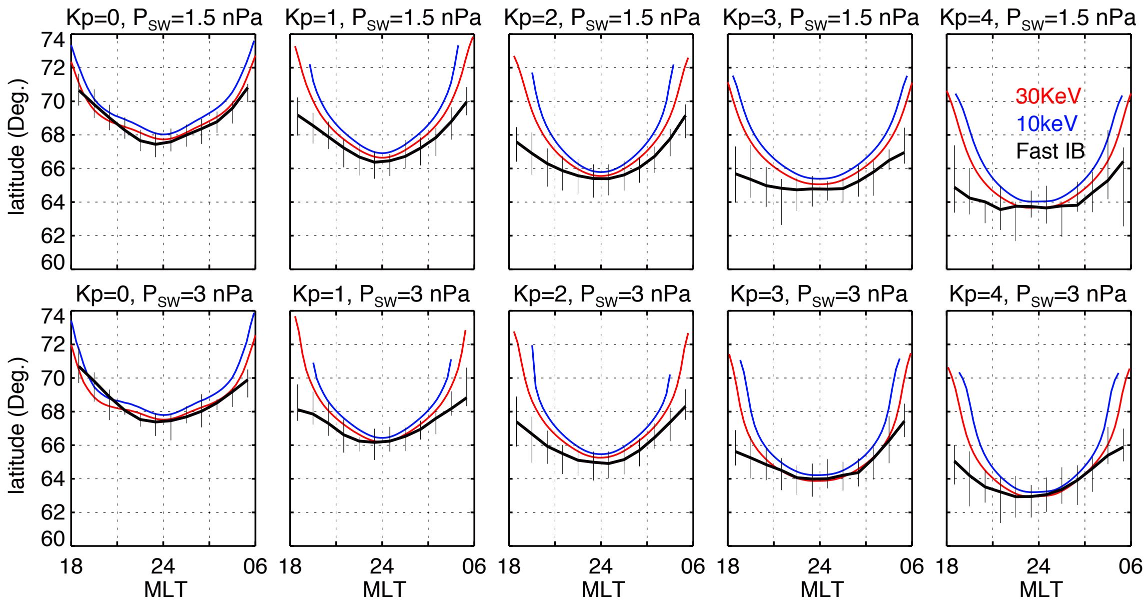

Figure 4.5. The IB invariant latitudes observed by FAST (the black curves indicate the median and the black vertical lines indicate the 25% and 75% quartiles) as a function of MLT for different Kp and P_{SW} levels. The modeled IB latitudes in the ionosphere for 10 (the blue lines) and 30 (the red lines) keV protons.

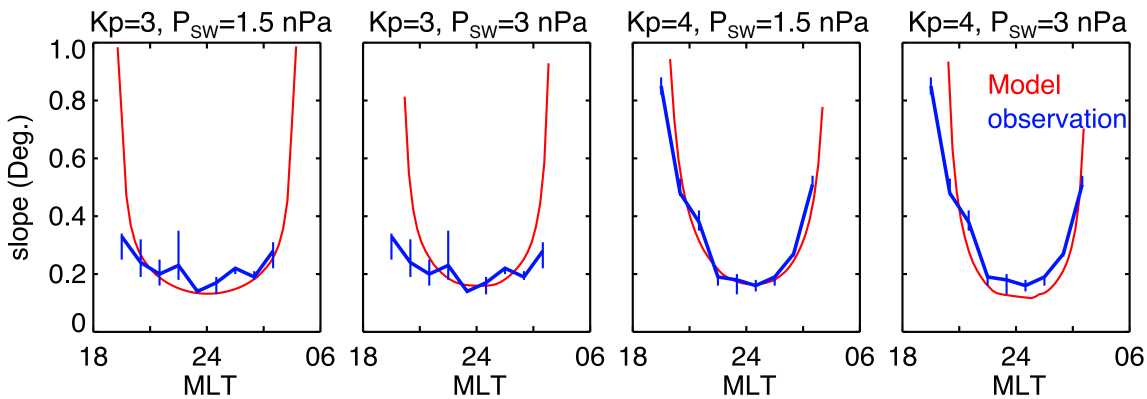

Figure 4.6. The slope comparison between the modeled (the red curves) and FAST IB (the blue curves) for Kp = 3 and 4 as a function of MLT. The FAST results are sorted only with Kp so the two blue curves for different P_{SW} under the same Kp are identical.

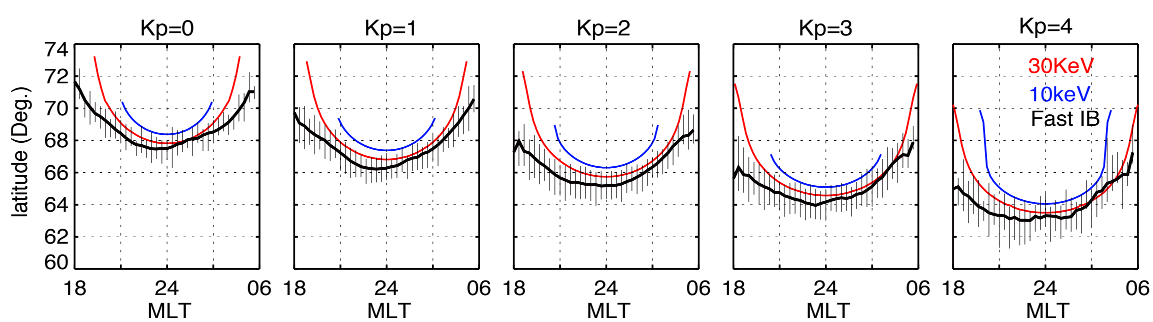

Figure 4.7. The MLT distribution of the IB latitudes for 10 (the blue lines) and 30 (the red lines) keV protons in the ionosphere computed from the T89 model in comparison with the FAST IB (the black curves) for different Kp levels.

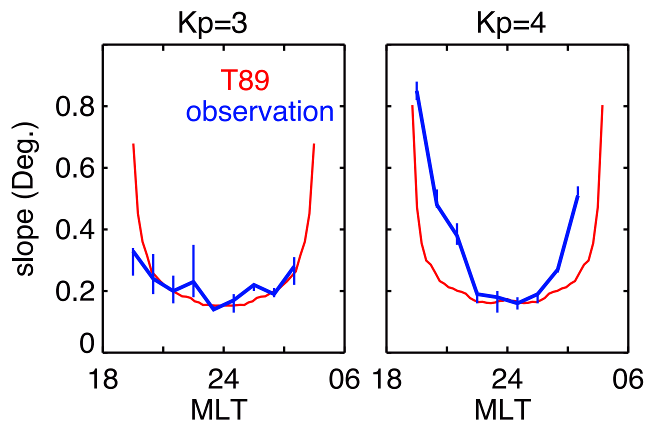

Figure 4.8. Comparison of the slopes between the IB computed from the T89 model (the red curves) and that from FAST observation (the blue curves) for Kp = 3 and 4 as a function of MLT.

CHAPTER 5 | The Evolution of Plasma Pressure, Magnetic Field, and Current Structures during Substorm Growth Phase

In this study, we first establish a realistic 3D substorm growth phase magnetic field model (adopted from *Zaharia* [2008]) that satisfies the physical constraint of force balance with plasma sheet pressures predicted by the SVRM plasma sheet pressure model we developed in Chapter 2. Here, we first investigate the evolution of 3D plasma sheet pressure distributions and magnetic field configurations, as well as the current system, during the substorm growth phase, and then evaluate my model accuracy by comparing model results with observations within the plasma sheet. And we also briefly discuss plasma pressure and magnetic field responses to different P_{SW} and sunspot number. By applying our magnetic field model to a substorm event, we evaluate the dynamics of proton aurora due to current sheet scattering by comparing the magnetospheric ion isotropic boundaries (IBs) with proton auroral observations [e.g., *Ganushkina et al.* 2005; *Shevchenko et al.* 2010; *Yue et al.* 2014], examine ballooning stability of the plasma sheet configurations, and determine the onset location in the plasma sheet by mapping the ionospheric onset location.

5.1 Model result: Evolution of Substorm Growth Phase—Energy Loading Effect

In this section, we examine the growth phase evolution of pressure, magnetic field and current density profile in the equatorial plane and along the midnight meridian corresponding to increasing PCPAE loading under constant P_{SW} and sunspot number to demonstrate whether our physical based self-consistent model can qualitatively reproduce the typical signatures of a substorm growth phase. In the next session, we evaluate quantitatively the accuracy of our model substorm growth evolution by comparing with observations.

Figure 5.1 shows the equatorial plasma pressure, magnetic field and westward currents for 5 different energy loading values (100, 2000, 4000, 8000, 10000 kV · min) with $P_{SW} = 2$ nPa and sunspot number = 50. These loading values are chosen to represent the increasing loading typically seen for a strong substorm (AE max > 600 nT, see *Yue et al*. [2015]), with PCPAE = 100 corresponding to the beginning of the growth phase and 10000 to just before substorm onset. Figure 5.1a shows that the plasma pressure gradually increases as energy loading increases with no significant dawn-dusk asymmetry, while Bz gradually increases in the magnetotail with smaller value at midnight than near the flanks and the westward current (J_φ) gradually increases and peaks around midnight. Along the midnight meridian as shown in Figure 5.1b, the plasma pressure and its gradient increase, while magnetic flux tube volume decreases, as energy loading increases. Bz increases in the tail but decreases in the inner magnetosphere due to the increasing J_φ which peaks at small r as energy loading increases, showing Earthward plasma sheet penetration. While plasma beta shows a peak forming during the late growth phase around 11 R_E. The flat Bz profile within the high-β plasma sheet during the late growth phase could be the favorable condition for plasma sheet instabilities, such as ballooning/interchange instabilities, which may initiate substorm onset. This is further discussed in section 5.5.

Figure 5.2 shows the model results in the midnight meridian plane and the variations with Z at X = –8 and –13 R_E. It is shown that plasma pressure increases as energy loading increases along the midnight meridian in Figure 5.2a, resulting in the field lines from 3 fixed latitudes (65 ^{o}, 66 ^{o}, and 67 ^{o}) become more stretched and map to further down the tail. Bz shows a positive gradient in the Z direction (dBz/dZ > 0) in the vicinity of X= –10 R_E and the area of positive dBz/dZ becomes larger as energy loading increases. In addition, the westward J_φ increases as energy loading increases and its contour is aligned approximately with field lines, which is a feature resulting from force balance that other empirical models do not take into account.

Along the Z direction shown in Figure 5.2b, plasma pressure and Bxy increase as energy loading increases while Bz decreases at the equator but increases off the equator during the late growth phase, showing positive dBz/dz (as seen by the green and red curves in the third column in Figure 5.2b) at both locations (X = –8 and –13 R_E). It is interesting to note that the positive dBz/dz signature has been observed by THEMIS [*Saito et al.,* 2010, 2011]. However, a corresponding local equatorial Bz minimum as a function of radial distance predicted by *Saito et al.* is not seen in our model results. Additionally, J_φ peaks off the equatorial plane in the near Earth region, and the Z locations of the peak moves towards the equatorial plane as energy loading increases, indicating that the current sheet is thinning as the growth phase develops.

5.2 Model Evaluation

The model results above show the typical picture of plasma sheet dynamics during the substorm growth phase: plasma pressure increases, magnetic field lines become more stretched, and westward current is enhanced, and current sheet thins. To evaluate quantitatively how reliable our model results are, we compare the model Bz on the equatorial plane and total magnetic field strength along the Z direction with the observed magnetic fields from Geotail and THEMIS for PCPAE loading = 100, 2000, 4000, 8000 kV·min with P_{SW} = 2nPa and sunspot number = 50 in Figures 5.3 and 5.4. Figures 5.3a and 5.3b show comparisons between the median values of observed Bz near the equatorial plane (beta > 2) and the modeled Bz at Z = 0 from the force-balanced magnetic field. The observed Bz in the plasma sheet is relatively lower at midnight than near the flanks, and the overall Bz in the plasma sheet increases with increasing PCPAE loading. The model Bz reproduces reasonably well the spatial distributions and their overall response to PCPAE loading, though statistics for PCPAE = 8000 are more limited than for the lower PCPAE values. Figure 5.3c shows that the model Bz (red lines) in the plasma sheet agrees generally well with observed Bz (blue lines with the errors bar indicating the 25% and 75% quartiles), The modeled Bz has lower magnitudes than the observations from ~9 to 13 R_E, a difference that could be due to the model Bz being evaluated strictly at Z = 0 while the observations include data points in the vicinity of the equator plane. As shown in Figure 5.2, Bz at |Z| < ~1 R_E actually becomes higher as Z increases at r ~8 to 13 R_E, thus likely leading to higher Bz values than would be obtained if we were able to obtain observations strictly at the equator.

To evaluate the model magnetic field variations along the Z direction, we plot in Figure 5.4 the total model magnetic field strengths as a function of plasma beta (red curves) in comparison with the median values of observed strengths (blue lines with the errors bar indicating the 25% and 75% quartiles) at 3 different radial distances (r = 8, 11 and 16 R_E). Plasma beta is used to represent Z variations since the exact Z distances to the equatorial plane cannot be determined for the observations and plasma beta decreases with increasing Z. Figure 5.4 shows that the observed total magnetic field strength increases with increasing energy loading, and the model agrees very well with the observed magnitudes as well as their variations with beta and responses to energy loading.

5.3 Discussion

5.3.1 Field-aligned currents

Figure 5.5a shows the equatorial mapping of integrated FACs density $J_{||}$ in the ionosphere computed using the Vasyliunas equation [*Vasyliunas*, 1970, 1984] for 5 different energy loadings with $P_{SW} = 2$ nPa and sunspot number = 50. At the beginning of growth phase, there are typical R1 FACs in the tail with upward (downward) FACs at the pre-midnight (post-midnight) MLTs. There is a small upward R2 FAC in the post-midnight close to the Earth. As the energy loading increases, the R2 FACs intensify and move earthward, while the R1 FACs retreat tailward. This is due to the magnetic field topology changes and increasing pressure gradients. At late growth phase, the typical R2 FACs develop with downward (upward) FACs at pre-midnight (post-midnight) MLTs and the R1 FACs disappear from the model domain.

To evaluate our FACs, we compare with the FACs derived from AMPERE (details about how to derive the FACs from AMPERE can be found in *Murphy et al.* [2012]). Since a statistical pattern of AMPERE FACs for the substorm growth phase has not been established, we did an initial check using a substorm event on March 7th 2010 (onset time is 05:17 UT), which has very good spatial coverage of magnetic field data for deriving FACs from AMPERE. To model FACs for this event, we first obtained the 2D equatorial pressure profile for different times of the growth phase from our 2D empirical plasma sheet pressure model by using the observed temporal profiles of P_{SW} and PCPAE loading as input (the monthly averaged sunspot number was 15.3). We then computed the force-balanced magnetic field and associated FACs.

Figures 5.5b and 5.5c show comparisons between the AMPERE FACs (the red and blue colors indicate downward and upward FACs into and from the ionosphere, respectively) during

04:34-04:44 and 04:48-04:58 UT and model FACs at 04:38 and 04:53 UT. The gray color in Figure 5.5b indicates the very weak FACs (less than 0.1 $\mu A/m^2$). It can be seen that during 04:34 – 04:44 UT, there are observed upward FACs at high latitudes (~ 68° –70°) in the pre-midnight sector and a pair of Region-2 sense FACs with downward (upward) FACs at pre-midnight (post-midnight) at low latitudes (~64° –66°). The observed FACs intensify (04:48 – 04:58 UT) as the substorm growth phase develops, showing typical Region-1 sense FACs at the high latitudes (~ 67° –70°) and Region 2 sense FACs at the low latitudes (~63° –66°). The model FAC patterns match reasonably well with the observations despite some discrepancies in the latitude and magnitude. Comparing Figure 5.5b and 5.5c shows that the observed FACs spreads more broadly over latitude than do the model FACs. The larger spread of the observed FACs may be due to the 10-min averaging interval of the data, during which the magnetic field stretches causing the ionospheric latitudes of the FACs to change. In addition, the 20 second resolution of the AMPERE magnetometers and subsequent ten minute gridding will tend to smooth the AMPERE FACs. This smoothing of the AMPERE FACs along with the higher spatial and temporal resolution with which the model FACs are computed, such that spatially and temporally localized currents can be resolved, will contribute to the amplitude differences between the modeled and derived AMPERE FACs.

5.3.2 Effect of P_{SW} and sun spot number

While the evolution of the growth phase pressure and magnetic field mainly respond to the increasing PCPAE loading, the responses also depend on P_{SW} and sunspot number, which can be quite different for each substorm. Here we briefly describe the dependences on these two factors. Figures 5.6 and 5.7 show the model results in the equatorial plane and along the midnight meridian, respectively, corresponding to the same PCPAE loading (4000 kV·min) but to different values of P_{SW} (2 and 4 nPa) and sunspot number (20 and 50) as labeled on top of each column. From Figure 5.6a, when the sunspot number is higher, the plasma pressure is higher in the inner magnetosphere but becomes lower in the tail, resulting in stronger pressure gradient, enhanced westward current, and substantial increase of Bz in the tail. Note that the dependence on sunspot number is not linear. Pressure increases with increasing sunspot number until ~60-80 then decreases again (see Chapter 2 for possible explanation of the non-linear dependence). As P_{SW} increases, the plasma pressure and pressure gradient increase and magnetic field Bz decreases in the near Earth region, but increases in the tail due to the increasing westward current J_{φ}, and the J_{φ} peak moving earthward. The response to P_{SW} may be a result of the balance between P_{SW} and magnetosphere pressure (magnetic pressure in the lobes and plasma pressure in the equatorial plane) as discussed in Chapter 2 and 3.

As shown in Figure 5.7, while the magnitudes of pressure, magnetic fields, and current density changes with changing P_{SW} and sunspot number, the X-Z profiles of these parameters remain similar. The magnetic field configurations are slightly more stretched when sunspot number changes from 20 to 50, but are significantly more stretched when P_{SW} increases from 2 to 4 nPa as indicated by the field lines for the 3 fixed latitudes (65^{o}, 66^{o}, and 67^{o}).

5.4 Model Application: a substorm event study

Since the evaluation shown above indicates that our model give a good statistical description of the substorm growth phase, we thus applied the model to a substorm event to analyze the physical processes associated with the evolution of the plasma and magnetic field, including the evolution of proton aurora due to current sheet scattering, ballooning instability, and the substorm onset location in the plasma sheet. Here we show an example of our analysis of a substorm event on March 5th, 2008. As can be seen from the aurora observed by 630.0 and 486.1 nm wavelength of the NORSTAR meridian scanning photometers at Gillam station (located at ~23.4 MLT at the onset) shown in Figures 5.8a and 5.8b, both the electron and proton aurora moved equatorward during the growth phase and the electron aurora breakup started at 67.3^{o} latitude at 06:04 UT followed by poleward expansion of aurora. The electron aurora breakup arc is located at the poleward shoulder of the proton aurora, as is typically observed [*Donovan et al.*, 2012]. As shown in Figure 5.8b, this event is chosen for having good spatial coverage of the nightside plasma sheet by two geosynchronous satellites (GOES-10 and GOES-12) very near midnight and three THEMIS satellites radially aligned (TH-A, TH-D, and TH-C at X_{GSM} ~6, 11, and 16 R_E, respectively) at Y_{GSM} ~5 R_E, thus providing excellent coverage for evaluation of our model predictions. Figures 5.8d-f show that during the growth phase P_{SW} varied slightly between 1.7 and 2 nPa, PCP gradually decreased from 70 to 50 kV, and AE slowly increased from 40 to ~100 nT. The AE during the growth phase was small and then reached ~400 nT after the onset (not shown), indicating that this is an isolated and moderate substorm. The computed PCPAE loading, shown in Figure 8g, increased from ~50 to 5000 kV-min.

Using the observed P_{SW} and PCPAE loading shown in Figures 5.8d and 5.8g and the observed monthly averaged sunspot number of 9.3 for this event, we predict the evolution of the plasma sheet pressure and magnetic field. Figure 5.9 shows the comparisons between modeled results and observations. The black and blue lines in Figure 5.9a are plasma and total pressures observed by THEMIS, respectively, and the red lines are the model equatorial pressures. As shown in Figure 5.8c, TH-A moved tailward in the inner magnetosphere from around r ~ 6 R_E, and remained close to the central plasma sheet since the total pressure is similar to the plasma pressure throughout the growth phase in Figure 5.9a. TH-D was at r ~11 R_E while TH-C was at r ~16 R_E and both were moving eastward and also moving away from the central plasma sheet as indicated by the plasma pressure becoming smaller than the total pressure. This is likely due to the magnetic field becoming more stretched and the plasma sheet becoming thinner as the growth phase develops. The model pressures match reasonably well with observed total pressure in general, except for TH-D just prior to the onset, when TH-D became far away from the current sheet where the pressure model prediction becomes less reliable.

In order to evaluate how reliable our modeled magnetic field is for this specific event, Figure 5.9b compares the model magnetic field Bz component and radial component Br ($B_r = \sqrt{B_x^2 + B_y^2}$) with the observations from GOES-12 and GOES-10, as well as with TH-D and TH-C, during the substorm growth phase from 05:10 to 06:00 UT. Here, we have used the GOES satellites observed magnetic field instead of TH-A because GOES-10 and GOES-12 observed larger Bz than TH-A, indicating that the GOES satellites were likely closer to the central plasma sheet than TH-A. Since we do not know exactly the satellite positions relative to the current sheet, we use the model Br and Bz at the satellite Z_{GSM} (for GOES) and the observed plasma beta (for THEMIS). Because of this uncertainty in the real Z distance to the current sheet, we emphasize comparison of the variation trends instead of the exact values. The Br and Bz comparisons at the different radial locations show that the model magnetic field variations are consistent with observed magnetic field variations.

Previous studies have shown that the proton aurora can be used as an excellent indicator for remote sensing certain aspects of magnetotail dynamics [*Donovan et al*., 2012], and also for testing magnetosphere-ionosphere mapping accuracy [*Ganushkina et al.* 2005; *Shevchenko et al*., 2010] since the equtorward boundary of the proton aurora is expected to overlap with the IBs of keV ions due to current sheet scattering under low geomagnetic activity [e.g., *Sergeev et al.,* 2012; *Yue et al.,* 2014]. The low geomagnetic activity during the substorm growth phase of this event (AE is smaller than ~100 nT) gives us an excellent opportunity to analyze magnetic field topology change through proton aurora dynamics. Comparing the latitudes of the IBs computed from our model magnetic field with the latitudes of the proton aurora shown in Figure 5.8b allows us to evaluate the mapping and also to understand the equatorward motion of the proton aurora during the growth phase.

Figure 5.10 shows the computed IBs and their comparisons with the proton aurora. Figure 5.10a and 5.10b show the IBs (solid lines) for 10 keV protons at six different times (indicated by different colors) in the equatorial plane and the corresponding latitudes in the ionosphere, respectively. These IBs are calculated from the model 3D force-balanced magnetic field configurations based on the current sheet scattering criterion (the ratio between the magnetic field curvature radius and the particle gyro-radius is less than 8) [*Sergeev et al.,* 1983]. To give a better picture of the mapping under such magnetic field configurations, we also plot in Figures 5.10a and 5.10b the equatorial locations that are 5 (dotted lines) and 10 R_E (dashed lines) tailward of the IBs along the X direction and their corresponding ionospheric latitudes, respectively. It can be seen that the IBs are very close to each other on the equatorial plane, with ~0.5 R_E Earthward movement near midnight while the IBs in the ionosphere move ~1° equatorward near midnight due to the continuous stretching of magnetic field lines from 05:10 UT to 06:00 UT. It should be note that our model is not yet able to take into account dipole tilt. However, we have estimated the uncertainty of mapping using the T01 model. The mapping latitude of a point at X = –9 and Y = 0 R_E (approximately the IB locations) at 05:10 UT is

~67.23° when assuming no dipole tilt (current sheet is at $Z = 0$) and is ~67.84° when considering dipole tilt (current sheet is at $Z = -0.8\ R_E$). This latitude difference is roughly the same throughout the growth phase. So for this event, there is likely a 0.6° uncertainty in latitudes due to the dipole tilt effect. This uncertainty shouldn't affect our results significantly.

It is expected that the earthward edge of the IBs for keV ions should correspond to the equatorward boundary of proton aurora. In Figure 5.10c, we overplot the evolution of the computed IBs on the proton aurora observed by the 486.1 nm meridian scanning photometer at Gillam station. The blue line is the IB evolution for 10 keV proton while the red lines above and bellow the blue line give the IBs for 1 and 30 keV protons, respectively. It can be seen that the 1 to 30 keV IBs during the growth phase follow very well the equatorward boundary of the proton aurora as it moves equatorward with time. The equatorward motion of the aurora reflects two factors in the model: (1) the continuous stretching of magnetic field lines that map the equatorial IBs to lower latitudes, and (2) the movement of Gillam toward midnight where IBs are at lower latitudes than those away from midnight as can be seen in Figure 5.10b.

The good agreement between the proton aurora and IBs indicates that my model magnetic field reliably represents the realistic growth-phase magnetic configuration and its evolution with time. This also indicates that the proton aurora in this event was caused by the current sheet scattering and that the model should give realistic field line mappings from the equator to the ionosphere. As can be seen in the electron aurora shown in Figure 5.8a, the substorm onset (06:04 UT) started at ~67.3° latitude, which falls between the latitudes of the IB-$5R_E$ and IB-$10R_E$ shown in Figure 10c indicated by the two yellow lines. Therefore, it is suggested that the substorm onset location in the plasma sheet was at r ~14 R_E just before midnight from the magnetic field line mapping.

The ballooning instability during the late growth phase may play a crucial role in leading to the substorm onset. In this study, we have calculated the equivalent MHD ballooning instability growth rate for this substorm event as done in *Xing et al*. [2013]. Here, we calculated the second mode of drift ballooning instability (DBI-2) as defined in *Pu et al.* [1997], which is easier to be triggered during the substorm late growth phase when field line stretching is enhanced. The instability criterion is described by equations (5) and (6) in *Pu et al.* [1997], which are simplified as $a_0 = k_{\parallel}^2 - \beta k_p k_c < 0$ and $a_2 = 2C_{SL}^2 k_c(\frac{k_p}{\gamma} - k_c - k_b) - (C_A^2 + C_{SL}^2)k_{\parallel}^2 < 0$, where C_A is the Alfvénic velocity; $C_{SL}^2 = C_A^2 C_S^2 / (C_A^2 + C_S^2)$ with C_S being the acoustic speed; $k_p = \hat{n} \cdot \nabla P / P$, $k_b = \hat{n} \cdot \nabla B / B$ and $k_c = \hat{n} \cdot [(\hat{b} \cdot \nabla)\hat{b}]$ are the typical scale lengths of the plasma pressure gradient, magnetic field gradient, and curvature force, respectively. $k_{\parallel}$ is the parallel wave number of the perturbation, and γ is ratio of the specific heats, here assuming isothermal compression ($\gamma = 1$).

Figure 5.11a shows the midnight radial profile of plasma pressure, Bz and plasma beta for 05:10, 05:31, 05:41, 05:50 and 06:00 UT. The plasma pressure and pressure gradient increase as the substorm growth phase develops, while Bz decreases in the inner magnetosphere and increases in the tail due to the increasing J_φ. Meanwhile, the magnetic field lines become more stretched. No local Bz minimum is formed but a peak in plasma beta develops after ~05:41 UT. Figure 5.11b shows the equivalent ballooning instability growth rate parameter $a_2 \cdot a_0$ as functions of radial distance and parallel wave number for five different times along the midnight meridian and Y = 4 R_E as labeled on top of each panel under the condition that the data with both a_2 and a_0 larger than 0 are not included. By doing this, the positive value of $a_2 \cdot a_0$ indicates the plasma sheet would be MHD ballooning unstable. The range of parallel wave numbers was selected to include the value for which the equivalent growth rate becomes zero. The superposed black line identifies $a_2 \cdot a_0 = 0$, which is the threshold of instability. It can be seen that the DBI-2 mode is unstable for parallel wave numbers smaller than 3.5×10^{-6} m^{-1} during the late growth phase around midnight. This is due to the magnetic field topology change shown in Figure 5.11a producing larger FACs, which provides the favorable condition for stronger ballooning instability. In addition, the growth rate peaks around r ~13-15 R_E at midnight, which is consistent with the location of the substorm onset derived from the aurora observation in Figure 5.10.

As pointed out by *Xing et al.* [2013], the DBI-2 mode may couple to a wide range of parallel wavelength, including very large wavelength perturbations, which are related to the weak FAC in the ambient plasma. However, the ionosphere is likely to respond to the lowest possible parallel wavelength disturbances, which are associated with more intense FAC. Previous studies [e.g., *Pritchett and Coroniti*, 2010; *Zhu et al.,* 2009] have argued that the ballooning instability is more favorable when there is a Bz minimum in high plasma beta. However, in this event, no Bz minimum is associated with the increasing growth rate of DBI-2 ballooning instability. Actually, the maximum growth rate is found to be at the localized peak of plasma beta.

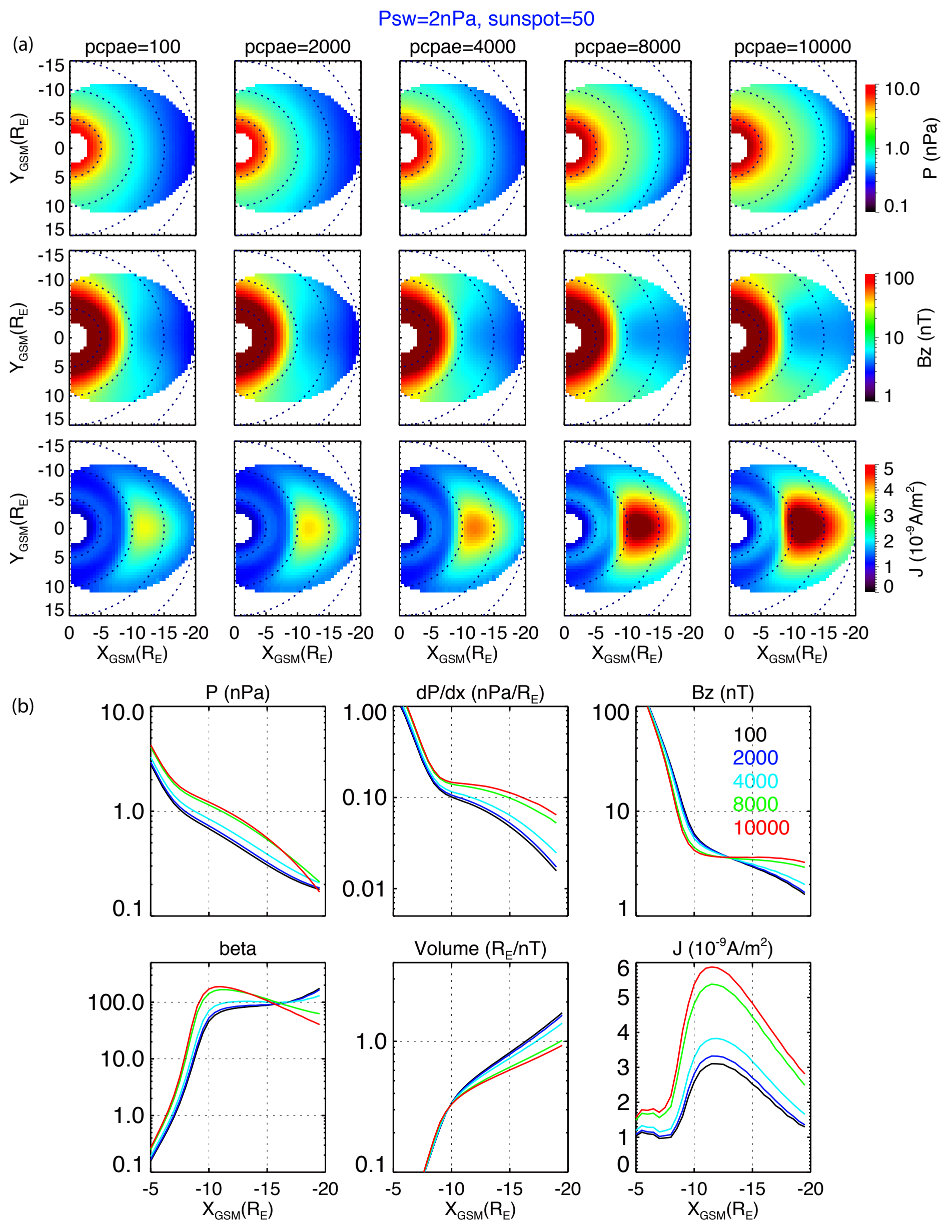

Figure 5.1. (a) The equatorial distributions of modeled pressure, Bz and westward J_φ for 5 different PCPAE loading (100, 2000, 4000, 8000, 10000 kV·min) with P_{SW} = 2 nPa, sunspot = 50. (b) The midnight radial profile of equatorial plasma pressure, plasma pressure gradient, Bz, plasma beta, flux tube volume per unit flux from the equatorial plane to the ionosphere, and westward J_φ for the same control parameters as (a). The black, blue, light blue, green and red lines are for PCPAE loading = 100, 2000, 4000, 8000, 10000, respectively.

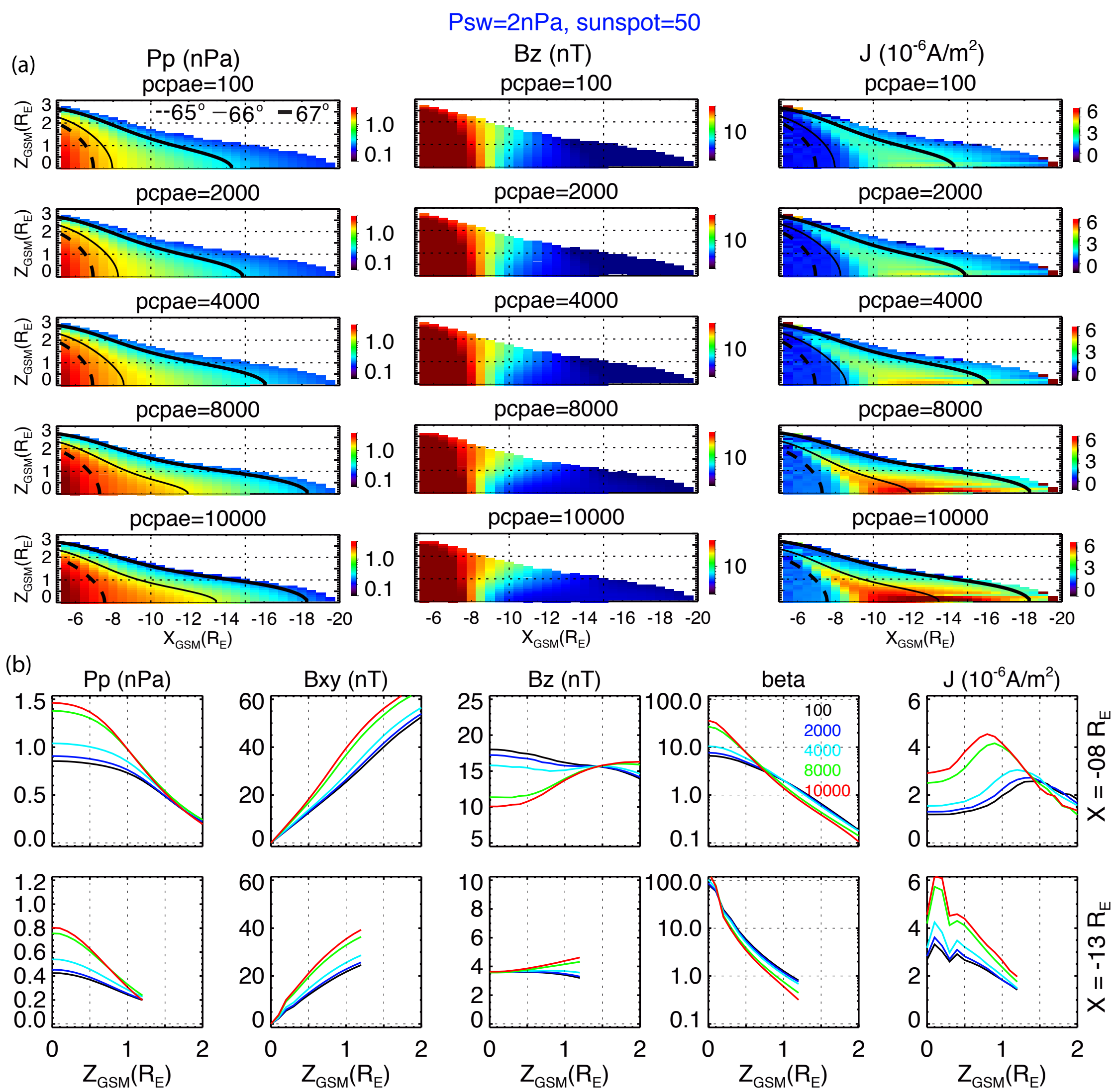

Figure 5.2. (a) The midnight X-Z plane distributions of modeled pressure, Bz and westward J_φ for 5 different PCPAE loading (100, 2000, 4000, 8000, 10000 kV·min) with P_{SW} = 2 nPa, sunspot = 50. The black curves are magnetic field lines from three different latitudes. (b) The Z radial profile of plasma pressure, Bxy, Bz, plasma beta, and westward J_φ at Y = 0 and X= –8 and -13 R_E for the same control parameters as (a). The black, blue, light blue, green and red lines are for PCPAE loading = 100, 2000, 4000, 8000, 10000, respectively.

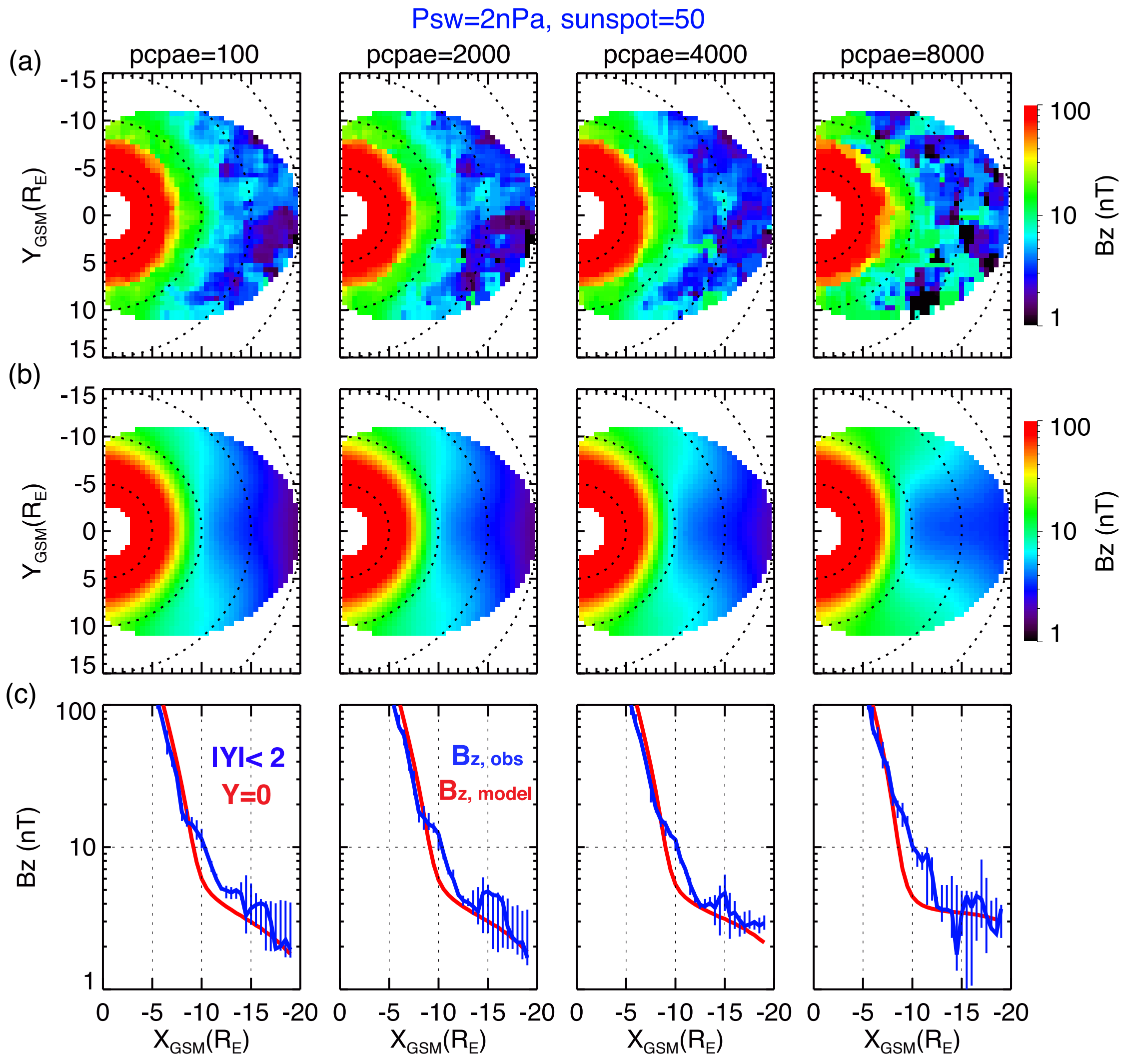

Figure 5.3. Equatorial distributions of (a) observed Bz and (b) model force-balanced Bz (c) Comparisons of the radial profiles of observed Bz (the blue curves) and the model Bz (the red curves) near the midnight MLT for 4 different PCPAE loading (100, 2000, 4000, 8000 kV·min) with P_{SW} = 2 nPa, sunspot = 50.

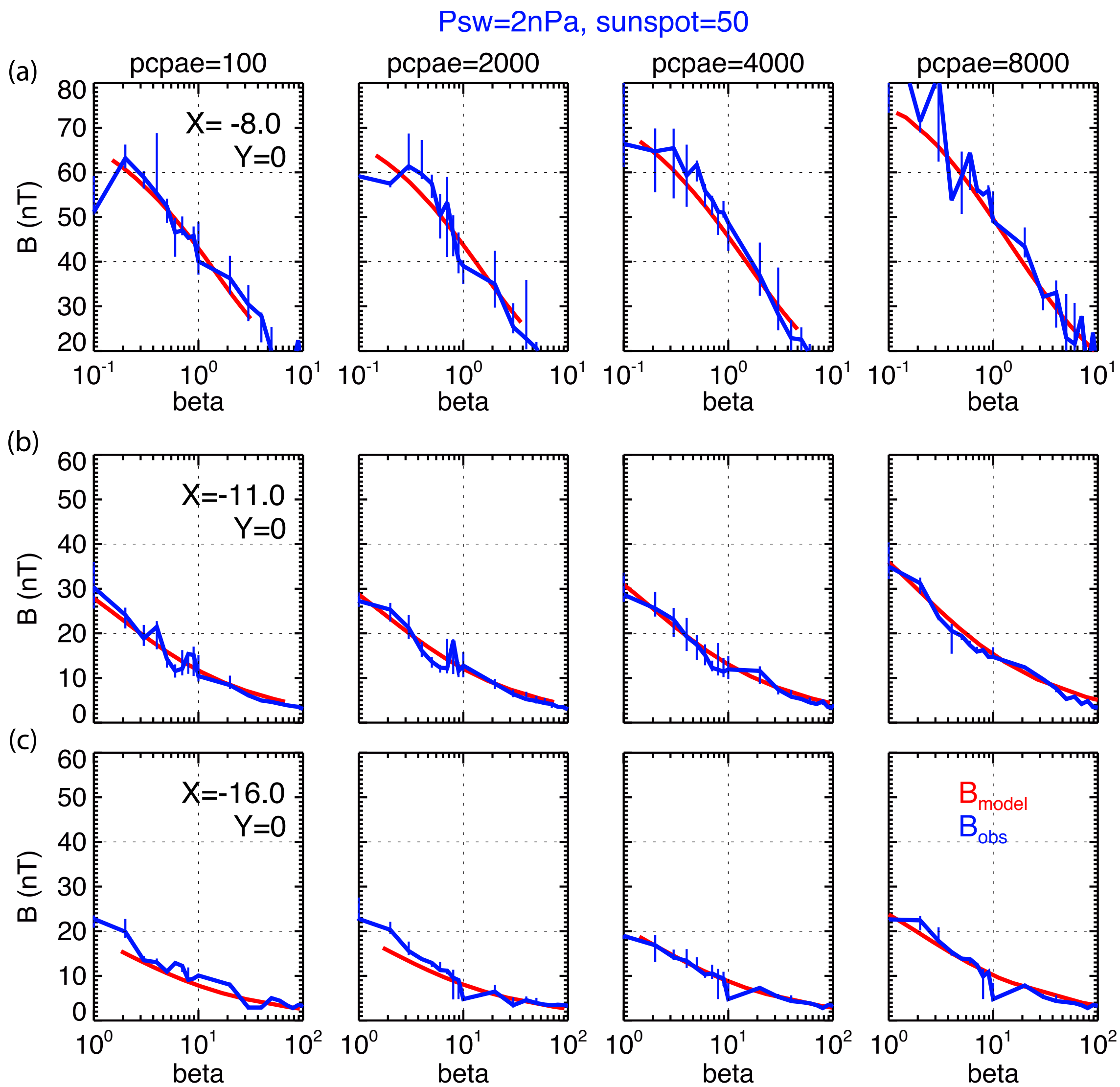

Figure 5.4. Total magnetic field as a function of plasma beta at (a) X = –8, Y = 0 R_E and (b) X = -11 and Y = 0 R_E (c) X = –16, Y = 0 R_E of the observed (the blue curves) and model magnetic field (the red curves) for 4 different PCPAE loading (100, 2000, 4000, 8000 kV·min) with P_{SW} = 2 nPa, sunspot = 50.

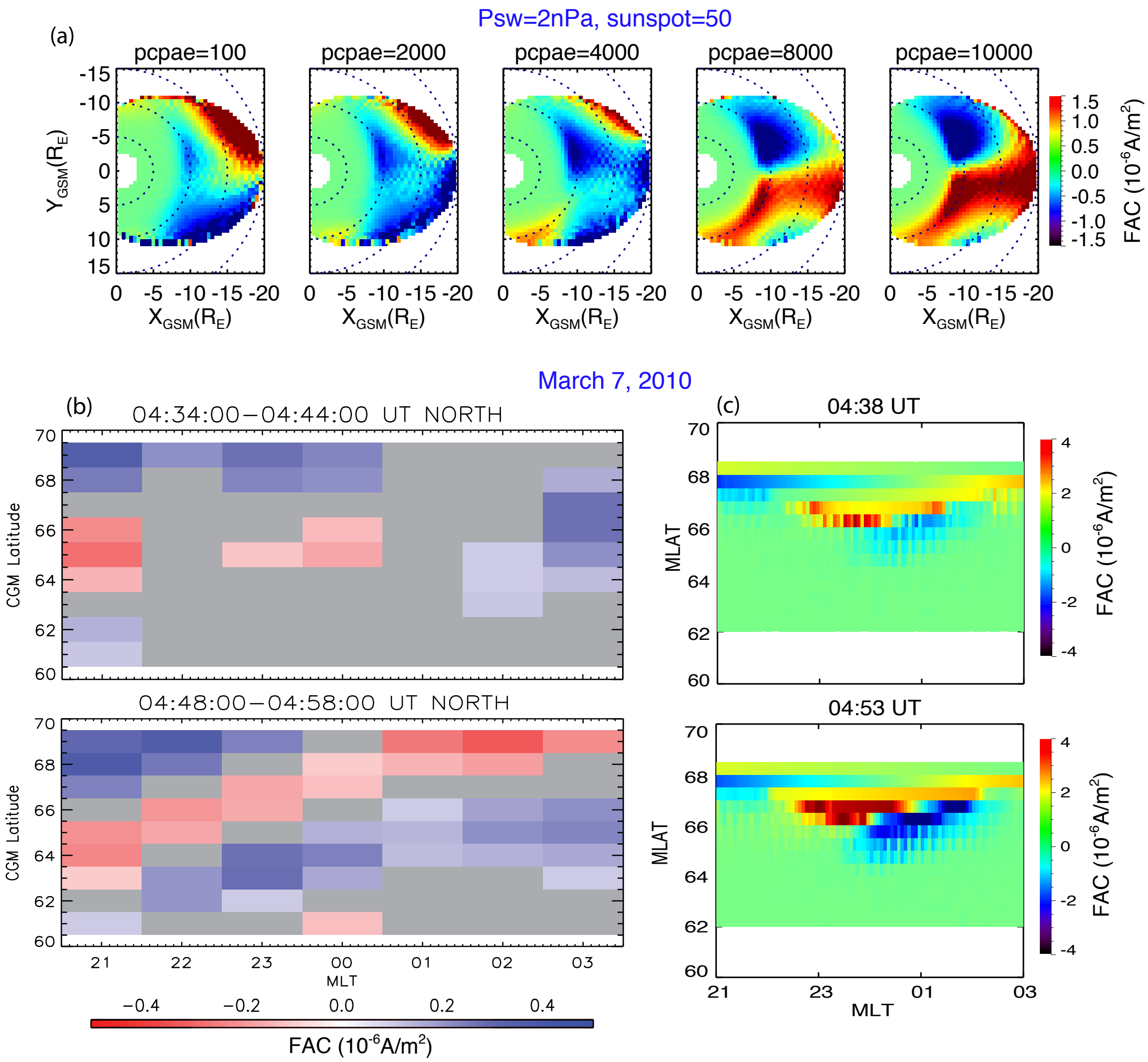

Figure 5.5. (a) The equatorial field aligned currents distributions for 5 different PCPAE loading (100, 2000, 4000, 8000, 10000 kV·min) with P_{SW} = 2 nPa, sunspot = 50. (b) The derived AMPERE FACs (red, downward and blue, upward) in ionosphere as functions of MLAT and MLT during 04:34-04:44 and 04:48-04:58 UT quasi-stationary time periods for March 7th, 2010 substorm event (onset is occurred at 05:17 UT according to auroral observations). (c) Model ionospheric FACs (red, downward and blue, upward) distributions as functions of MLAT and MLT at 04:38 and 04:53 UT.

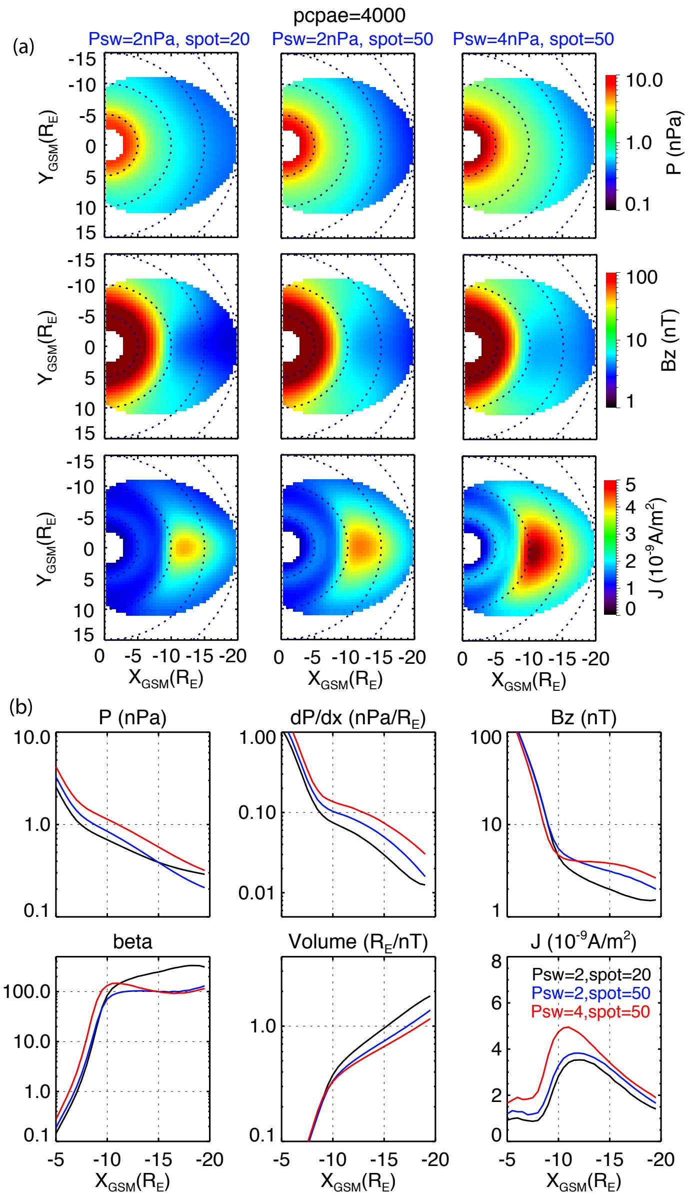

Figure 5.6. (a) The equatorial distributions of modeled pressure, Bz and westward J_φ for PCPAE loading = 4000 kV·min with 3 different control parameters (P_{SW} = 2 nPa, sunspot = 20; P_{SW} = 2 nPa, sunspot = 50; P_{SW} = 4 nPa, sunspot = 50). (b) The midnight radial profile of equatorial plasma pressure, plasma pressure gradient, Bz, plasma beta, flux tube volume per unit flux from the equatorial plane to the ionosphere, and westward J_φ for the same control parameters as (a).

The black, blue and red lines are for P_{SW} = 2 nPa, sunspot = 20; P_{SW} = 2 nPa, sunspot = 50; P_{SW} = 4 nPa, sunspot = 50, respectively.

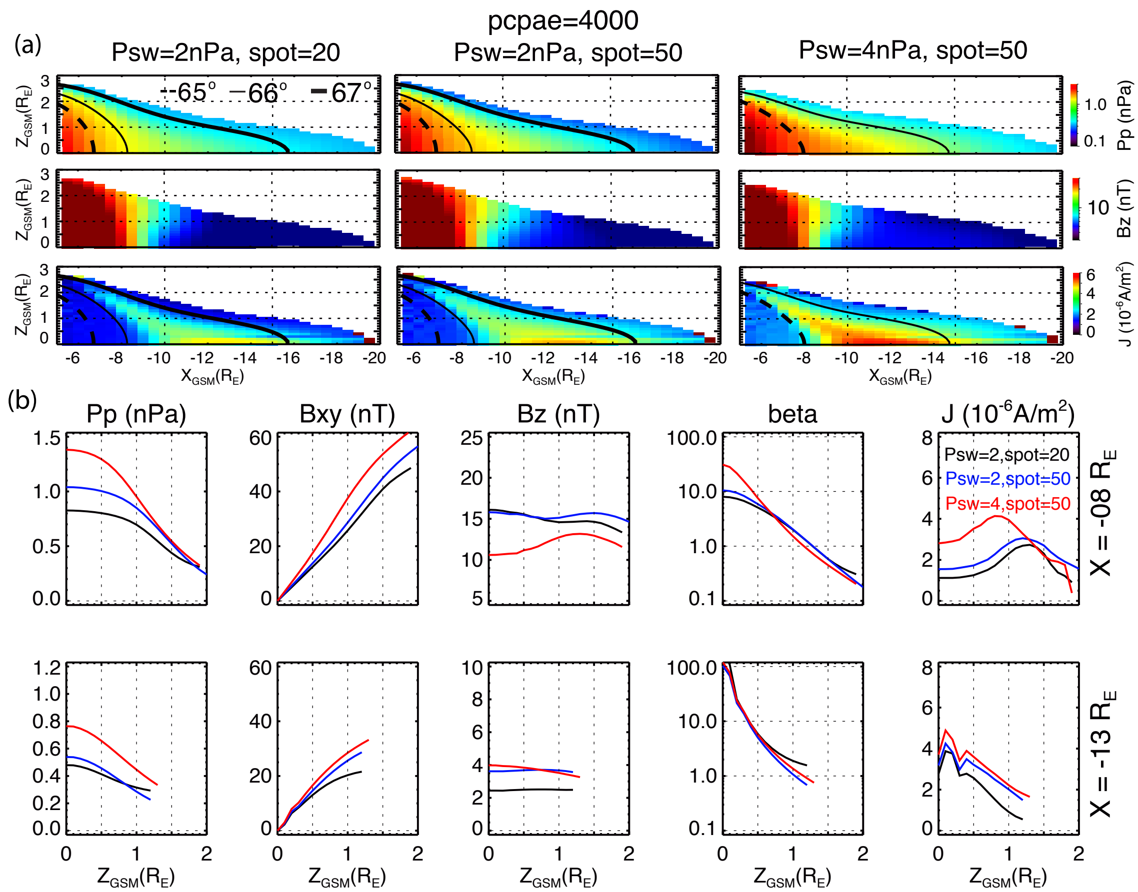

Figure 5.7. (a) The midnight X-Z plane distributions of modeled pressure, Bz and westward J_φ for PCPAE loading = 4000 kV·min with 3 different control parameters (P_{SW} = 2 nPa, sunspot = 20; P_{SW} = 2 nPa, sunspot = 50; P_{SW} = 4 nPa, sunspot = 50). The black curves are magnetic field lines from three different latitudes. (b) The Z radial profile of plasma pressure, Bxy, Bz, plasma beta, and westward J_φ at Y = 0 and X = –8 and –13 R_E for the same control parameters as (a). The black, blue and red lines are for P_{SW} = 2 nPa, sunspot = 20; P_{SW} = 2 nPa, sunspot = 50; P_{SW} = 4 nPa, sunspot=50, respectively.

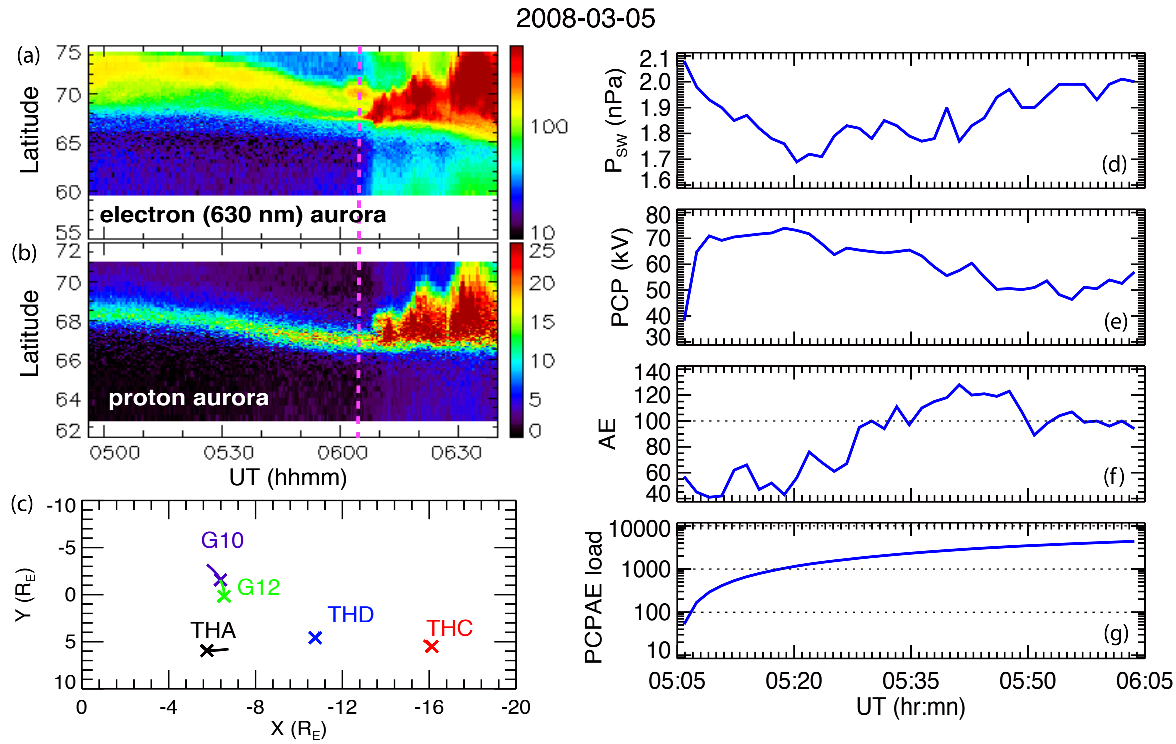

Figure 5.8. The overview of March 5th, 2008 substorm event. (a)-(b) electron and proton aurora observed by Gill station around midnight meridian. The vertical dashed line marks the substorm onset time 06:04 UT according to electron aurora observation; (c) THEMIS A, C and D and GOES10 and GOES12 trajectories at X-Y plane in GSM coordinates during substorm growth phase. The black, blue and red lines are the THEMIS A, D, C, while the purple and green lines are the GOES10 and GOES12, respectively; (d)-(g) The variation of P_{SW}, CPCP, AE and the PCPAE loading based on OMNI data during 05:05-06:05 UT.

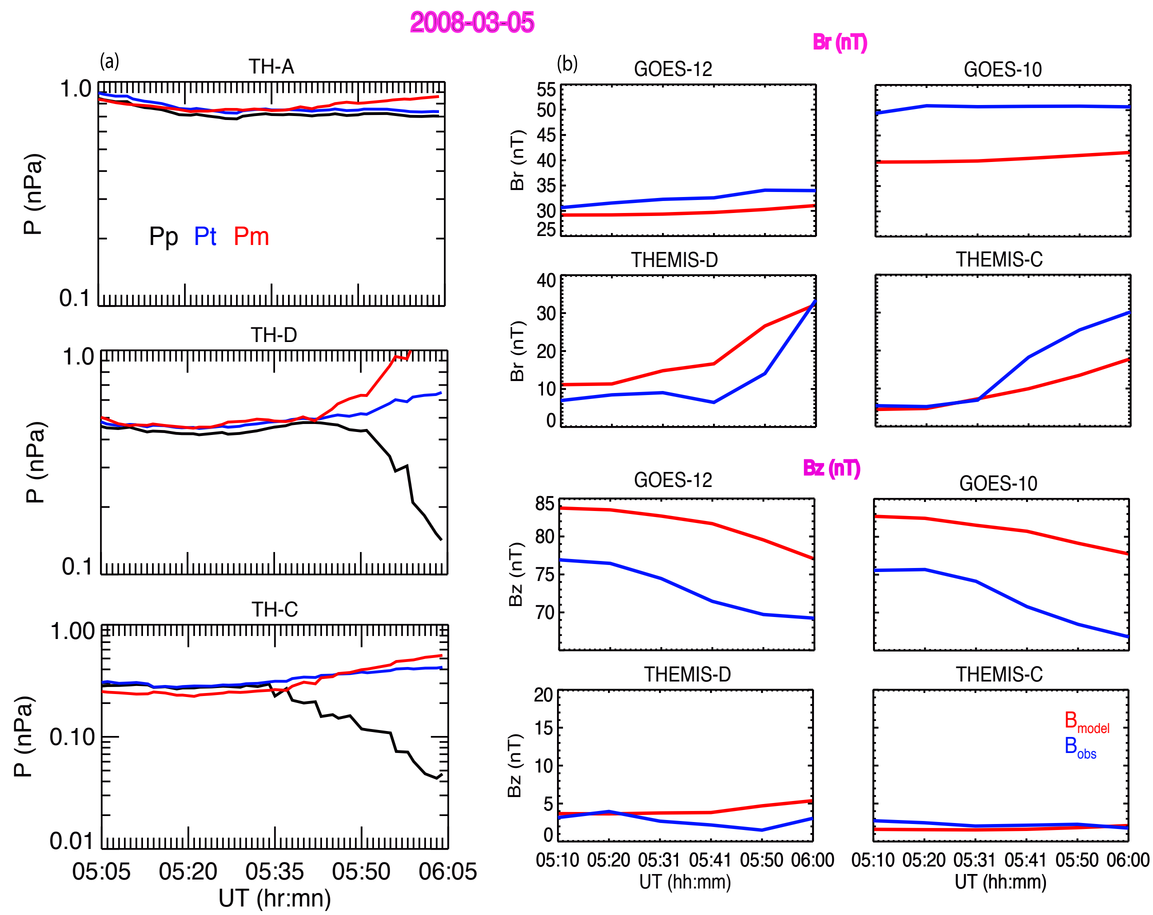

Figure 5.9. (a) The comparison of the modeled and observed pressure from THEMIS A, D and C during 05:05-06:05 UT. The black, blue and red lines are the observed plasma pressure, total pressures and the modeled pressure, respectively. (b) The magnetic field comparison for geosynchronous GOES 12 and GOES-10 as well as THEMIS D and C satellites from 05:10 to 06:00 UT. The red and blue curves are model and observation results, respectively. Upper two panels: magnetic radial Br component; lower two panels: magnetic Bz component.

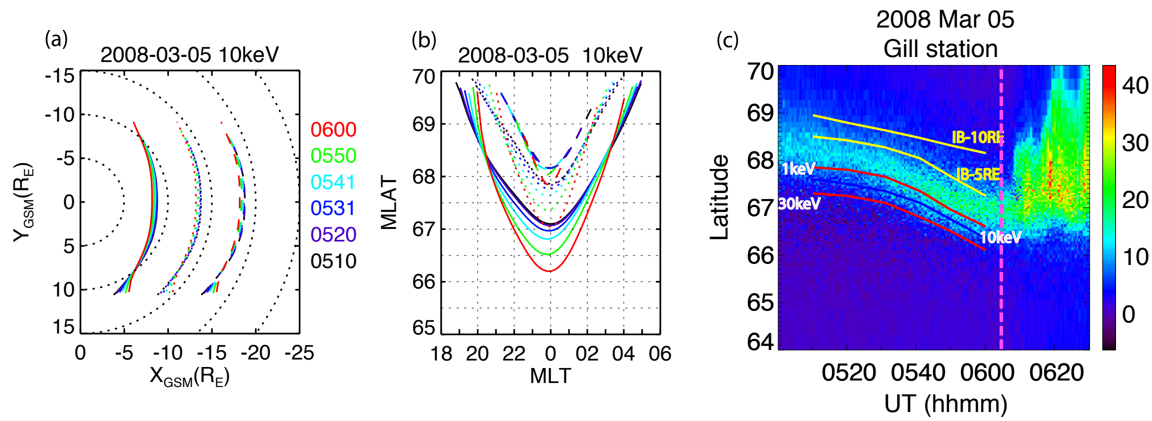

Figure 5.10. (a) The equatorial mapping of ion isotropic boundaries (solid lines), IBs-5R_E (dot lines) and IBs-10R_E (dashed lines) in X direction for different time snapshots (black: 05:10 UT; purple: 05:20 UT; blue: 05:31 UT; light blue: 05:41 UT; green: 05:50 UT; red: 06:00 UT) during March 5th, 2008 substorm event (onset is occurred at 06:04 UT according to auroral observations). (b) The corresponding mapping latitudes in ionosphere as a function of MLT. (c) The proton aurora observations at Gill station from 05:00-06:30 UT. The vertical dashed line marks the substorm onset time. The lower red line, blue line and the upper red line are the IB latitudes for 30, 10 and 1 keV proton, respectively. The lower and upper yellow lines are the corresponding mapping latitudes for IBs-5R_E and IBs-10R_E in X direction.

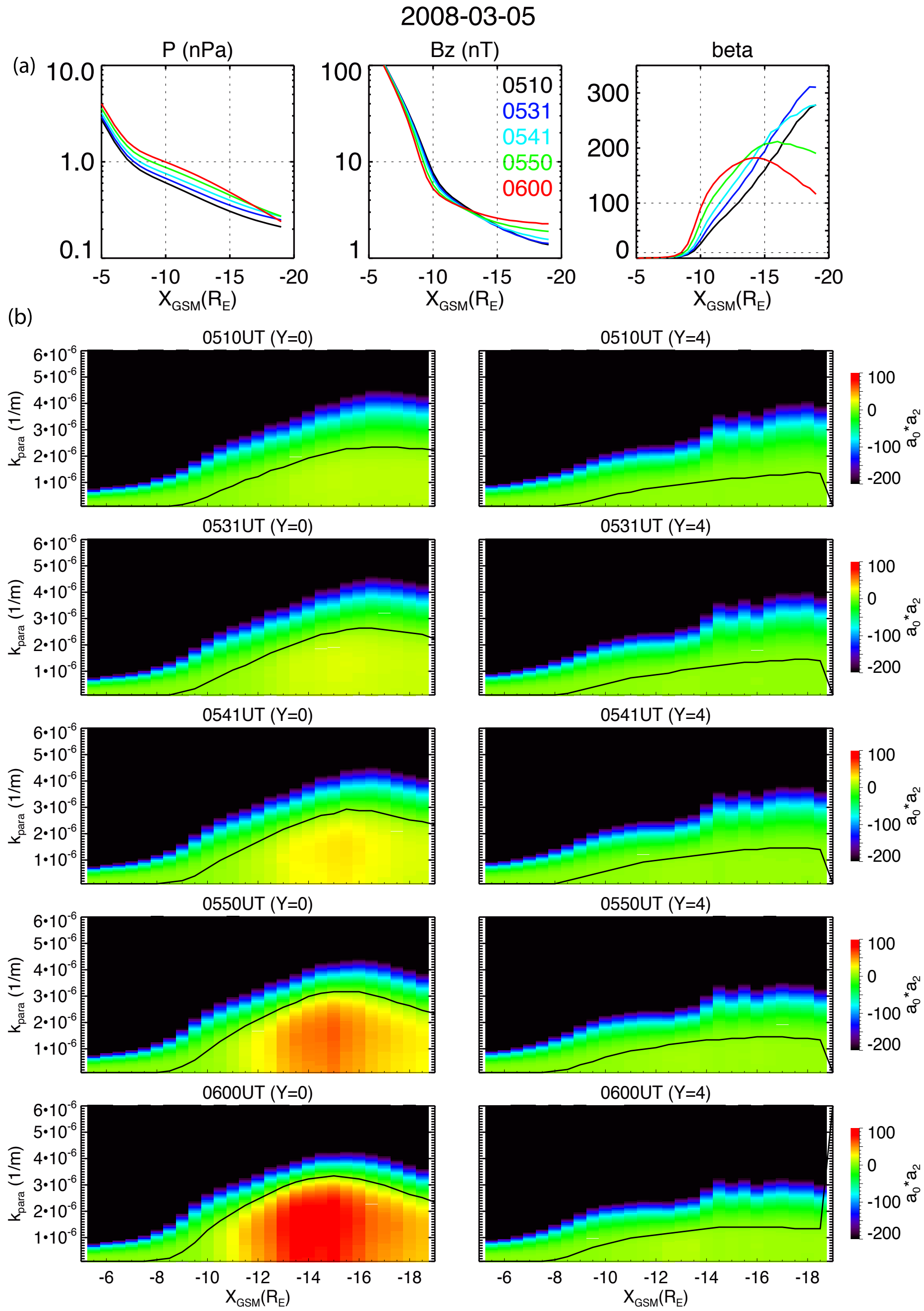

Figure 5.11. (a) The midnight radial profile of equatorial plasma pressure, Bz and plasma beta for 5 different time snapshots during March 5th, 2008 substorm event. The black, blue, light blue, green and red lines are for 05:10, 05:31,05:41, 05:50, 06:00 UT, respectively. (b) The equatorial radial profile of equivalent MHD ballooning instability growth rate for the same time snapshot as (a) at Midnight (Y = 0) and Y = $4R_E$. The black line marks $a_2 \cdot a_0 = 0$.

CHAPTER 6 | Summary and Concluding Remarks

The ultimate goal of my Ph.D. research has been to establish the very first substorm growth phase magnetic field model and to use it to investigate outstanding physical questions associated with substorms. In order to achieve this, the first part of my Ph.D. research involved: (1) processing and statistically analyzed the very large observational dataset from THEMIS (2007-2010) and GEOTAIL (1995-2005) satellites; (2) developing a 2D empirical plasma sheet pressure model under different Kp and P_{SW} and then used it as the input to the 3D force-balanced magnetic field solver to obtain the general behavior of magnetic field configurations in response to different Kp and P_{SW} levels; (3) analyzing the 3D pressure distributions and magnetic field configurations as well as current system as functions of Kp and P_{SW} and evaluated the interchange instability of plasma sheet and the differences with non-force balanced magnetic field model; (4) evaluating the ion isotropic boundaries due to current sheet scattering.

After the force-balanced pressure and magnetic field model in general had been successfully established, the second part of my research was using the force-balanced model to investigate substorm growth phase since the magnetospheric substorm is one of the two major space weather hazards threatening today's technological society and the physics responsible for substorms remain a major outstanding question in magnetospheric physics. A key to accurate evaluation of our understanding of these processes relies on knowing the realistic 3 dimensional (3D) Earth's magnetic field configurations, which cannot be provided by currently available empirical models with sufficient accuracy or as a function of growth phase development. So the 2^{nd} part of my Ph.D. research involved: (1) establishing an empirical substorm growth phase plasma sheet pressure model by using the SVRM technique and evaluated the model accuracy; (2) using the model pressures as input to establish the very first 3D substorm growth phase magnetic field model to describe the 3D plasma, magnetic field and current system; (3) applying the model to substorm event study to examine some underlying physical processes during the growth phase. The following are the main findings.

6.1 Plasma sheet pressure model for different Kp and P_{SW} levels

We have established an empirical model using Geotail and THEMIS data to best represent the spatial distribution of equatorial isotropic plasma pressure from r = 3 to 30 R_E on the nightside magnetosphere for Kp = 0 to 5 and for P_{SW} = 1.5 and 3 nPa. The empirical pressure provides the realistic pressure constraint for constructing 3D force-balanced magnetic field configurations. Unlike previous empirical models, we used plasma pressure plus radial magnetic pressure to represent equatorial plasma pressure. We also included pressure from high-energy ions as well as from electrons, which are important pressure contributors in the near-Earth region. This allows our pressure model to provide more accurate pressure gradients for our magnetic field modeling. From the pressure modeling, we have found that:

1. Our empirical pressure profiles well represent the statistical spatial distributions with very high correlation coefficients. Compared with pressure gradients computed using simultaneous measurements from two THEMIS spacecraft, our model also gives reasonable radial and azimuthal pressure gradients.
2. The pressure change with increasing Kp is characteristically different from the change with increasing P_{SW}. Larger convection electric field during higher Kp moves the plasma sheet further inward, resulting in larger increases in pressure and the radial pressure gradients in the near-Earth compared to the tail region. On the other hand, magnetosphere

compression by higher P_{SW} enhances pressure and radial pressure gradients more significantly in the tail region.

3. Both pressure and radial gradients are enhanced with increasing Kp or P_{SW}, no significant azimuthal pressure variations are found statistically for all Kp and P_{SW} conditions.

6.2 Empirical modeling of 3D force-balanced magnetospheric magnetic field structure

By using empirical pressure profiles established from THEMIS and GEOTAIL observations for different Kp and P_{SW} levels, we have computed 3D equilibrium magnetic field from the 3-D force balance magnetic field model. We have found:

1. In response to the increased plasma pressure during higher Kp and P_{SW}, enhanced J_φ decreases (increases) the Bz in the region earthward (tailward) of the J_φ peak. Relative to the changes from increasing P_{SW}, the Kp associated pressure enhancement causes the J_φ peak to move further earthward and the field lines to become more stretched.

2. The observed equatorial B_z for all Kp and P_{SW} conditions increases with decreasing r slightly in the tail plasma sheet but strongly in the near-Earth region. Across the tail, the equatorial Bz is relatively lower near midnight than near the flanks. The overall Bz increases in the tail but decreases in the near-Earth region with increasing Kp or P_{SW}, and the changes are more significant with the Kp change. The total B at a fixed r for all conditions increases with increasing Z as indicated by the decreasing plasma beta. The increase becomes sharper during higher Kp or P_{SW} and stronger increase is seen with increasing P_{SW}. Comparing these observed magnetic field profiles with the force-balanced magnetic field shows fairly good agreement, indicating our equilibrium model

can well present realistic 3D plasma and magnetic field configurations. The model accuracy in the inner magnetosphere can be further improved in the future when more reliable pressure measurements become available from the recently launched Van Allen probes and anisotropic pressure is taken into account in the force-balanced magnetic field.

3. In comparison with the non-force-balanced T89 magnetic field, there is no equatorial Bz minimum found for the considered pressure profiles. There is positive dBz/dz in the near-Earth region in most of the cases. A similar positive dBz/dz has been observed by THEMIS. Bifurcation of J_φ appears in the near Earth area as a result of our J_φ configuration being approximately aligned with field lines, while the T89 J_φ decreases monotonically with increasing Z everywhere.

4. Peaks of the R-2 FACs are near the inner edge of the plasma sheet, and the strength of FACs increase (decrease) as P_{SW} (Kp) increases. Field lines become more stretched and the mapping latitude of a fixed equatorial location is lower as Kp and P_{SW} increases, and more significant differences in the stretching and latitudes are associated with the Kp change. Mapping latitudes are slightly lower in the post-midnight than pre-midnight MLTs. In comparison, the T89 mapping latitudes are higher (lower) than our fields for Kp = 1 (Kp = 3).

5. The force-balanced pressure and magnetic field configurations for all Kp and P_{SW} are intrinsically stable to the interchange instability. However, the region near midnight may be unstable to the ballooning modes around X = –15 to –10 R_E due to very high beta and strong cross tail current.

6.3 Current sheet scattering and ion isotropic boundary under 3D empirical force-balanced magnetic field

We have investigated the role of tail current sheet scattering in the IB formation based on our 3D force-balanced magnetic field model. We first computed the ion TCS scattering parameter on the equatorial plane and the ion IB mapped to the ionosphere for protons from 1 to 30 keV. Then we compared our model results with high/low altitude satellites observations by THEMIS/FAST. We have found that:

1. The dependences of modeled IB latitudes on MLT, energy, Kp, and P_{SW} are consistent with those of FAST IBs: the IB moves to higher latitudes from midnight towards dawn/dusk and to lower latitudes as energy increases and as Kp or P_{SW} increases.
2. The modeled IB at the equator is located around the inner boundary of the highly isotropic ion distribution observed by THEMIS at midnight and post-midnight, while there is larger discrepancy at pre-midnight under higher Kp. The modeled IB matches fairly well with FAST IB for Kp = 0. As Kp becomes higher, the agreement at midnight remains generally good, but discrepancy becomes larger at dusk. Thus our results indicate that, while current sheet scattering is generally the dominant effect, other effects could be important on the duskside during active times. This duskside discrepancies can likely be accounted for by pitch-angle scattering by EMIC waves, which is expected to be more effective at dusk to noon MLTs and during higher geomagnetic activity.
3. For the FAST IB that has the energy dependence of lower latitude for higher energy, our model is capable of quantitatively producing the observed energy dependence. These model-observation comparisons strongly indicate that current sheet scattering plays a

major role in the IB formation for the 1-30 keV main plasma sheet ion population, similar to the conclusions from the previous studies on > 30 keV ions.

4. The overall better agreement in the model-comparison achieved by our force-balanced field than by the T89 indicates that taking into account the physical constraint of force-balance in a model can provide more accurate description of the magnetic configuration, and also reinforces our conclusions regarding the role of current sheet scattering for < 30 keV ions.

6.4 A 2D empirical plasma sheet pressure model for substorm growth phase using the support vector regression machine

We have identified the factors that are well correlated with plasma sheet pressure and its corresponding changes and built up a 2D equatorial empirical plasma sheet pressure model and an error model by using the Support Vector Regression Machine (SVRM) controlled by these factors. Major results from this study are:

1. Based on our large database of ~2,800,000 plasma pressure data points during substorm growth phase from THEMIS and Geotail observations from year 1995 to 2010, we identified P_{SW}, energy loading, and the sunspot number as the three primary contributors to pressure variations. The energy loading is a combination of time integral of CPCP and AE that we found is a better representative of energy loading.

2. By using these factors as inputs and using the SVRM technique, we have successfully constructed a 2D plasma sheet pressure model that has high accuracy with 5% median errors. Data and model comparison indicates that the new pressure model represents observations very well in general. The predicted pressure gradients also agree reasonably

well with the observed pressure gradients obtained from simultaneous THEMIS two-probe measurements.

3. We have found that the pressure increases linearly as P_{SW} increases. The pressure increase ratios are larger under lower energy loading but similar at different regions. On the other hand, the pressure responses to energy loading and sunspot number are nonlinear. The pressure increases first with increasing loading or sunspot number, it then remains relatively constant or decreases slightly after reaching a peak value at loading of ~8000 kV·min or at sunspot number of ~80. The loading effect is stronger when P_{SW} is lower. It is similar at different radial distance but stronger near midnight than away from midnight. The effect of sunspot number is more clearly seen at smaller r.

4. Our pressure model can be used to understand the pressure changes observed during a substorm event by providing evaluations of the individual and combined effects of energy loading and P_{SW}, as well as the combined temporal and spatial effect along the spacecraft trajectory.

6.5 Empirical modeling of 3D force-balanced plasma pressure and magnetic field structures during substorm growth phase

We have developed the very first empirical 3D force-balanced substorm growth phase magnetic field model. We have analyzed the growth phase evolution and evaluated the model predictions. Additionally, we have applied our models to one substorm event to analyze the underlying physical processes and onset location. Major results from this study are:

1. As the substorm growth phase develops (energy loading increases), plasma pressure, pressure gradient, and $J\varphi$ increase, while Bxy increases off the equator and the equatorial

magnetic field Bz decreases in the near earth region and increases in the tail due to increasing Jφ and the Jφ peak moving earthward. As a result, magnetic field lines become more stretched. Jφ at a given X-Y location peaks off the equator in the near Earth region and its peak moves towards equator due to the continuous stretching of magnetic field lines.

2. There are typical R1 FACs around 12 to 20 R_E at the beginning of the substorm growth phase, and they gradually evolve into R2 FACs in the late growth phase with their earthward boundary moving to smaller r.

3. The model Bz and total magnetic field strength, as well as FACs, are quite consistent with observations, indicating that our 3D substorm growth phase magnetic field model performs reasonably well.

4. The sunspot number effect is nonlinear and its effect maximizes at sunspot number ~60-80. Compared with the growth phase under a sunspot number of 20, the pressure under sunspot number of 50 is higher in the inner magnetosphere but lower in the tail, and the magnetic field configuration is slightly more stretched. On the other hand, the P_{SW} effect is linear and magnetic field lines are found to be significantly more stretched when P_{SW} increases from 2 to 4 nPa.

5. By applying our model to a substorm event, we found that the equatorward movement of proton aurora is mainly associated with the continuous stretching of magnetic field lines during the substorm growth phase, and the ballooning instability in plasma sheet is more favorable around midnight during the late growth phase at the location where there is a local peak in plasma beta. Also, the equatorial mapping of the electron breakup arc for

this event is at ~14 R_E before midnight, coinciding with the location of the maximum growth rate for ballooning instability.

References/Bibliography

Anderson, B. J., K. Takahashi, and B. A. Toth (2000), Sensing global Birkeland currents with Iridium® engineering magnetometer data, Geophys. Res. Lett., 27(24), 4045–4048, doi:10.1029/2000GL000094.

Angelopoulos, V., C. F. Kennel, F. V. Coroniti, R. Pellat, M. G. Kivelson, R. J. Walker, C. T. Russell, W. Baumjohann, W. C. Feldman, and J. T. Gosling (1994), Statistical Characteristics of Bursty Bulk Flow Events, J. Geophys. Res., 99(A11), 21,257–21,280.

Angelopoulos, V. (1996). The role of impulsive particle acceleration in magnetotail circulation, in Proceedings of the Third International Con- ference on Substorms (ICS-3), Spec. Publ. 389, pp. 17 – 22, Eur. Space Agency, Noordwijk, Netherlands.

Angelopoulos, V., et al. (1993), Characteristics of ion flow in the quiet state of the inner plasma sheet, Geophys. Res. Lett., 20, 1711–1714.

Auster, H. U., et al. (2008), The THEMIS fluxgate magnetometer, Space Sci. Rev., 141, 235–264, doi:10.1007/s11214-008-9365-9.

Baker, D. N., & McPherron, R. L. (1990). Extreme energetic particle decreases near geostationary orbit: A manifestation of current diversion within the inner plasma sheet. Journal of Geophysical Research: Space Physics (1978–2012), 95(A5), 6591-6599.

Baker, D. N., Pulkkinen, T. I., Angelopoulos, V., Baumjohann, W., & McPherron, R. L. (1996). Neutral line model of substorms: Past results and present view. Journal of Geophysical Research: Space Physics (1978–2012), 101(A6), 12975-13010.

Ban, P.-P., S.-J. Sun, C. Chen, and Z.-W. Zhao (2011), Forecasting of low-latitude storm-time ionospheric foF2 using support vector machine, Radio Sci., 46, RS6008, doi:10.1029/2010RS004633.

Baumjohann, W., G. Paschmann, and H. Lu¨hr (1990), Pressure balance between lobe and plasma sheet, Geophys. Res. Lett., 17, 45 – 48.

Baumjohann, W. J., G. Paschmann, T. Nagai, and H. Lu˙hr, Superposed epoch analysis of the substorm plasma sheet, J. Geophys. Res., 96, 11,605, 1991.

Baumjohann, W., and G. Paschmann, Determination of the polytropic index in the plasma sheet, Geophys. Res. Lett., 16, 295, 1989.

Becker, U., Neukirch, T., & Schindler, K. (2001). On the quasistatic development of thin current sheets in magnetotail‐like magnetic fields. Journal of Geophysical Research: Space Physics (1978‐2012), 106(A3), 3811-3825.

Birn, J., & Hesse, M. (1991). The substorm current wedge and field‐aligned currents in MHD simulations of magnetotail reconnection. Journal of Geophysical Research: Space Physics (1978‐2012), 96(A2), 1611-1618.

Borovsky, J. E., M. F. Thomsen, and R. C. Elphic (1998), The driving of the plasma sheet by the solar wind, J. Geophys. Res., 103(A8), 17,617– 17,640.

Borovsky, J. E., and M. H. Denton (2006), Differences between CME-driven storms and CIR-driven storms, J. Geophys. Res., 111, A07S08, doi:10.1029/2005JA011447.

Borovsky, J. E., Thomsen, M. F., & McComas, D. J. (1997). The superdense plasma sheet: Plasmaspheric origin, solar wind origin, or ionospheric origin?. Journal of Geophysical Research: Space Physics (1978–2012), 102(A10), 22089-22097.

Carlson, C. W., Pfaff, R. A., & Watzin, J. G. (1998). The fast auroral snapshot (FAST) mission. Geophysical research letters, 25(12), 2013-2016.

Chang, C. C., and C. J. Lin, (2001), LIBSVM: A library for support vector machines, Tech. rep., National Taiwan University, software available at http://www.csie.ntu.edu.tw/cjlin/libsvm.

Cheng, C. Z., Magnetospheric equilibrium with anisotropic pressure, J. Geophys. Res., 97, 1497, 1992.

Cheng, C.Z., 1995. Three-dimensional magnetospheric equilibrium with isotropic pressure. Geophysical Research Letters 22, 2401–2404.

Cheng, C. Z.; Qian, Q. (1994), Theory of ballooning-mirror instabilities for anisotropic pressure plasmas in the magnetosphere, Journal of Geophysical Research, 99, A6, 11193-11210, doi: 10.1029/94JA00657.

Cheng, C. Z., and A. T. Y. Lui (1998), Kinetic ballooning instability for substorm onset and current disruption observed by AMPTE/CCE, Geophys. Res. Lett., 25(21), 4091–4094.

Cheng, C. Z., and S. Zaharia (2004), MHD ballooning instability in the plasma sheet, Geophys. Res. Lett., 31, L06809, doi:10.1029/2003GL018823.

Cheng, A. F. (1985), Magnetospheric interchange instability, J. Geophys. Res., 90, 9900.

Chu, X., R. L. McPherron, T.-S. Hsu, V. Angelopoulos, Z. Pu, Z. Yao, H. Zhang and M. Connors (2015). "Magnetic mapping effects of substorm currents leading to auroral poleward expansion and equatorward retreat." Journal of Geophysical Research: Space Physics 120(1): 2014JA020596.

Chu, X. N., T. S. Hsu, R. L. McPherron, V. Angelopoulos, Z. Y. Pu, J. J. Weygand, K. Khurana, M. Connors, J. Kissinger, H. Zhang and O. Amm (2014). "Development and validation of inversion technique forsubstorm current wedge using ground magnetic field data." Journal ofGeophysical Research-Space Physics 119(3): 1909-1924.

Clauer, C., Gombosi, T. I., De Zeenw, D. L., Ridley, A. J., Powell, K. G., Van Leer, B., ... & Holzer, T. E. (2000). High performance computer methods applied to predictive space weather simulations. Plasma Science, IEEE Transactions on, 28(6), 1931-1937.

De Michelis, P.*,* I. A. Daglis*, and* G. Consolini *(*1999*),* An average image of proton plasma pressure and of current systems in the equatorial plane derived from AMPTE/CCE-CHEM measurements*,* J. Geophys. Res.*,* 104*(*A12*),* 28615–28624*, doi:*10.1029/1999JA900310.

Donovan, E., et al. (2006), The THEMIS all-sky imaging array-system design and initial results from the prototype imager, J. Atmos. Sol. Terr. Phys., 68, 1472–1487.

Donovan, E., Spanswick, E., Liang, J., Grant, J., Jackel, B., & Greffen, M. (2012). Magnetospheric dynamics and the proton aurora. Auroral Phenomenology and Magnetospheric Processes: Earth And Other Planets, 365-378.

Donovan, E. F., Jackel, B. J., Voronkov, I., Sotirelis, T., Creutzberg, F., & Nicholson, N. A. (2003a). Ground‐based optical determination of the b2i boundary: A basis for an optical MT‐index. Journal of Geophysical Research: Space Physics (1978–2012), 108(A3).

Donovan, E. F., Jackel, B., Strangeway, R., & Klumpar, D. (2003b). Energy dependence of the latitude of the 1–25 KeV ion isotropy boundary. Sodankylä Geophysical Observatory Publications, 92, 11-14.

Drucker, H., C. J. C. Burges, L. Kaufman, A. Smola, and V. Vapnik (1997), Support Vector Regression Machines, vol. 9, Advances in Neural Information Processing Systems, NIPS 1996, pp. 155–161, MIT Press, Denver, Colo.

Fairfield, D. H., R. P. Lepping, E. W. Hones Jr., S. J. Bame, and J. R. Asbridge (1981), Simultaneous measurements of magnetotail dynamics by IMP spacecraft, J. Geophys. Res., 86, 1396 – 1414.

Ganushkina, N. Y., Pulkkinen, T. I., Kubyshkina, M. V., Sergeev, V. A., Lvova, E. A., Yahnina, T. A., ... & Fritz, T. (2005). Proton isotropy boundaries as measured on mid- and low-altitude satellites. In Annales Geophysicae (Vol. 23, No. 5, pp. 1839-1847).

Gavrishchaka, V. V., and S. B. Ganguli (2001), Support vector machine as an efficient tool for high-dimensional data processing: Application to substorm forecasting, J. Geophys. Res., 106(A12), 29911–29914, doi:10.1029/2001JA900118.

Gkioulidou, M., C.-P. Wang, L. R. Lyons, and R. A. Wolf (2009), Formation of the Harang reversal and its dependence on plasma sheet conditions: Rice convection model simulations, J. Geophys. Res., 114, A07204, doi:10.1029/2008JA013955.

Gkioulidou, M., C.-P. Wang, and L. R. Lyons (2011), Effect of self-consistent magnetic field on plasma sheet penetration to the inner magnetosphere: Rice convection model simulations combined with modified Dungey force-balanced magnetic field solver, J. Geophys. Res., 116, A12213, doi:10.1029/2011JA016810.

Gonzalez, W. D., B. T. Tsurutani, and A. L. Clua de Gonzales (1999), Interplanetary origin of geomagnetic storms, Space Sci. Rev., 88, 529.

Guild, T., et al. (2004), Plasma sheet climatology: Geotail observations and LFM model comparisons, J. Atmos. Sol. Terr. Phys., 66(15 – 16), 1351 – 1360.

Harris, E. G., On a plasma sheath separating regions of oppositely directed magnetic field, Nuovo Cimento, XXIII, 115, 1962.

Hesse, M. and J. Birn, Three-dimensional magnetotail equilibria by numerical relaxation techniques, J. Geophys. Res., 98, 3973, 1993.

Hori, T., K. Maezawa, Y. Saito, and T. Mukai, Average profile of ion flow and convection electric field in the near-Earth plasma sheet, Geophys. Res. Lett., 27, 1623, 2000.

Hsu, T.-S., and R. L. McPherron (2012), A Statistical Analysis of Substorm Associated Tail Activity, Advance in Space Research, 50 (10), 1317-1343, doi:1310.1016/j.asr.2012.1306.1034, doi: 10.1016/j.asr.2012.06.034.

Huang, C. Y., and L. A. Frank (1986), A statistical survey of the central plasma sheet: implications for substorm models, *Geophys. Res. Lett.*, *13*, 652-655.

Huang Cong, Dan-Dan Liu, Jing-Song Wang, Forecast daily indices of solar activity, F10.7, using support vector regression method, Research in Astronomy and Astrophysics, 2009, 9, 6, 694

Hurricane, O. A. (1997), MHD ballooning stability of a sheared plasma sheet, J. Geophys. Res., 102(A9), 19,903–19,911, doi:10.1029/97JA01595.

Iijima, T., and T. A. Potemra (1976a), Field-Aligned Currents in the Dayside Cusp Observed by Triad, J. Geophys. Res., 81(34), 5971–5979, doi:10.1029/JA081i034p05971.

Iijima, T., and Potemra, T. A. (1976b). The amplitude distribution of field‐aligned currents at northern high latitudes observed by Triad. Journal of Geophysical Research, 81(13), 2165-

2174.

Jordanova, V. K., Farrugia, C. J., Thorne, R. M., Khazanov, G. V., Reeves, G. D., & Thomsen, M. F. (2001). Modeling ring current proton precipitation by electromagnetic ion cyclotron waves during the May 14–16, 1997, storm. Journal of Geophysical Research: Space Physics (1978–2012), 106(A1), 7-22.

Kaufmann, R. L., B. M. Ball, W. R. Paterson, and L. A. Frank, Plasma sheet thickness and electric currents, J. Geophys. Res., 106, 6179, 2001.

Kaufmann, R. L., C. Lu, W. R. Paterson, and L. A. Frank (2002), Three- dimensional analyses of electric currents and pressure anisotropies in the plasma sheet, J. Geophys. Res., 107(A7), 1103, doi:10.1029/ 2001JA000288.

Kaufmann, R. L., W. R. Paterson, and L. A. Frank (2004), Pressure, volume, density relationships in the plasma sheet, J. Geophys. Res., 109, A08204, doi:10.1029/2003JA010317.

Kirpichev, I. P., E. E. Antonova (2011), Plasma pressure distribution in the equatorial plane of the Earth's magnetosphere at geocentric distances of 6–10 R E according to the international THEMIS mission data, Geomagnetizm I Aeronomiya - GEOMAGN AERON, 51, no. 4, doi: 10.1134/S0016793211040049

Kistler, L. M., E. Möbius, W. Baumjohann, G. Paschmann, and D. C. Hamilton (1992), Pressure changes in the plasma sheet during substorm injections, *J. Geophys. Res., 97,* 2973-2983.

Kistler, L. M., W. Baumjohann, T. Nagai, and E. Mo˙bius, Superposed epoch analysis of pressure and magnetic field configuration changes in the plasma sheet, J. Geophys. Res., 98, 9249, 1993.

Kokubun, S., T. Yamamoto, M. H. Acuna, K. Hayashi, K. Shiokawa, and H. Kawano (1994), The Geotail magnetic field experiment, J. Geomagn. Geoelectr., 46, 7–21, doi:10.5636/jgg.46.7.

Kropotkin, A. P., & Lui, A. T. Y. (1995). Quasi‐static evolution of the magnetosphere: The substorm growth phase. Journal of Geophysical Research: Space Physics (1978‐2012), 100(A9), 17231-17239.

Kubyshkina, M., V. Sergeev, N. Tsyganenko, V. Angelopoulos, A. Runov, E. Donovan, H. Singer, U. Auster, and W. Baumjohann (2011), Time‐dependent magnetospheric configuration and breakup mapping during a substorm, J. Geophys. Res., 116, A00I27, doi:10.1029/2010JA015882.

Lagarias, J. C., J. A. Reeds, M. H. Wright, and P. E. Wright (1998), Convergence Properties of the Nelder-Mead Simplex Method in Low Dimensions, *SIAM Journal of Optimization*, Vol. 9, Number 1, pp. 112–147.

Lee, D. Y., and R. A. Wolf (1992), Is the Earth's magnetotail balloon unstable?, J. Geophys. Res., 97(A12), 19,251–19,257.

Liang, J., Donovan, E., Ni, B., C. Yue, Jiang, F., & Angelopoulos, V. (2014). On an energy-latitude dispersion pattern of ion precipitation potentially associated with magnetospheric

EMIC waves. Journal of Geophysical Research: Space Physics, 119, doi: 10.1002/2014JA020226.

Liu, S., M. W. Chen, M. Schulz, and L. R. Lyons (2006), Initial simulation results of storm-time ring current in a self- consistent magnetic field model, J. Geophys. Res., 111, A04225, doi:10.1029/2005JA011194.

Liu, D. D., Huang, C., Lu, J. Y. and Wang, J. S. (2011), The hourly average solar wind velocity prediction based on support vector regression method. Monthly Notices of the Royal Astronomical Society, 413: 2877–2882. doi: 10.1111/j.1365-2966.2011.18359.x

Liu, W. W. (1997). Physics of the explosive growth phase: Ballooning instability revisited. Journal of Geophysical Research: Space Physics (1978–2012), 102(A3), 4927-4931.

Lui, A. T. Y. (1996). Current disruption in the Earth's magnetosphere: Observations and models. Journal of Geophysical Research: Space Physics (1978–2012), 101(A6), 13067-13088.

Lui, A. T. Y., and D. C. Hamilton (1992), Radial profiles of quiet time magnetospheric parameters, *J. Geophys. Res*., *97*, 19,325–19,332.

Lui, A. T. Y., Inner magnetospheric plasma pressure distribution and its local time asymmetry, Geophys. Res. Lett., 30(16), 1846, doi:10.1029/ 2003GL017596, 2003.

Lvova, E. A., Sergeev, V. A., & Bagautdinova, G. R. (2005). Statistical study of the proton isotropy boundary. In Annales Geophysicae, Vol. 23, No. 4, pp. 1311-1316. Copernicus GmbH.

Lyons, L. R., Y. Nishimura, E. Donovan, and V. Angelopoulos (2013), Distinction between auroral substorm onset and traditional ground magnetic onset signatures, J. Geophys. Res. Space Physics, 118, 4080–4092, doi:10.1002/jgra.50384.

Machida et al., statistical visualization of the Earth's magnetotail based on Geotail data and the implied substorm model, Ann. Geophys., 2009.

McCollough, J. P., J. L. Gannon, D. N. Baker, and M. Gehmeyr (2008), A statistical comparison of commonly used external magnetic field models, Space Weather, 6, S10001, doi:10.1029/2008SW000391.

McFadden, J. P., C. W. Carlson, D. Larson, V. Angelopoulos, M. Ludlam, R. Abiad, B. Elliott, P. Turin, and M. Marckwordt (2008a), The THEMIS ESA plasma instrument and in-flight calibration, Space Sci. Rev., 141, 277–302, doi:10.1007/s11214-008-9440-2.

McPherron, R. L. (1970). Growth phase of magnetospheric substorms. Journal of Geophysical Research, 75(28), 5592-5599.

Miura, A., Ohtani, S., & Tamao, T. (1989). Ballooning instability and structure of diamagnetic hydromagnetic waves in a model magnetosphere. Journal of Geophysical Research: Space Physics (1978–2012), 94(A11), 15231-15242.

Miyashita, Y., S. Machida, T. Mukai, Y. Saito, K. Tsuruda, H. Hayakawa, and P. R. Sutcliffe (2000), A statistical study of variations in the near and middistant magnetotail associated with substorm onsets: GEOTAIL observations, J. Geophys. Res., 105(A7), 15913–15930.

Miyashita, Y., S. Machida, T. Mukai, Y. Saito, and P. R. Sutcliffe (2001), Mass and energy transport in the near and middistant magnetotail around substorm onsets: Geotail observations, J. Geophys. Res., 106(A4), 6259–6274, doi:10.1029/2000JA000233.

Miyashita, Y., S. Machida, K. Liou, T. Mukai, Y. Saito, H. Hayakawa, C.-I. Meng, and G. K.

Parks (2003), Evolution of the magnetotail associated with substorm auroral breakups, J. Geophys. Res., 108, 1353, doi:10.1029/2003JA009939, A9.

Miyashita, Y., et al. (2009), A state-of-the-art picture of substorm-associated evolution of the near-Earth magnetotail obtained from superposed epoch analysis, J. Geophys. Res., 114, A01211, doi:10.1029/2008JA013225.

Miyashita, Y., et al. (2010), Pressure changes associated with substorm depolarization in the near-Earth plasma sheet, J. Geophys. Res., 115, A12239, doi:10.1029/2010JA015608.

Mukai, T., S. Machida, Y. Saito, M. Hirahara, T. Terasawa, N. Kaya, T. Obara, M. Ejiri, and A. Nishida (1994), The low-energy particle (LEP) experiment onboard the Geotail satellite, J. Geomagn. Geoelectr., 46, 669–692, doi:10.5636/jgg.46.669.

Murphy, K. R., I. R. Mann, I. J. Rae, C. L. Waters, B. J. Anderson, D. K. Milling, H. J. Singer, and H. Korth (2012), Reduction in field-aligned currents preceding and local to auroral substorm onset, Geophys. Res. Lett., 39, L15106, doi:10.1029/2012GL052798.

Nakamura, M., G. Paschmann, W. Baumjohann, and N. Sckopke, Ion distributions and flows near the neutral sheet, J. Geophys. Res., 96, 5631,1991.

Newell, P. T., V. A. Sergeev, G. R. Bikkuzina, *and* S. Wing (1998), Characterizing the state of the magnetosphere: Testing the ion precipitation maxima latitude (b2i) and the ion isotropy boundary, J. Geophys. Res., 103(A3), 4739–4745, *doi:*10.1029/97JA03622.

Nishimura, Y., L. Lyons, S. Zou, X. Xing, V. Angelopoulos, S. Mende, J. Bonnell, D. Larson, U. Auster, T. Hori, N. Nishitani, K. Hosokawa, G. Sofko, M. Nicolls, and C. Heinselman, Pre-onset time sequence of auroral substorms: Coordinated observations by ASIs, satellites and radars, J. Geophys. Res., 115, A00I08, doi:10.1029/2010JA015832.

Nishimura, Y., L. R. Lyons, V. Angelopoulos, T. Kikuchi, S. Zou, and S. B. Mende (2011), Relations between multiple auroral streamers, pre-onset thin arc formation, and substorm auroral onset, J. Geophys. Res., 116, A09214, doi:10.1029/2011JA016768.

Noble, W. S. (2006), What is a support vector machine? Nat. Biotechnol., 24, 1565–1567.

Ohtani, S., S. Wing, V. G. Merkin, and T. Higuchi (2014), Solar cycle dependence of nightside field-aligned currents: Effects of dayside ionospheric conductivity on the solar wind-magnetosphere-ionosphere coupling, J. Geophys. Res. Space Physics, 119, 322–334, doi:10.1002/2013JA019410.

Olson, W. P., and K. A. Pfitzer (1974), Quantitative model of magnetospheric magnetic field, J. Geophys. Res., 79, 3739.

Petrinec, S. M., & Russell, C. T. (1993). An empirical model of the size and shape of the near‐Earth magnetotail. Geophysical research letters, 20(23), 2695-2698.

Powell, K.G., Roe, P.L., Linde, T.J., Gombosi, T.I., Zeeuw, D.L.D., 1999. A solution-adaptive upwind scheme for ideal magnetohydrodynamics. Journal of Computational Physics 154, 284–309.

Pritchett, P. L., & Coroniti, F. V. (2010). A kinetic ballooning/interchange instability in the magnetotail. Journal of Geophysical Research: Space Physics (1978–2012), 115(A6).

Pu, Z. Y., A. Korth, Z. X. Chen, R. H. W. Friedel, Q. G. Zong, X. M. Wang, M. H. Wong, S. Y. Fu, and T. I. Pulkkinen (1997), MHD drift ballooning instability near the inner edge of the near-Earth plasma sheet, J. Geophys. Res., 102(A7), 14,397–14,406.

Raeder, J., Walker, R. J., & Ashour‐Abdalla, M. (1995). The structure of the distant geomagnetic tail during long periods of northward IMF. Geophysical research letters, 22(4), 349-352.

Saito, M. H., L.-N. Hau, C.-C. Hung, Y.-T. Lai, and Y.-C. Chou (2010), Spatial profile of magnetic field in the near-Earth plasma sheet prior to dipolarization by THEMIS: Feature of minimum B, Geophys. Res. Lett., 37, L08106, doi:10.1029/2010GL042813.

Saito, M. H., D. Fairfield, G. Le, L.-N. Hau, V. Angelopoulos, J. P. McFadden, U. Auster, J. W. Bonnell, and D. Larson (2011), Structure, force balance, and evolution of incompressible cross-tail current sheet thinning, J. Geophys. Res., 116, A10217, doi:10.1029/2011JA016654.

Sanny, J., McPherron, R.L., Russell, C.T., Baker, D.N., Pulkkinen, T.I., Nishida, A., (1994). Growth-phase thinning of the near-Earth current sheet during the CDAW 6 substorm. Journal of Geophysical Research 99, 5805–5816.

Sergeev, V., Y. Nishimura, M. Kubyshkina, V. Angelopoulos, R. Nakamura, and H. Singer (2012), Magnetospheric location of the equatorward prebreakup arc, J. Geophys. Res., 117, A01212, doi:10.1029/2011JA017154.

Sergeev, V. A., and N. A. Tsyganenko (1982), Energetic particle losses and trap- ping boundaries as deduced from calculations with a realistic magnetic field model, Planet. Space Sci., 10, 999.

Sergeev, V. A., E. M. Sazhina, N. A. Tsyganenko, J. A. Lunbland, and F. Soraas (1983), Pitch angle scattering of energetic protons in the magnetotail current sheet as the dominant source of their isotropic precipitation into the nightside ionosphere, Planet. Space Sci., 31, 1147–1158.

Sergeev V. A. and Malkov M. V (1988). Diagnostic of the magnetic con- figuration of the plasma sheet from measurements of energetic electrons above the ionosphere, Geomagn. Aeron., 28, 649–653.

Sergeev, V. A. and Gvozdevsky, B. B. (1995), MT-index − a possible new index to characterize the magnetic configuration of magnetotail, Ann. Geophys., 13, 1093-1103, doi:10.1007/s00585-995-1093-9.

Sergeev, V. A., M. Malkov, and K. Mursula (1993), Testing the Isotropic Boundary Algorithm Method to Evaluate the Magnetic Field Configuration in the Tail, J. Geophys. Res., 98(A5), 7609–7620, doi:10.1029/92JA02587.

Sergeev, V.A., Tanskanen, P., Mursula, K., Korth, A., Elphic, R.C., (1990). Current sheet thickness in the near-Earth plasma sheet during substorm growth phase. Journal of Geophysical Research 95, 3819–3828.

Sergeev, V., Angelopoulos, V., Kubyshkina, M., Donovan, E., Zhou, X.Z., Runov, A., Singer, H., McFadden, J., Nakamura, R., (2011). Substorm growth and expansion onset as observed with ideal ground-spacecraft THEMIS coverage. Journal of Geophysical Research 116.

Shevchenko, I. G., V. Sergeev, M. Kubyshkina, V. Angelopoulos, K. H. Glassmeier, and H. J. Singer (2010), Estimation of magnetosphere‐ionosphere mapping accuracy using isotropy boundary and THEMIS observations, J. Geophys. Res., 115, A11206, doi:10.1029/2010JA015354.

Shiokawa, K., Baumjohann, W., & Haerendel, G. (1997). Braking of high speed flows in the near‐Earth tail. Geophysical research letters, 24(10), 1179-1182.

Shue, J.-H., J. K. Chao, H. C. Fu, C. T. Russell, P. Song, K. K. Khurana, and H. J. Singer (1997), A new functional form to study the solar wind control of the magnetopause size and shape, J. Geophys. Res., 102(A5), 9497–9511, doi:10.1029/97JA00196.

Singer, H., L. Matheson, R. Grubb, A. Newman, and D. Bouwer (1996), Monitoring space weather with the GOES magnetometers, in GOES-8 and Beyond, vol. 2812, edited by E. R. Washwell, pp. 299– 308, Soc. of Photo-Optical Instrum. Eng., Bellingham, Wash.

Southwood, D. J., and M. G. Kivelson (1987), Magnetospheric interchange instability, J. Geophys. Res., 92, 109.

Speiser, T. W. (1965), Particle trajectories in a model current sheet, based on the open model of the magnetosphere, with applications to auroral particles, J. Geophys. Res., 70(7), 1717–1728, doi:10.1029/JZ070i007p01717.

Spence, H. E., M. G. Kivelson, R. J. Walker, and D. J. McComas (1989), Magnetospheric plasma pressures in the midnight meridian: observations from 2.5 to 35 R_E, *J. Geophys. Res.*, *94*, 5264–5272.

Spence, H. E., and M. G. Kivelson (1993), Contributions of the low–latitude boundary layer to the finite width magnetotail convection model, *J. Geophys. Res.*, *98*, 15,487–15,496.

Stiles, G. S., J. E. W. Hones Jr., S. J. Bame, and J. R. Asbridge, Plasmasheet pressure anisotropies, J. Geophys. Res., 83, 3166, 1978.

Toffoletto, F. R., R. W. Spiro, R. A. Wolf, M. Hesse, and J. Birn (2001), Modeling inner magnetospheric electrodynamics, in Space Weather, Geophys. Monogr. Ser., vol. 125, edited by P. Song, H. J. Singer, and G. L. Siscoe, pp. 265–272, AGU, Washington, D. C.

Tsyganenko, N. A., and T. Mukai (2003), Tail plasma sheet models derived from Geotail particle data, J. Geophys. Res., 108(A3), 1136, doi:10.1029/2002JA009707.

Tsyganenko, N. A., (1995) Modeling the Earth's magnetospheric magnetic field confined within a realistic magnetopause, J. Geophys. Res., 100, 5599–5612.

Tsyganenko, N. A. (1996), Effects of the solar wind conditions on the global magnetospheric configuration as deduced from data-based field models, in Proceedings of the ICS-3 Conference on Substorms, Eur. Space Agency Spec. Publ. 389, pp. 181–185, Eur. Space Agency, Noordwijk, Netherlands.

Tsyganenko, N.A., (1989). A magnetospheric magnetic field model with a warped tail current sheet. Planet. Space Sci. 37, 5–20.

Tsyganenko, N. A. (1990), Quantitative models of magnetospheric magnetic field: Methods and results, Space. Sci. Rev., 54, 75.

Tsyganenko, N. A., (2010) On the reconstruction of magnetospheric plasma pressure distributions from empirical geomagnetic field models, J. Geophys. Res., v.115, A07211, doi:10.1029/2009JA015012.

Usanova, M. E., I. R. Mann, J. Bortnik, L. Shao, and V. Angelopoulos (2012), THEMIS observations of electromagnetic ion cyclotron wave occurrence: Dependence on AE, SYMH, and solar wind dynamic pressure, J. Geophys. Res., 117, A10218, doi:10.1029/2012JA018049.

Vapnik, V., and A. Lerner (1963), Pattern recognition using generalized portrait method, Autom. Remote Control, 24, 774–780.

Vasyliunas, V. M. (1970), Mathematical models of magnetospheric convection and its coupling to the ionosphere, in Particles and Fields in the Magnetosphere, edited by B. M. McCormac, pp. 60–71, D. Reidel, Hingham, Mass.

Vasyliunas, V. M. (1984), Fundamentals of current description, Magnetospheric Currents, Geophys. Monogr. Ser., 28, edited by T. A. Potemra, pp. 63–66, AGU, Washington, D. C.

Voigt, G.-H., and R. A. Wolf (1988), Quasi-static magnetospheric MHD processes and the "ground state" of the magnetosphere, Rev. Geophys., 26(4), 823–843, doi:10.1029/RG026i004p00823.

Wang, C.-P., S. G. Zaharia, L. R. Lyons, and V. Angelopoulos (2012), Spatial distributions of ion pitch angle anisotropy in the near-Earth magnetosphere and tail plasma sheet, J. Geophys. Res., 118, 1-12, doi:10.1029/2012JA018275.

Wang, C.-P., Chao Yue, S. Zaharia, X. Xing, L. Lyons, V. Angelopoulos, T. Nagai, and T. Lui (2013), Empirical modeling of plasma sheet pressure and three-dimensional force-balanced magnetospheric magnetic field structure: 1. Observation, J. Geophys. Res. Space Physics, 118, doi:10.1002/jgra.50585.

Wang, C. P., Lyons, L. R., Weygand, J. M., Nagai, T., & McEntire, R. W. (2006). Equatorial distributions of the plasma sheet ions, their electric and magnetic drifts, and magnetic fields under different interplanetary magnetic field Bz conditions. Journal of Geophysical Research: Space Physics (1978–2012), 111(A4).

Wang, C.-P., L. R. Lyons, T. Nagai, J. M. Weygand, and R. W. McEntire (2007), Sources, transport, and distributions of plasma sheet ions and electrons and dependences on interplanetary parameters under northward interplanetary magnetic field, J. Geophys. Res., 112, A10224, doi:10.1029/2007JA012522.

Wang, C.-P., L. R. Lyons, R. A. Wolf, T. Nagai, J. M. Weygand, and A. T. Y. Lui (2009), The plasma sheet PV5/3 and nV and associated plasma and energy transport for different convection strengths and AE levels, J. Geophys. Res., 114, A00D02, doi:10.1029/2008JA013849.

Wang, C.-P., L. R. Lyons, T. Nagai, J. M. Weygand, and A. T. Y. Lui (2010), Evolution of plasma sheet particle content under different interplanetary magnetic field conditions, J. Geophys. Res., 115, A06210, doi:10.1029/2009JA015028.

Wang, C.-P., M. Gkioulidou, L. R. Lyons, R. A. Wolf, V. Angelopoulos, T. Nagai, J. M. Weygand, and A. T. Y. Lui (2011), Spatial distributions of ions and electrons from the plasma sheet to the inner magnetosphere: Comparisons between THEMIS-Geotail statistical results and the Rice convection model, J. Geophys. Res., 116, A11216, doi:10.1029/2011JA016809.

Wang, C.-P., L. R. Lyons, M. W. Chen, and F. R. Toffoletto, Modeling the transition of the inner plasma sheet from weak to enhanced convection, J. Geophys. Res., 109, A12202, doi:10.1029/2004JA010591, 2004.

Wang, C.-P., L. R. Lyons, M. W. Chen, and R. A. Wolf, Two-dimensional quiet time equilibrium for the inner plasma sheet protons and magnetic field, Geophys. Res. Lett., 29(24), 2186, doi:10.1029/ 2001GL013984, 2002.

Wang, C.-P., L. R. Lyons, M. W. Chen, and R. A. Wolf, Modeling the quiet time inner plasma sheet protons, J. Geophys. Res., 106, 6161, 2001.

Wang, Y., D. G. Sibeck, J. Merka, S. A. Boardsen, H. Karimabadi, T. B. Sipes, J. Šafránková, K. Jelínek, and R. Lin (2013), A new three-dimensional magnetopause model with a support vector regression machine and a large database of multiple spacecraft observations, J. Geophys. Res. Space Physics, 118, 2173–2184, doi:10.1002/jgra.50226.

Waters, C. L., B. J. Anderson, and K. Liou (2001), Estimation of global field aligned currents using the Iridium® system magnetometer data, Geophys. Res. Lett., 28(11), 2165–2168, doi:10.1029/2000GL012725.

Weimer, D. R. (1995), Models of high-latitude electric potentials derived with a least error fit of spherical harmonic coefficients, J. Geophys. Res., 100(A10), 19,595–19,608, doi:10.1029/95JA01755.

Weiss, L. A., M. F. Thomsen, G. D. Reeves, and D. J. McComas (1997), An examination of the Tsyganenko (T89a) field model using a database of two-satellite magnetic conjunctions, J. Geophys. Res., 102(A3), 4911–4918.

Wiegelmann, T., & Schindler, K. (1995). Formation of thin current sheets in a quasistatic magnetotail model. Geophysical research letters, 22(15), 2057-2060.

Williams, D. J., R. W. McEntire, C. Schlemm II, A. T. Y. Lui, G. Gloeckler, S. P. Christon, and F. Gliem (1994), Geotail energetic particles and ion composition instrument, J. Geomagn. Geoelectr., 46, 39–57, doi:10.5636/jgg.46.39.

Wing, S., and P. T. Newell (1998), Central plasma sheet ion properties as inferred from ionospheric observations, *J. Geophys. Res.*, *103*, 6785–6800.

Wing, S., and P. T. Newell (2000), Quiet time plasma sheet ion pressure contribution to Birkeland currents, J. Geophys. Res., 105(A4), 7793–7802, doi:10.1029/1999JA900464.

Wing, S., J. W. Gjerloev, J. R. Johnson, and R. A. Hoffman (2007), Substorm plasma sheet ion pressure profiles, Geophys. Res. Lett., 34, L16110, doi:10.1029/2007GL030453.

Wolf, R. A. (1983), The quasi-static (slow-flow) region of the magnetosphere, in Solar-Terrestrial Physics, 303–368, D. Reidel, Hingham, MA.

Xing, X., and R. A. Wolf (2007). Criterion for interchange instability in a plasma connected to a conducting ionosphere, J. Geophys. Res., 112, A12209, doi:10.1029/2007JA012535.

Xing, X. (2008), Criterion for interchange instability in the plasma sheet, Houston, Texas : Rice University.

Xing, X., L. R. Lyons, V. Angelopoulos, D. Larson, J. McFadden, C. Carlson, A. Runov, and U. Auster (2009), Azimuthal plasma pressure gradient in quiet time plasma sheet, Geophys. Res. Lett., 36, L14105, doi:10.1029/ 2009GL038881.

Xing, X., L. R. Lyons, V. Angelopoulos, D. Larson, C. Carlson, A. Runov, and U. Auster (2010), Plasma sheet pressure evolution related to substorms, J. Geophys. Res., 115, A01212, doi:10.1029/2009JA014315.

Xing, X., L. R. Lyons, Y. Nishimura, V. Angelopoulos, E. Donovan, E. Spanswick, J. Liang, D. Larson, C. Carlson, and U. Auster (2011), Near-Earth plasma sheet azimuthal pressure gradient and associated auroral development soon before substorm onset, J. Geophys. Res., 116, A07204, doi:10.1029/2011JA016539.

Xing, X., J. Liang, E. Spanswick, L. Lyons, and V. Angelopoulos (2013), Auroral wave structures and ballooning instabilities in the plasma sheet, J. Geophys. Res. Space Physics, 118, 6319–6326, doi:10.1002/2013JA019068.

Yang, J., F. R. Toffoletto, R. A. Wolf, and S. Sazykin (2011), RCM-E simulation of ion acceleration during an idealized plasma sheet bubble injection, J. Geophys. Res., 116, A05207.

Yue, C., C.-P. Wang, S. G. Zaharia, X. Xing, and L. Lyons (2013), Empirical modeling of plasma sheet pressure and three-dimensional force-balanced magnetospheric magnetic field structure: 2. Modeling, J. Geophys. Res. Space Physics, 118, 6166–6175, doi:10.1002/2013JA018943.

Yue, C., C.-P. Wang, L. Lyons, J. Liang, E. F. Donovan, S. G. Zaharia, and M. Henderson (2014), Current sheet scattering and ion isotropic boundary under 3-D empirical force-balanced magnetic field, J. Geophys. Res. Space Physics, 119, doi:10.1002/2014JA020172.

Yue, C., C.-P. Wang, L. Lyons, Y. Wang, T. Hsu, M. Henderson, A.T.Y. Lui, V. Angelopoulos, Tsugunobu Nagai (2015), A 2D empirical plasma sheet pressure model for substorm growth phase using the Support Vector Regression Machine, J. Geophys. Res. Space Physics, 120, doi:10.1002/2014JA020787.

Zaharia, S., and C. Z. Cheng (2003), Can an isotropic plasma pressure distribution be in force balance with the T96 model field?, J. Geophys. Res., 108(A11), 1412, doi:10.1029/2002JA009501.

Zaharia, S., Cheng, C.Z., Maezawa, K., 2004. 3-D force-balanced magnetospheric configurations. Annales Geophysicae 22, 251–265.

Zaharia, S., Jordanova, V.K., Thomsen, M.F., Reeves, G.D., 2006. Self-consistent modeling of magnetic fields and plasmas in the inner magnetosphere: Application to a geomagnetic storm. Journal of Geophysical Research (Space Physics) 111, A11S14.

Zaharia, S. (2008), Improved Euler potential method for three-dimensional magnetospheric equilibrium, J. Geophys. Res., 113, A08221, doi:10.1029/ 2008JA013325.

Zavriyev, A., & Hasegawa, A. (1989). The equilibrium dayside magnetosphere. Journal of Geophysical Research: Space Physics (1978–2012), 94(A8), 10039-10045.

Zhu, P., Raeder, J., Germaschewski, K., & Hegna, C. C. (2009). Initiation of ballooning instability in the near-Earth plasma sheet prior to the 23 March 2007 THEMIS substorm expansion onset. In Annales Geophysicae (Vol. 27, No. 3, pp. 1129-1138). Copernicus GmbH.